4. Set the flow rate of the air and tested gas using the needle valves, and install the volumetric concentration of (3)% test gas to air.
5. Measurement of current variation is observed using the PC- interfaced digital multimeter of type (UNI-UT81B).
6. At the first time the digital multimeter record the biasing current of air flow, after that switch-on the testing gas ($NO_2$), and after several second the current has low variation, then switch-off the test gas to record the recovery time.

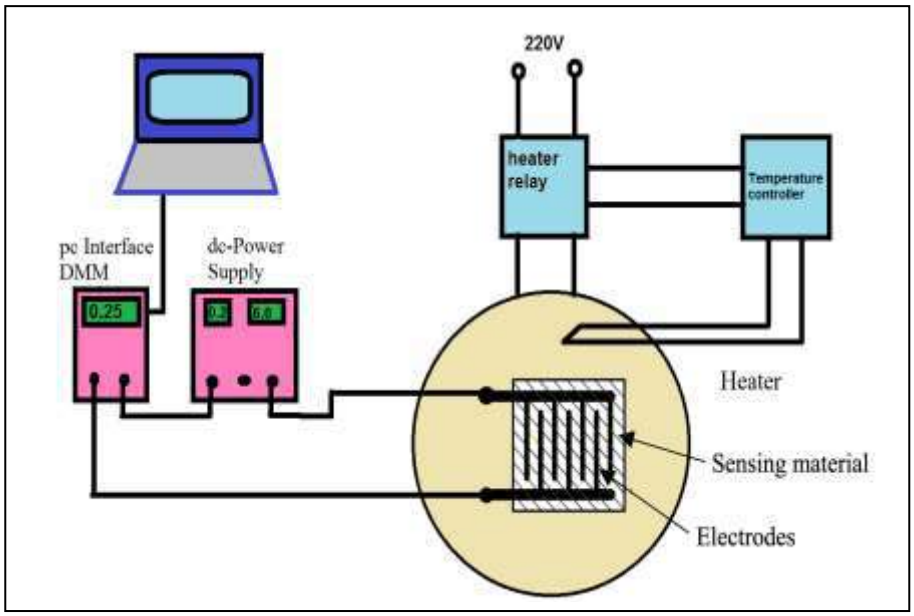


Fig. 3.8: Schematic Diagram and the Electrical Circuit Setup for Gas Sensing Measurements.

## 4.1 Introduction

In this chapter, the results and the analysis of the experimental measurements of the $Mg_xZnO_{1-x}$ thin films which were prepared by (CSP) on glass and silicon substrates, when at the different Mg-contents(0,30,50,70,and 90)% , and substrate temperatures (400,450, and 500)$^oC$. The structural, Raman shift, optical, and electrical properties of $Mg_xZnO_{1-x}$/n-Si photodetector have been studied. The structural and electrical properties of $Mg_xZnO_{1-x}$/n-Si photodetector were studied at constant thickness. Finally the sensing properties for gases were studied for all deposited thin films, and display the conclusions and suggestions for future work.

## 4.2 Structural and Surface Morphology for $Mg_xZnO_{1-x}$ Thin Films

In this section, have been studied the effect of different Mg-contents (0,30,50,70,and 90)%, and substrate temperatures (400,450,and 500)$^{o}$C on the structural and surface morphology properties for $Mg_xZnO_{1-x}$ thin films.

### 4.2.1 X-Ray Diffraction Maesurments

XRD technique is used to find out the nature of the crystal structure and main crystalline phases and the direction of the films prepared in certain conditions, as well as to identify some of the structural parameters such as crystalline size and full width at half maximum (FWHM).

The substrate temperature ($T_s$) plays an important role in determining the structure of $Mg_xZnO_{1-x}$ alloy films which are fabricated on glass and silicon substrates. Fig.4.1 shows the XRD measurements results that were formed at substrate temperatures of (400, 450, and 500) $^{o}$C, for range from ($20^{o}$-$60^{o}$), on glass substrate, at nitrogen pressure (4.5) bar, and constant thickness. It can be seen that the film is less crystallized at $T_s$= (400) $^{o}$C. When the substrate temperature ($T_s$) increased to (450) $^{o}$C, as shown in fig.4.1(450) $^{o}$C, there are three diffraction peaks located at (2θ =31.7˚,34.38˚,and 36.35˚), are found, which belong to ZnO: (100), (002), and (101) orientations, respectively.

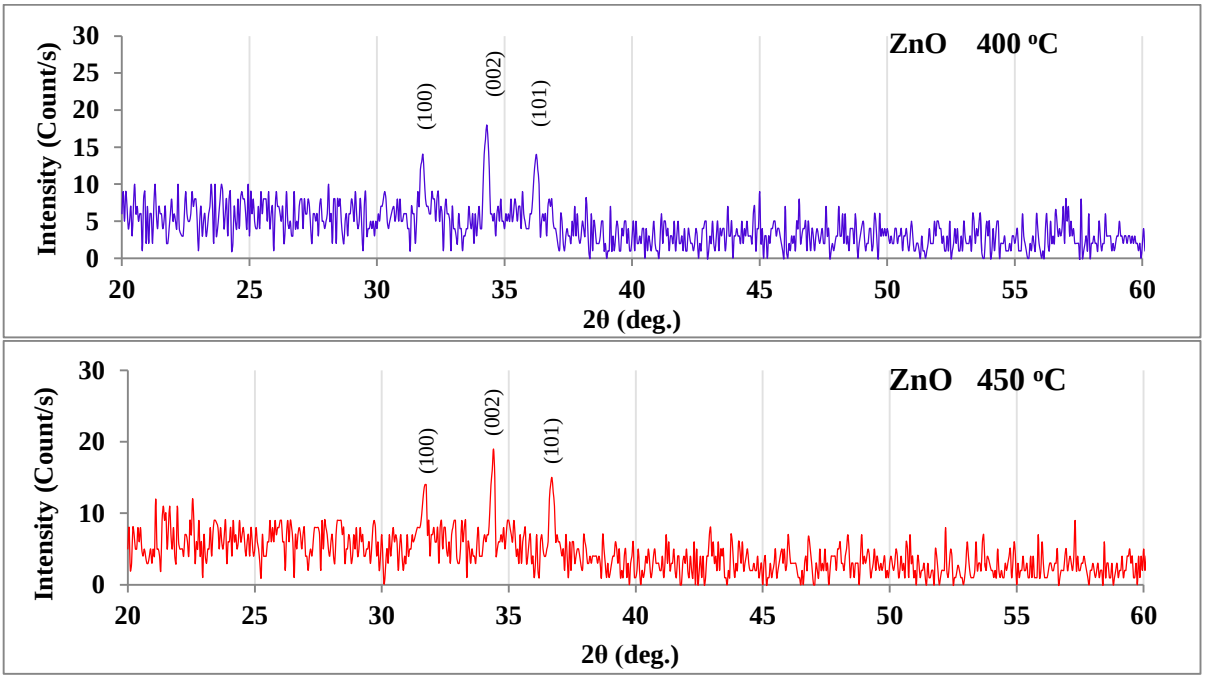

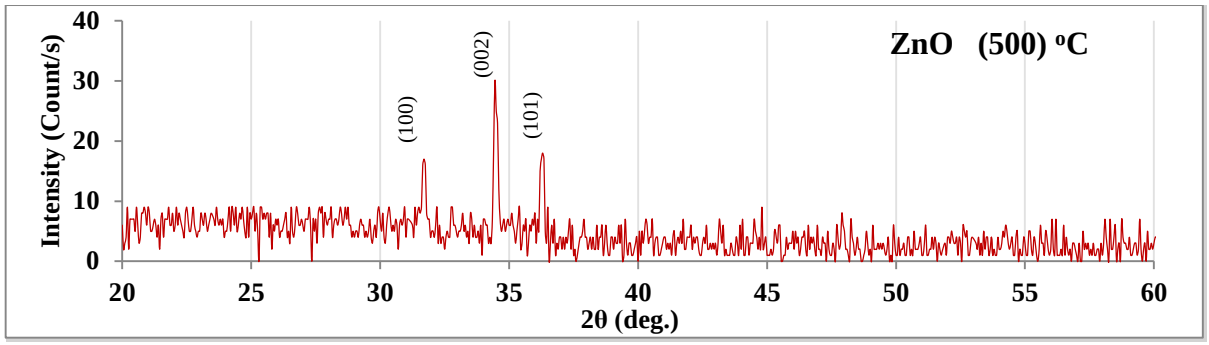


Fig.4.1: XRD Patterns for ZnO Thin Films with Different Substrate Temperatures

When the substrate temperature is (500) ºC as shown in fig.4.1 (500) ºC, the (100), (002), and (101) peaks is becoming fine line width, suggesting that pure c-oriented ZnO films are obtained. The above XRD results indicate that the structure of the films changed from less crystallized to higher crystallization with the increasing of the temperature.

Furthermore, the Zn-O bonds along the c- axis are longer than the other Zn-O bonds which means that the Zn-O bond energy along (002) direction is the smallest. The film-growth along this direction needs to higher kinetic energy than that along other

directions.Then in the substrate temperature at (450) ºC is best to the growth of (002) oriented ZnO films. The deposits at the substrate temperature (500) ºC, ZnO thin film increases crystallinty, but decreases the c- axis as the fig4.1 (450) ºC. The hexagonal phase appears at ($2\theta=34.38^{\circ}$) (002),because the change ZnO phase from hexagonal to hexagonal wurtzite occurs at temperatures higher than (400) ºC. Fig.4.1 (500) ºC shows the full width at half maximum (FWHM) of the ZnO thin films grown on glass at above substrate temperature, where the (FWHM) of the (002) peaks decreases with increasing of the substrate temperatures. This is related to the migration and diffusion rate of Zinc and oxygen atoms. At low temperature, the Zn and O atoms have no energy to migrate to the normal lattice site. This leads to increase in (FWHM) of (002) peak and decrease in crystellite size. But at high temperature grains have enough energy to combine together to form large grains, which leads to decrease of the (FWHM) of (002) peak.

From table 4.1, it is clear that the crystalline size at low temperature is lower compared with the high temperature and increases with increasing of substrate temperature. Tables (4.1,and 4.2) shows all the peaks observed in all films and comparison between the experimental and standard value of ($d_{hkl}$ ) according cards(JCPDS data card no. S6 –314, and JCPDS card no. 71-1176).

Table 4.1: Structural Properties of ZnO Thin Films prepared on Glass Substrate at Different Substrate Temperatures

| **Substrate Temperature ($^oC$)** | **(hkl)** | **2θ (deg.)** | **$d_{hkl}$ (Exp.) (nm)** | **$d_{hkl}$ (Std.) (nm)** | **FWHM (deg.)** | **Crys. size Ds(nm)** | **$\delta_D \times 10^{14}$ (lin $m^{-2}$)** | **$S \times 10^{-2}$ (lin$^{-2}$m$^{-4}$)** | ($N_\ell$ ) |
|---|---|---|---|---|---|---|---|---|---|
| **400** | (100) | 31.65 | 2.823 | 2.81 | 0.367 | 45.08 | 4.921 | 8.827 | 1.775 |
| | (002) | 34.32 | 2.610 | 2.60 | 0.400 | 41. 62 | 5.773 | 9.555 | 3.411 |
| | (101) | 36.25 | 2.475 | 2.47 | 0.330 | 50.68 | 3.893 | 7.840 | 1.579 |
| **450** | (100) | 31.70 | 2.819 | 2.81 | 0.241 | 68.60 | 2.125 | 5.795 | 1.166 |
| | (002) | 34.38 | 2.605 | 2.60 | 0.352 | 47. 30 | 4.470 | 8.407 | 1.691 |
| | (101) | 36.70 | 2.446 | 2.47 | 0.208 | 80.58 | 1.540 | 4.935 | 0.993 |
| **500** | (100) | 31.55 | 2.832 | 2.81 | 0.248 | 66.56 | 2.256 | 5.966 | 1.202 |
| | (002) | 34.44 | 2.600 | 2.60 | 0.270 | 61.60 | 2.635 | 6.447 | 1.299 |
| | (101) | 36.25 | 2.475 | 2.47 | 0.218 | 76.64 | 1.703 | 5.179 | 1.044 |

The film quality can improve with the increase of the substrate temperature. This is because the atoms at lower temperatures do not have enough energy to locate their right position [116]. It is seen from the fig.4.1 at (500)$^o$C that the relative intensity of the (002) peak increases with increasing substrate temperature. The increase in peak intensity indicates an improvement in the crystallinity of the films. This leads to decrease in full width at half maximums (FWHM) of peak and increase in crystallite size are similar behavior into [117]. The (FWHM) of XRD depends on the crystalline quality of each grain and distribution of grain orientation. The (FWHM) is proportion Inversely with the crystallite size, as the mean crystallite size increases as shown in Fig. 4.1(500) $^o$C. The increasing of the substrate temperature is in favor of the diffusion of atoms absorbed on the substrate and accelerates migration of atoms to the energy favorable positions, resulting in the enhancement of the crystalline and c-axis orientation of film. Fig.4.2 shows X-ray diffraction patterns of ZnO films mixed with MgO at proportions (x=0,30,50,70, and 90)% under (4.5) bar nitrogen pressure, and at substrate temperatures (400,450, and 500)°C, by using

(CSP), deposited on glass substrates are shown in figs.(4.2-4.4). The XRD shows peaks position which shifted slightly from the data of (ASTM) cards at increased. Interplaner spacing ($d_{hk1}$) was determined using the Braggs relationship(2-1). From figs.(4.2,4.3,and 4.4) when x=(30)% $Mg_{0.3}ZnO_{0.7}$ thin films, three peaks appears belonging to the ZnO which located at ($2\theta$=31.70º, 34.75º, and 36.25°) respectively as shown in table 4.2,which corresponds to{(101), (002), and (101)} planes, but not appear to MgO peaks in this ratio x=(30)%, it indicates the crystal structure is hexagonal wartzite despite the blending ratio of MgO with ZnO, these results are similar behavior into [26].

When increase Mg-contents to the (x=50, 70, and 90)%, noted two peaks belonging to the MgO which located at ($2\theta$= 36.85°,and 42.85°),which corresponds to{(111), (200)} planes.In this case,the crystal structure is a mixed resulting from ZnO with MgO in the hexagonal structure phase. It is noticed that the intensity of {(100), (002), and (101)} reflections decreasing with the increasing Mg-content, while the intensity of {(111), and (200)} reflection increases with increasing Mg-contents, and the intensity of (200) reflection will be the prominent and controlling for other peak in MgO in all temperatures. This refers to the clear improvement in the crystalline properties of the films, where it is clear that (200) is the highest peak in intensity as shown in figs.(4.2-4.4).

These results are similar behavior into [38]. Fig.4.2 shows the XRD pattern of $Mg_xZnO_{1-x}$ thin films of various Mg-contents (x=0, 30,50,70, and 90)% deposited at substrate temperatures (400,450, and 500) °C. The XRD patterns reveal that the films with Mg-content, x=(50)%, show highly intense (111) diffraction peak along with (101) peak which corresponds to cubic MgO phase with impurity phase. The appearance of only (200) peak for films with increase higher Mg-content x=(90)% is the sign of cubic single phase indicating deviation from wurtzite to cubic rock-salt structure in $Mg_xZnO_{1-x}$ thin films with increase in Mg-content. The presence of (002) wurtzite reflection along with (200) cubic reflection at x=(70)% indicates the existence of two phases.

The observed deviation from wurtzite structure with increasing Mg-content is attributed to the fact that when the Mg and Zn atoms bond to the O atom, the Mg atom lose electrons more easily than the Zn atom because of the difference in electro negativities, (1.31 for Mg is smaller than that of the 1.65 for Zn). Moreover, the large angle between the nearest-neighbour Zn-O bonds than the nearest neighbor Mg-O bonds, this is leads to stronger interaction between the second nearest-neighbour Mg-O bonds due to the stronger polarity of the Mg-O bonds, and hence results in deviation of crystal structure from wurtzite as the quantity of the Mg-O bond is increased.

The position of (002) and (200) peak shifted to higher diffraction angles with the increase in Mg-content, which manifests itself by the c-axis compression. This shows the onset of lattice strain in the films due to the difference in ionic radii of $Mg^{+2}$(0.57) Å. and $Zn^{+2}$ (0.60) Å ions.

Figs. (4.5,4.6, and 4.7) shows the variation of c-axis lattice constant and crystallite size of $Mg_xZnO_{1-x}$ thin films for different Mg-content (x)%. The crystallite size was found to decrease from (41.62 to 34.78)nm with corresponding increase in Mg-content from (x=0 to 90)% at substrate temperature (400) $^oC$,(47.30 to 38.20) nm, at substrate temperature (450) $^oC$, and from (61.60 to 50.02) nm, at substrate temperature (500) $^oC$ as shown in tables (4.3,and 4.4).

The evaluated c-axis lattice constant decreased monotonically from (0.5220 to 0.5134)nm, at substrate temperature (400)$^oC$, (0.5210 to 0.5138)nm, at substrate temperature (450) $^oC$, and from (0.5200 to 0.5150)nm with increase in Mg-content, indicating c-axis compression as shown in figs.(4.5a,b,and c).

Table 4.2: The $D_s$, $\delta_D$, S, and $N_\ell$ of Layers Data of (002),(200) Orientations for $Mg_xZnO_{1-x}$ at Different Mg-Content, at Substrate Temperature (400) $^oC$.

| **Sample** | **hkl** | **2θ (deg.)** | **$d_{hkl}$ (Exp.) (nm)** | **$d_{hkl}$ (Std.) (nm)** | **FWHM (β) (deg.)** | **Crys. size $D_s$ (nm)** | **$\delta_D \times 10^{14}$ (lin $m^{-2}$)** | **$S \times 10^{-2}$ (lin$^{-2}$ $m^{-4}$)** | ($N_\ell$) |
|---|---|---|---|---|---|---|---|---|---|
| **ZnO** | (100) | 31.65 | 2.823 | 2.810 | 0.367 | 45.08 | 4.921 | 8.827 | 1.775 |
| | (002) | 34.32 | 2.610 | 2.600 | 0.400 | 41. 62 | 5.773 | 9.554 | 1.922 |
| | (101) | 36.25 | 2.475 | 2.470 | 0.330 | 50.68 | 3.893 | 7.840 | 1. 579 |

| | | | | | | | | | |
|---|---|---|---|---|---|---|---|---|---|
| $Mg_{0.3}ZnO_{0.7}$ | (100) | 31.70 | 2.819 | 2.810 | 0.314 | 52.58 | 3.617 | 7.551 | 1.521 |
| | (002) | 34.75 | 2.578 | 2.600 | 0.396 | 42.06 | 5.652 | 9.448 | 1.902 |
| | (101) | 36.25 | 2.475 | 2.470 | 0.287 | 58.24 | 2.948 | 6.818 | 1.374 |
| $Mg_{0.5}ZnO_{0.5}$ | (100) | 31.75 | 2.904 | 2.810 | 0.262 | 63.00 | 2.519 | 6.315 | 1.269 |
| | (002) | 34.80 | 2.575 | 2.600 | 0.447 | 37.24 | 7.211 | 10.663 | 2.148 |
| | (111) | 36.85 | 2.436 | 2.434 | 0.638 | 26.24 | 14.524 | 15.132 | 3.048 |
| | (200) | 42.85 | 2.108 | 2.106 | 0.703 | 24.32 | 16.907 | 16.360 | 3.289 |
| $Mg_{0.7}ZnO_{0.3}$ | (100) | 31.65 | 2.823 | 2.810 | 0.311 | 53.20 | 3.533 | 7.480 | 1.504 |
| | (002) | 34.65 | 2.586 | 2.600 | 0.577 | 28.84 | 12.023 | 13.770 | 2.774 |
| | (101) | 36.00 | 2.491 | 2.470 | 0.172 | 97.26 | 1.057 | 4.089 | 0.823 |
| | (111) | 36.87 | 2.435 | 2.434 | 0.458 | 36.56 | 7.481 | 10.862 | 2.188 |
| | (200) | 42.88 | 2.106 | 2.106 | 0511 | 33.44 | 8.943 | 11.890 | 2.392 |
| $Mg_{0.9}ZnO_{0.1}$ | (100) | 31.75 | 2.904 | 2.810 | 0.182 | 90.88 | 1.211 | 4.387 | 0.880 |
| | (002) | 34.50 | 2.596 | 2.600 | 0.147 | 113.60 | 0.775 | 3.509 | 0.204 |
| | (111) | 36.82 | 2.438 | 2.434 | 0.410 | 40.88 | 5.984 | 9.725 | 1.956 |
| | (200) | 42.85 | 2.108 | 2.106 | 0.491 | 34.78 | 8.267 | 11.426 | 2.300 |

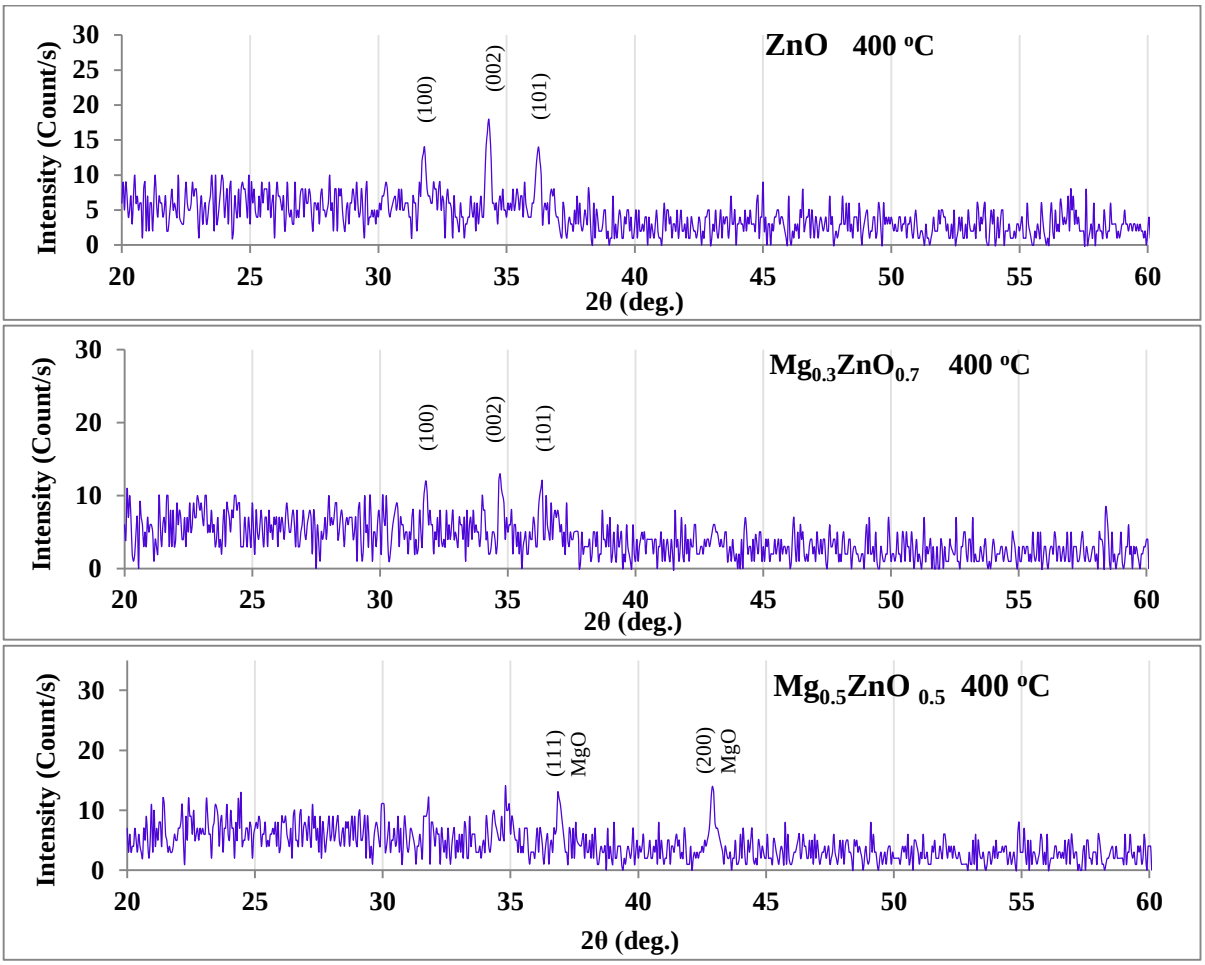

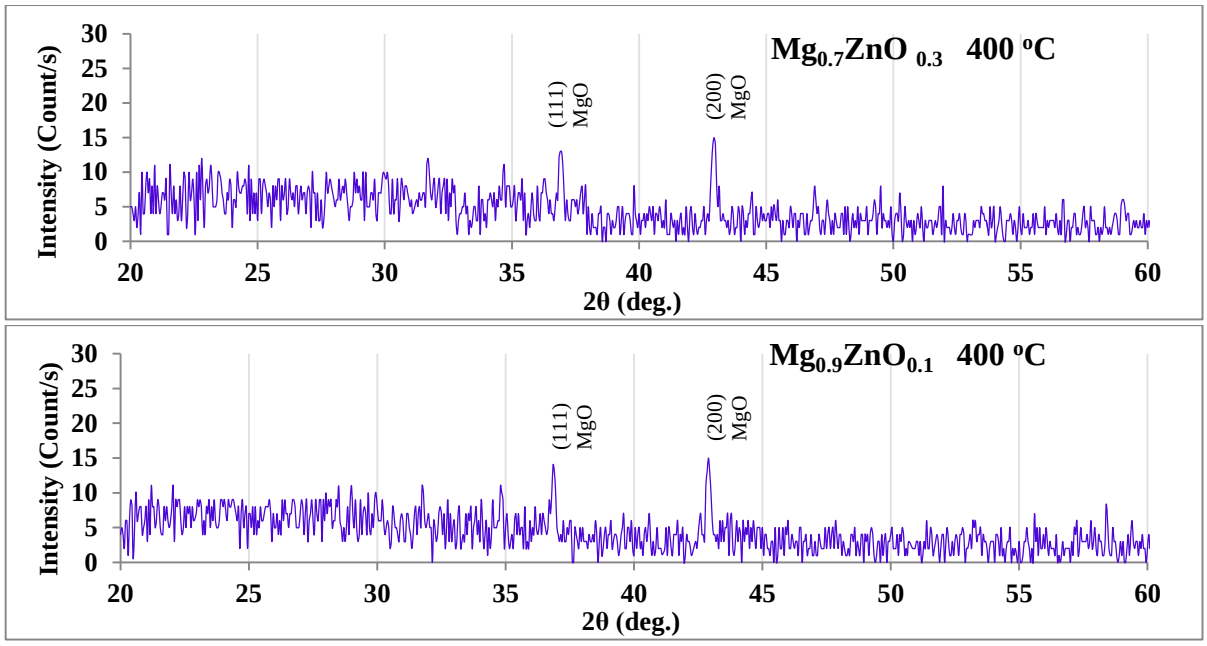


Fig.4.2:XRD Patterns for $Mg_xZnO_{1-x}$ Thin Films Mg-Contents (0,30,50,70,and 90)% , at Substrate Temperature (400) ºC.

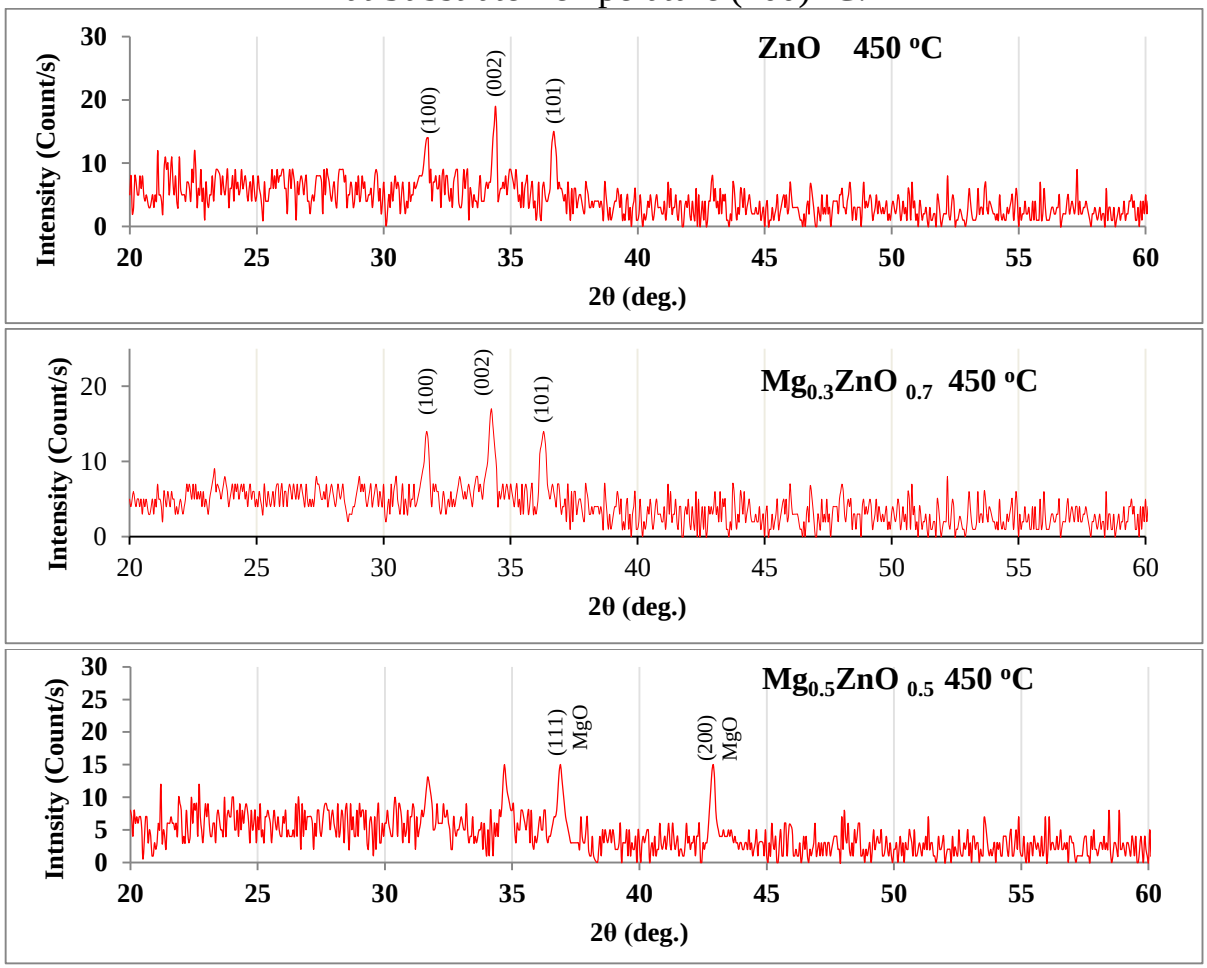

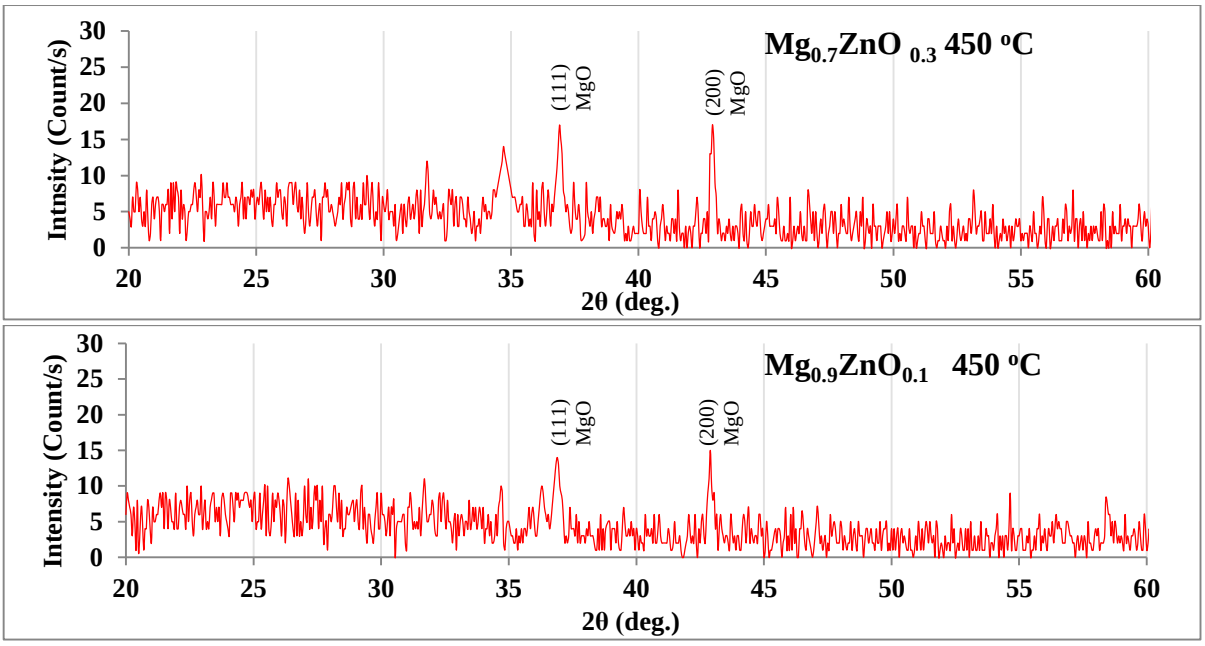


Fig.4.3: XRD Patterns for $Mg_xZnO_{1-x}$ Thin Films with Mg-Contents (0,30,50,70,and 90)% , at Substrate Temperature (450) °C.

Table 4.3: The $D_s$ , $\delta_D$, S, and $N_\ell$ of Layers Data of (002),(200) Orientations for $Mg_xZnO_{1-x}$ at Different Mg-Content, and at Substrate Temperature (450) °C.

| Sample | Investigated line(hkl) | 2θ (deg.) | d(nm) | FWHM (β) (deg.) | Crys. size $D_s$(nm) | $\delta_D \times 10^{14}$ (lin $m^{-2}$) | $S \times 10^{-2}$ (lin$^{-2}$ $m^{-4}$) | ($N_\ell$) |
|---|---|---|---|---|---|---|---|---|
| **ZnO** | (100) | 31.70 | 2.819 | 0.241 | 68.60 | 2.125 | 5.795 | 1.166 |
| | (002) | 34.38 | 2.605 | 0.352 | 47.30 | 4.469 | 8.406 | 1.691 |
| | (101) | 36.70 | 2.446 | 0.208 | 80.58 | 1.540 | 4.935 | 0.993 |
| **$Mg_{0.3}ZnO_{0.7}$** | (100) | 31.65 | 2.823 | 0.281 | 58.74 | 2.898 | 6.758 | 1.362 |
| | (002) | 34.77 | 2.577 | 0.320 | 52.00 | 3.698 | 7.634 | 1.538 |
| | (101) | 36.35 | 2.468 | 0.244 | 68.60 | 2.124 | 5.795 | 1.662 |
| **$Mg_{0.5}ZnO_{0.5}$** | (100) | 31.64 | 2.824 | 0.235 | 63.00 | 2.519 | 5.652 | 1.269 |
| | (002) | 34.70 | 2.582 | 0.419 | 70.34 | 2.021 | 9.354 | 1.137 |
| | (111) | 36.85 | 2.436 | 0.473 | 35.40 | 7.979 | 11.218 | 2.259 |
| | (200) | 42.85 | 2.108 | 0.540 | 31.60 | 10.014 | 12.567 | 2.531 |
| **$Mg_{0.7}ZnO_{0.3}$** | (100) | 31.63 | 2.825 | 0.300 | 55.10 | 3.293 | 7.216 | 1.452 |
| | (002) | 34.75 | 2.578 | 0.392 | 42.50 | 5.536 | 9.352 | 1.882 |
| | (111) | 36.90 | 2.433 | 0.413 | 40.58 | 6.072 | 9.794 | 1.972 |
| | (200) | 42.80 | 2.110 | 0.452 | 37.76 | 7.013 | 10.520 | 2.118 |
| **$Mg_{0.9}ZnO_{0.1}$** | (100) | 31.72 | 2.818 | 0.138 | 119.48 | 0.700 | 3.318 | 0.669 |
| | (002) | 34.70 | 2.582 | 0.120 | 138.60 | 0.520 | 2.863 | 0.577 |
| | (101) | 36.25 | 2.475 | 0.388 | 43.10 | 5.383 | 9.218 | 1.856 |
| | (111) | 36.85 | 2.436 | 0.373 | 44.92 | 4.955 | 8.847 | 1.781 |
| | (200) | 42.87 | 2.107 | 0.448 | 38.20 | *6.852* | 10.425 | 2.094 |

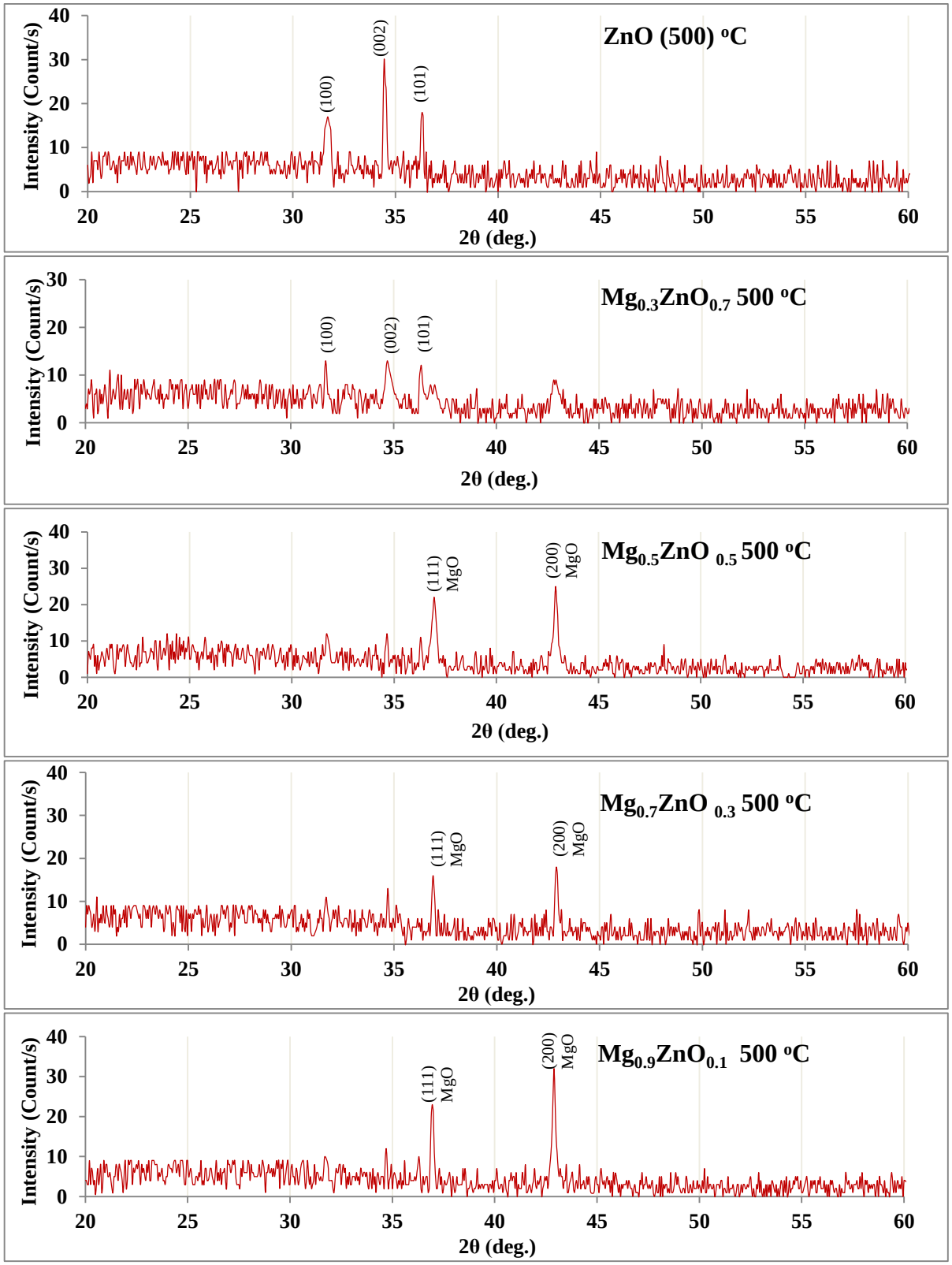


Fig.4.4: XRD Patterns for $Mg_xZnO_{1-x}$ Thin Films with Mg-Contents (0,30,50,70,and 90)% , at Substrate Temperature (500) ºC.

Table 4.4: The $D_s$ , $\delta_D$, S, and $N_\ell$ of Layers Data of (002),(200) Orientations for $Mg_xZnO_{1-x}$ at Different Mg-Content, and at Substrate Temperature (500) ºC.

| Sample | Investigated line(hkl) | 2θ (deg.) | d(nm) | FWHM (β) (deg.) | Crys. size $D_s$(nm) | $\delta_D \times 10^{14}$ (lin $m^{-2}$) | $S \times 10^{-2}$ (lin$^{-2}$ $m^{-4}$) | ($N_\ell$) |
|---|---|---|---|---|---|---|---|---|
| **ZnO** | (100) | 31.55 | 2.832 | 0.248 | 66.56 | 0.903 | 5.966 | 1.202 |
| | (002) | 34.44 | 2.600 | 0.270 | 61.60 | 1.054 | 6.447 | 1.299 |
| | (101) | 36.25 | 2.475 | 0.218 | 76.64 | 0.681 | 5.179 | 1.044 |
| **$Mg_{0.3}ZnO_{0.7}$** | (100) | 31.65 | 2.823 | 0.261 | 63.28 | 0.999 | 6.277 | 1.264 |
| | (002) | 34.47 | 2.599 | 0.340 | 48.94 | 1.670 | 8.118 | 1.635 |
| | (101) | 36.30 | 2.471 | 0.224 | 74.62 | 0.718 | 5.321 | 1.072 |
| **$Mg_{0.5}ZnO_{0.5}$** | (100) | 31.54 | 2.834 | 0.221 | 74.70 | 0.717 | 5.317 | 1.071 |
| | (002) | 34.52 | 2.595 | 0.386 | 43.12 | 2.151 | 9.215 | 1.855 |
| | (101) | 36.32 | 2.471 | 0.218 | 76.78 | 0.680 | 5.178 | 1.043 |
| | (111) | 36.92 | 2.432 | 0.430 | 38.94 | 2.637 | 10.196 | 2.054 |
| | (200) | 42.84 | 2.108 | 0.529 | 32.24 | 3.848 | 12.310 | 2.481 |
| **$Mg_{0.7}ZnO_{0.3}$** | (100) | 31.70 | 2.819 | 0.289 | 57.12 | 1.225 | 6.950 | 1.401 |
| | (002) | 34.65 | 2.586 | 0.347 | 47.96 | 1.739 | 8.280 | 1.668 |
| | (111) | 36.87 | 2.435 | 0.437 | 38.30 | 2.726 | 10.364 | 2.088 |
| | (200) | 42.86 | 2.107 | 0.431 | 39.58 | 2.553 | 10.030 | 2.021 |
| **$Mg_{0.9}ZnO_{0.1}$** | (100) | 31.64 | 2.824 | 0.123 | 134.24 | 0.222 | 2.958 | 0.591 |
| | (002) | 34.68 | 2.583 | 0.114 | 145.96 | 0.187 | 2.720 | 0.548 |
| | (101) | 36.29 | 2.472 | 0.356 | 46.94 | 1.815 | 8.457 | 1.704 |
| | (111) | 36.95 | 2.430 | 0.350 | 47.84 | 1.747 | 8.299 | 1.672 |
| | (200) | 42.87 | 2.107 | 0.356 | 50.02 | 1.597 | 8.277 | 1.594 |

A deviation from the linearity in the c-axis length with increase in Mg-content at x≥(50)% only at substrate temperature(400)ºC could be due to the interstitial incorporation of Mg atoms in the $Mg_xZnO_{1-x}$ thin films and to the non-solubility limit of the Mg-precursor in the solution at higher Mg concentration. This is expected for an Mg-substituted ZnO solid solution as the ionic radius of $Mg^{+2}$ is smaller than that of $Zn^{+2}$. Figs.(4.2,and 4.3) shows XRD pattern of $Mg_xZnO_{1-x}$ x=(30)% films deposited at different substrate temperatures ($T_s$) in the range from (400 to 500) °C. XRD pattern revealed that the film deposited at $T_s$> (450) °C was highly oriented along the c-axis and exhibits preferred (002) orientation that is, the c-axis of the crystal lattice is normal to the plane of the substrate. The absence of (002) preferential orientation at low temperature reveals the suppressing effect of low temperature on the (002) direction growth. This may be due to the fact that there is no enough energy at low temperatures for atoms to move to low-energy sites, which induces strain in the films. As the temperature increases to (500)°C, there is a

significant contribution in the (002) direction. The results show that the increase of substrate temperature is in favour to the diffusion of atoms absorbed on the substrate and accelerates the migration of atoms to the energy favourable positions, resulting in the enhancement of the crystallinity and c-axis orientation of film, which is indicated by the increase in intensity of (002) reflection and decrease of (FWHM).

**4.2.2 Lattice Constants (a ,and c)**

The lattice constants (a, and c) which belong to the (002) plane as a preferred orientation for the ZnO thin film, and (101) plane as a preferred orientation for the $Mg_xZnO_{1-x}$ thin films for different Mg-contents (x=30, and50)%. As for the concentrations (x=70,and 90)% they belong to (200) plane , due to the modification from the mixed phase to cubic rock-salt phase. The (a, and c) lengths determined by XRD are plotted as a function of Mg-content as shown in fig. 4.5. This figure a-axis lengths increase when increasing Mg-content from (x=0 to 90)%, while the c-axis length

decrease. But at higher substrate temperatures, the constants propulsion changed slightly.

It is thought that the decreasing of c-axis lattice constant comes from increasing the number of $Mg^{+2}$ ions incorporated into the interstitial sites and is assumed also that the c-axis lattice constant decreases slightly due to the increase of the number of substitutional $Mg^{+2}$ ions, because the radius of $Zn^{+2}$ ions is a little greater than that of radius $Mg^{+2}$ ion, the decrease of the number of $Zn^{+2}$ ion in the Zn lattice sites will compress the lattice constant, are similar behavior into [39].

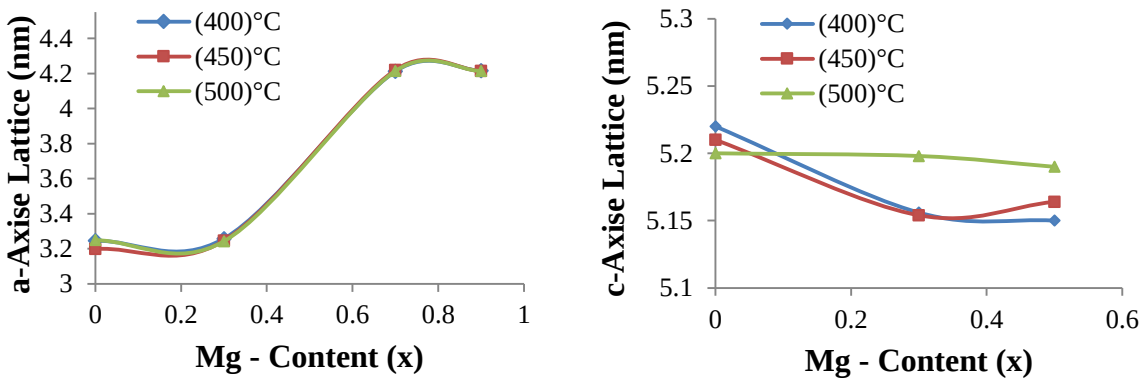


Fig.4.5: Variation of (a and c axis) Lattice Constants vs. Different Mg-Content for $Mg_xZnO_{1-x}$ Thin films.

### 4.2.3 Full Width at Half Maximum

(FWHM) by which who can know the preferred orientation (002) for ZnO pure and (101) for MgZnO are increase with increasing Mg-content and different temperatures in the film as shown in fig. 4.6a. It is inversely proportional to the crystallite size and thereby increase Mg-content increases the (FWHM), and decrease crystallite size as shown in the tables (4.2,4.3, and 4.4).

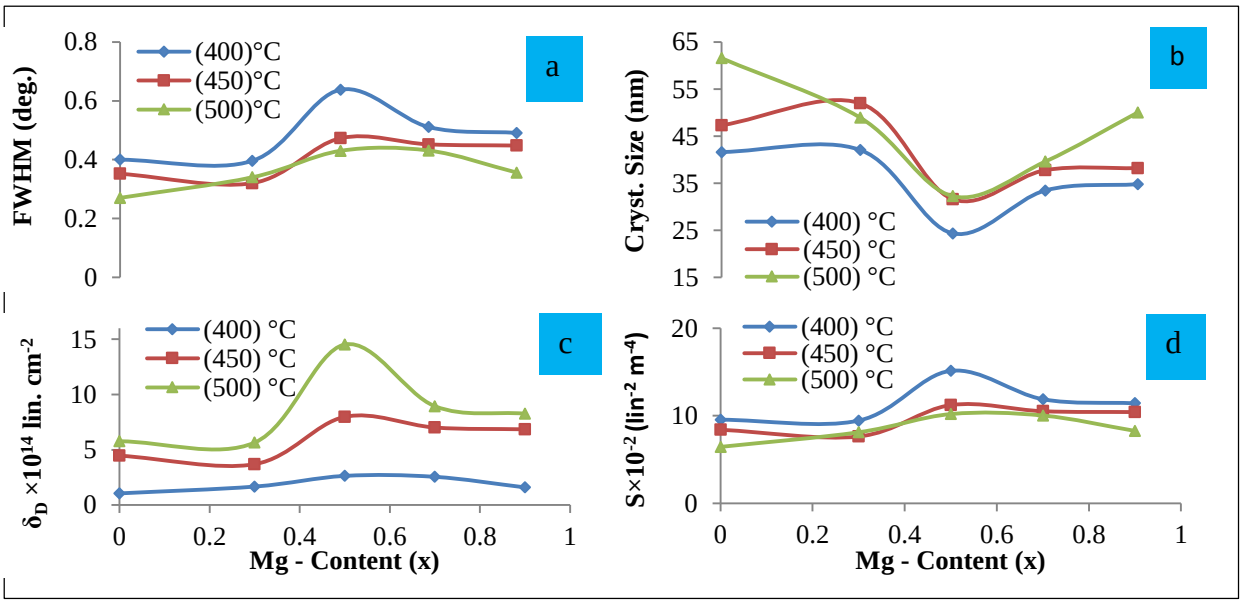


Fig.4.6: Variation of FWHM, $D_S$ ,S, and $\delta_D$ vs. Different Mg-Content for $Mg_xZnO_{1-x}$ Thin Films, and at Substrate Temperatures(400,450, and 500)°C.

### 4.2.4 Average Crystallite Size

The crystallite size of $Mg_xZnO_{1-x}$ thin films prepared at different Mg-contents (x=0,30,50,70, and 90)%, at substrate temperatures (400,450, and 500)°C was

calculated using the (FWHM) of the (002) peak for ZnO and (101) peak for MgZnO films using Debye Scherrers formula. The film prepared at Mg-content, (x=0) showed the highest average crystallite size of (68.26) nm at temperature (500) $^{o}$C for pure ZnO as shown in table 4.1, and its value decreases with adding Mg-content in the films as shown in tables (4.3, and 4.4) and fig.4.6b. The decrease in cell volume indicates disorder, which may be due to compression stresses in the films or substitution of elements of small size for elements of large size.

The XRD peaks can be widened (FWHM increase) by internal stress and defect when increasing Mg-content in the films, so the crystallite size decreases with increasing Mg-content. But at high temperatures increases crystallity due to kinetic energy sufficient for migration of atoms to their original positions, as shown in the table 4.3, and therefore decreases defects and stresses in the films. When a temperature increase of more than (450) $^{o}$C note the appeared some of the side distractions, it is supposed that the appearance of this behavior due to increased collisions between atoms, and thereby increase the defects again, this behavior will be at (500) $^{o}$C.

### 4.2.5 Microstrains

The amount of microstrain was calculated for all films by using the relationship (2-5), values microstrain which is illustrated by fig. 4.6d.

### 4.2.6 Dislocation Density

The amount of dislocation density is caused by the grain size was calculated by using equation (2-6). Fig. 4.6c, the relationship between the density of dislocation and the Mg-content in the films. It is noticed that the value decreases with increasing impurities, which means a decrease dislocations (increase crystallite size). This means improving the crystal structure, as is illustrated by the mathematical relationship between them, as appropriate density of dislocation inversely with the square the crystallite size. But when you continue to increase the impurities more than the percentage (30)% impurities become a new defects leading to an increase in

the density of dislocation. In addition, the transfer from the hexagonal wurtzite type crystal structure into mixed structure at high percentages of impurities (50 and 70)%.

In the ratios which are greater than (70)% are transferring from mixed phase to the cubic rock salt phase. As for the effect of temperature too is clear, when the temperature increases, there is less dislocation density as shown in fig.4.6d. The number of layers are calculated from the thickness and grain size.

It is noted that the number of layers are changed with Mg-content in random way. It believes that the substrate temperature and droplet size plays a great role in this random change.

**4.3 Atomic Force Microscopy**

The study of film surfaces is deposited important to recognize how the distribution and arrangement of atoms on surfaces, and get to know the differences or homogeneity properties or attributes relating to each atom separately, can through microscopic analysis AFM study the effect of the parameters (thickness, temperature, method of preparation etc.) on the properties of film material deposited.

As well as analysis of the AFM can calculate the thickness of film, roughness and grain size, and gives an illustrative picture of the distribution of the particle size of the crystal on the surface rate. The three dimensional (3-D) AFM images and granularity accumulation distribution charts for ZnO pure and mixed MgO deposited on glass substrates with different Mg-contents(0,30,50,70, and 90)%, and varies substrate temperatures (400,450,and 500)$^{o}$C as shown in figs.(4.7,4.8,and 4.9) respectively.

The shapes shown 3-D, granularity normal distribution and appearance, graphic granular aggregates formed in the film and grain boundaries of mixed $Mg_xZnO_{1-x}$ thin films.

The white areas in this figure represent the formation of agglomerated grains one on the top of the other. In these areas, it is supposed that the neighboring grain comes together form large groups. So grain in white areas are larger compared with other

grains. From all of these interpretations, the film growth mechanism is thought to be formed firstly layer by layer and then island growth type [118].

All the AFM images were measured over an area of (2000×2000) $nm^2$. The average grain size of the particles is in nanoscale. Average diameter, total grain size ,surface thickness, roughness, and root mean square (RMS) values were listed in table 4.5.

Figs.(4.7,4.8,and 4.9) shows a 3-D images of the pure ZnO films, (400,450, and 500)$^oC$ where it is noticed that the topography of the surface and the appearance of grain has been formed on the surface of the films, and these images, are found that the surface thickness equal to (12,13.58,and 19.29)nm, respectively these values represents the thickness of the film surface roughness, which represents the highest granular crystalline peaks on the surface, also note the regularity of growth in the film, knowing that grained arrangement vertically to the axis of crystallization varying heights.

Through the figure was found that the average roughness equal to (0.654,1.46, and 1.98) nm,respectively. As it turns out that the average value of the (RMS) equal to (0.754,1.71,and 2.28)nm, respectively because they represent (the highs and lows space squared divided by all numbers under the square root) and this values is interpreted as the highest surface roughness (RMS) which is signified by the increase in surface roughness of the film. The figs.(4.7,4.8,and 4.9) on the right side drawing chart the distribution of grain aggregates of ZnO film surface.

It has been found that the average diameter equal to (90.19,76.12,and 97.48) nm respectively, and the graph shows how the distribution of aggregates grain sizes on the surface of the film of certain percentages.

The figs.(4.7,4.8,and 4.9) shows AFM images of the surface of the $Mg_xZnO_{1-x}$ thin films increase Mg-contents (30 to 90)%, showed the following results:

- Diameter average decreases with increasing Mg- contents in low ratios and increases at high Mg-content ratios and have the same behavior for the total grain number at the temperature of (400) °C, either at a temperature of (450, and 500) °C be behavior an opposite, see table 4.5.
- Large grain growth with increasing Mg-content leads to an increase in surface roughness and this clearly shows at (400) $^{o}$C, but this behavior is the opposite at high temperatures (450, and 500) $^{o}$C as shown in table 4.5. Increases (RMS) with increase the Mg-contents in the films at substrate temperature of(400) $^{o}$C, and the average of roughness exhibits the same behavior, while at substrate temperatures (400,and 500) $^{o}$C decreases (RMS).
- Decrease the thickness of the surface with increasing Mg-contents at substrate temperatures (400, and 450) $^{o}$C, while the note to increase the surface thickness randomly at substrate temperature (500) °C.

Table 4.5: Average Diameter,Total Grain No., Surface Thickness, Roughness Average and Root Mean Square for $Mg_xZnO_{1-x}$ Thin Films at Mg-Contents (0,30,50,70, and 90)%, and at Substrate Temperatures (400, 450,and 500) $^oC$.

| **Glass Substrate** | | | **$T_s$ =(400) $^oC$ , Thickness = (80)nm** | | |
|---|---|---|---|---|---|
| ***Content (x)*** | ***Average Diameter (nm)*** | ***Total Grain No. (nm)*** | ***Surface Thickness (nm)*** | ***Roughness Average (nm)*** | ***Root Mean Square (nm)*** |
| ZnO (pure) | 90.160 | 185 | 12.00 | 0.654 | 0.754 |
| $Mg_{0.3}ZnO_{0.7}$ | 76.350 | 208 | 11.54 | 3.240 | 3.800 |
| $Mg_{0.5}ZnO_{0.5}$ | 68.540 | 273 | 3.55 | 1.000 | 1.170 |
| $Mg_{0.7}ZnO_{0.3}$ | 121.300 | 064 | 2.16 | 2.420 | 2.750 |
| $Mg_{0.9}ZnO_{0.1}$ | 109.670 | 126 | 3.30 | 0.957 | 1.100 |
| **Glass Substrate** | | | **$T_s$ =(450) $^oC$ , Thickness = (80)nm** | | |
| ***Content (x)*** | ***Average Diameter (nm)*** | ***Total Grain No. (nm)*** | ***Surface Thickness (nm)*** | ***Roughness Average (nm)*** | ***Root Mean Square (nm)*** |
| ZnO (pure) | 76.120 | 279 | 13.58 | 1.460 | 1.710 |
| $Mg_{0.3}ZnO_{0.7}$ | 103.640 | 163 | 3.48 | 0.485 | 0.573 |
| $Mg_{0.5}ZnO_{0.5}$ | 92.610 | 189 | 5.15 | 0.898 | 1.040 |
| $Mg_{0.7}ZnO_{0.3}$ | 101.880 | 147 | 3.11 | 0.528 | 0.610 |
| $Mg_{0.9}ZnO_{0.1}$ | 81.550 | 136 | 3.84 | 0.653 | 0.533 |
| **Glass Substrate** | | | **$T_s$ =(500) $^oC$ , Thickness = (80)nm** | | |
| ***Content (x)*** | ***Average Diameter (nm)*** | ***Total Grain No. (nm)*** | ***Surface Thickness (nm)*** | ***Roughness Average (nm)*** | ***Root Mean Square (nm)*** |
| ZnO (pure) | 97.480 | 157 | 3.39 | 1.980 | 2.280 |
| $Mg_{0.3}ZnO_{0.7}$ | 93.390 | 172 | 19.29 | 1.920 | 2.230 |
| $Mg_{0.5}ZnO_{0.5}$ | 75.550 | 231 | 6.62 | 0.788 | 0.899 |
| $Mg_{0.7}ZnO_{0.3}$ | 73.560 | 280 | 13.95 | 0.380 | 0.434 |
| $Mg_{0.9}ZnO_{0.1}$ | 78.090 | 237 | 4.99 | 0.465 | 0.533 |

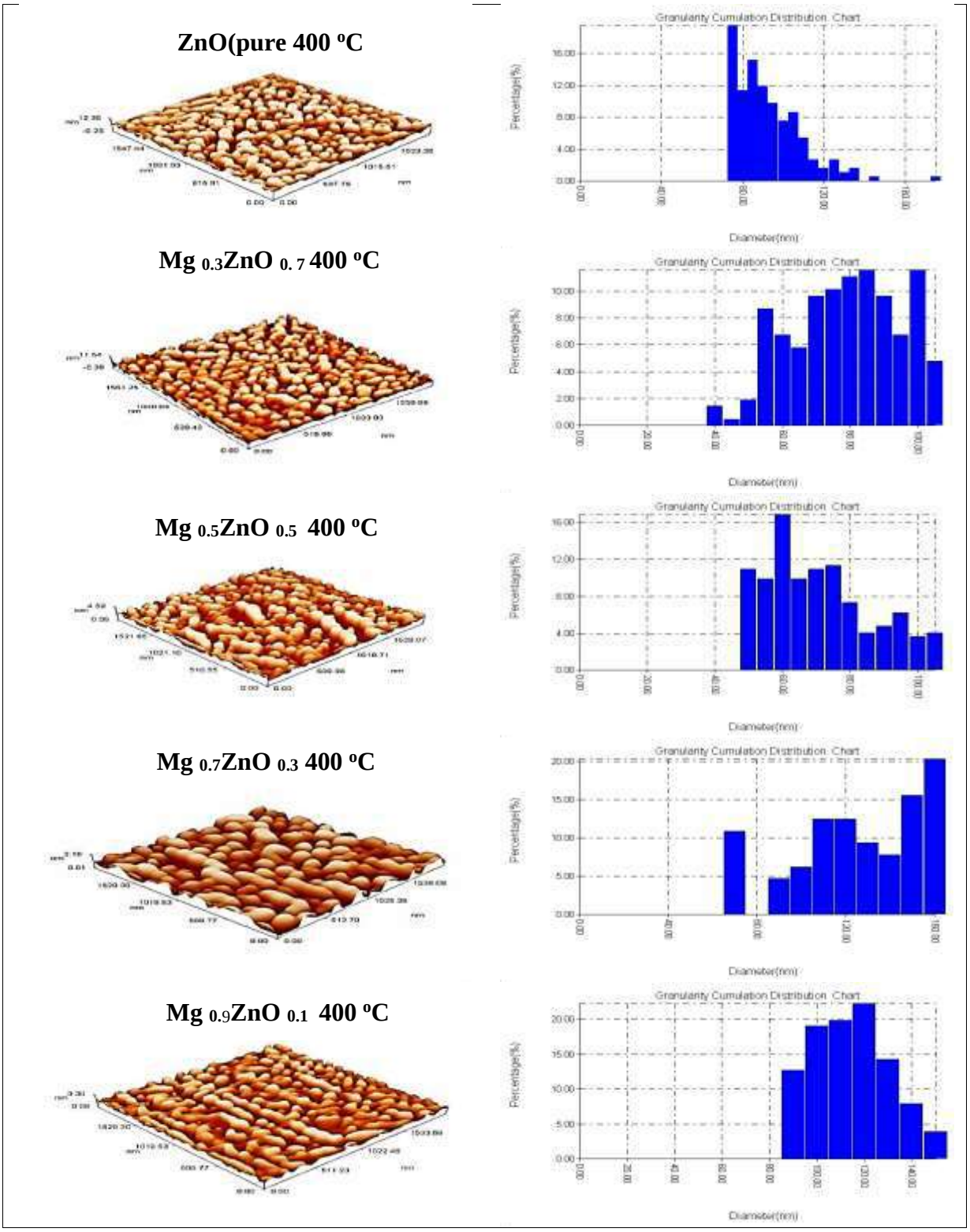


Fig.4.7:3-D AFM Image and Granularity Accumulation for $Mg_xZnO_{1-x}$ with Mg-Cntents (0,30,50,70, and 90)%, and at Substrate Temperature (400) ºC

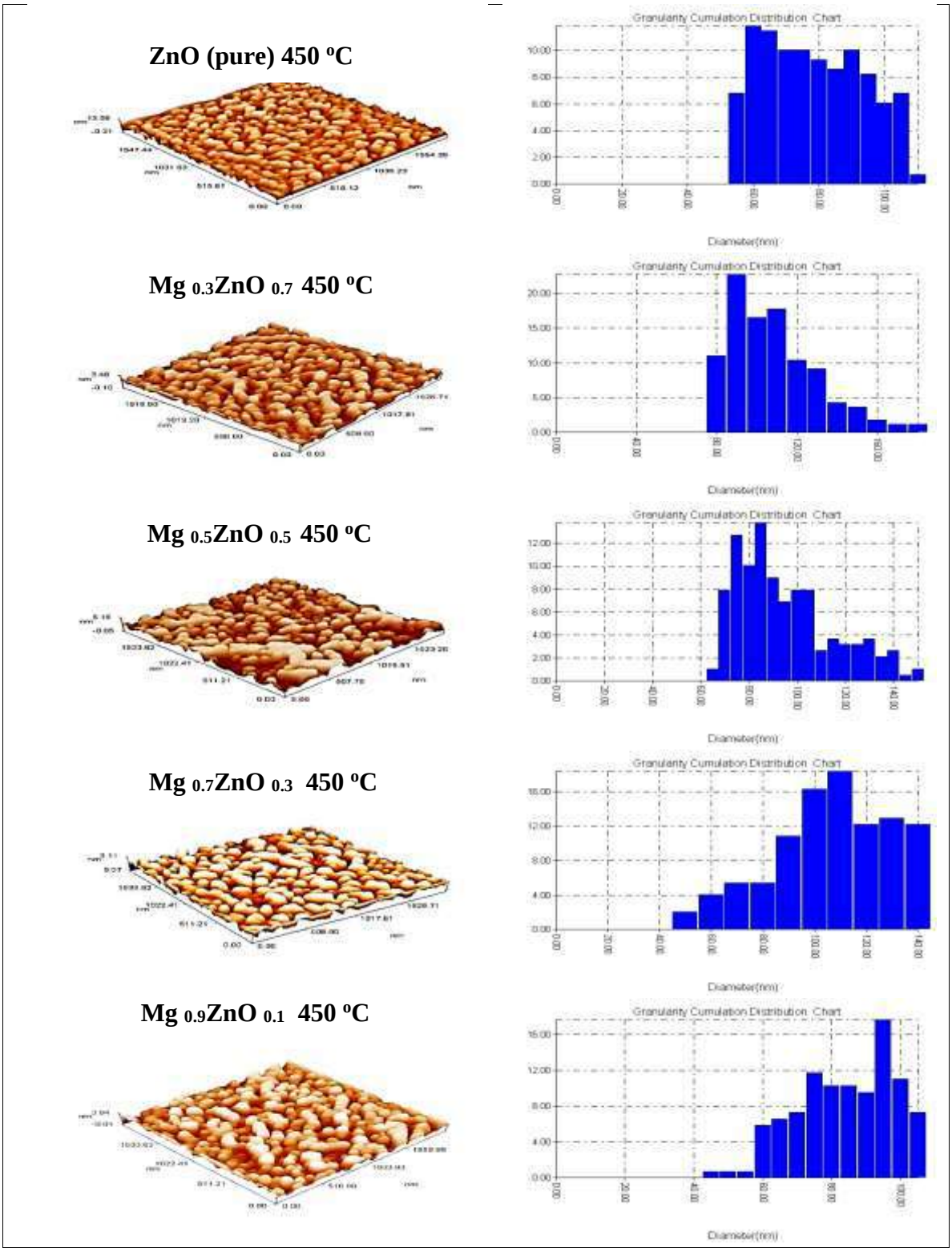


Fig. 4.8: 3-D AFM Image and Granularity Accumulation for $Mg_xZnO_{1-x}$ with Mg-Contents (0,30,50,70, and 90)%, and at Substrate Temperature (450) ºC

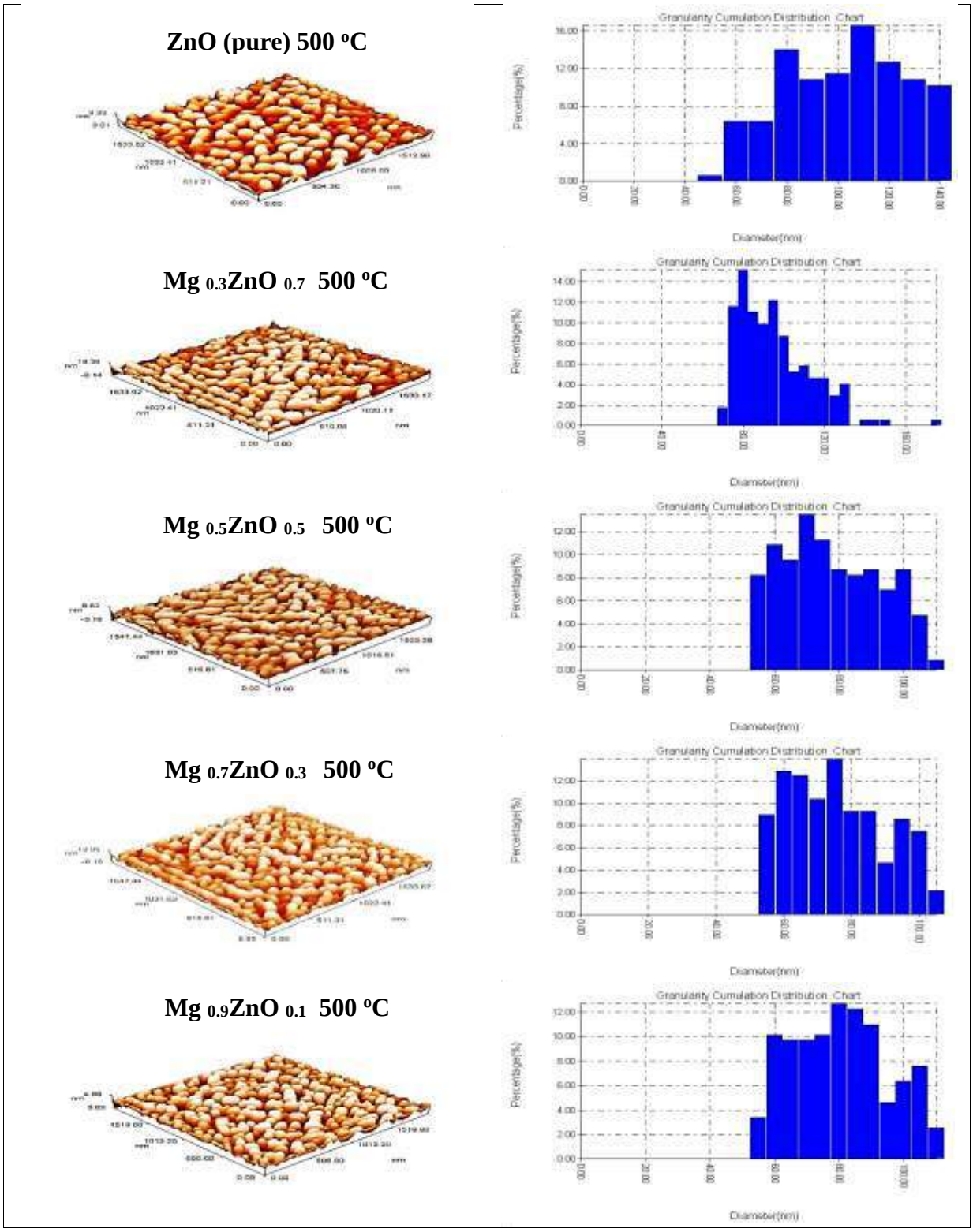


Fig. 4.9: 3-D AFM Image and Granularity Accumulation for $Mg_xZnO_{1-x}$ with Mg-Contents (0,30,50,70, and 90)%, and at Substrate Temperature (500) ºC.

## 4.4 Optical Properties for $Mg_xZnO_{x-1}$ Thin Films

Properties were studied optical pure ZnO and mixed $Mg_xZnO_{1-x}$ thin films with different Mg-contents (0,30,50,70, and 90)%, prepared on glass substrates and under

different temperatures (400,450, and 500) °C, by using (CSP) technique under a fixed preparation conditions. Transmittance, absorbance and reflectivity have been studied in the spectral range of (300-700)nm, and depending on the above characteristics have been identified some of the following optical constants: Optical energy gap ($E_g$), refractive index (n), extinction coefficient ($k_o$), real part ($\varepsilon_r$) and imaginary part ($\varepsilon_i$) for dielectric constants.

### 4.4.1 Messurements of Transmission Spectrum for $Mg_xZnO_{1-x}$ Thin Films

The optical properties of the $Mg_xZnO_{1-x}$ thin films nanostructures were studied by UV–Vis absorption spectroscopy. Fig.4.10 shows the room temperature optical absorption spectra of pure ZnO and $Mg_xZnO_{1-x}$ thin films nanoparticles. Mg mixing shifts the absorption onset to (368–350) nm of Mg-content from (0 to 90)%, indicating an increase in the energy gap from (3.18 to 3.31) eV.

The shifts in the optical energy gap in ZnO caused by mixing with Mg ions are shown in fig. 4.10a. The increase of energy gap is attributed to the decrease of particle size of $Mg_xZnO_{1-x}$ thin films nanoparticles, and also due to the influence of mixed ions. Moreover, with the increase in Mg-content, the band edge shifts toward the lower wavelength (higher energy) side.

The results of the energy gap are similar behavior into [119].The transmittance spectra of the mixed $Mg_xZnO_{1-x}$ thin films in the spectral range of (300-700) nm are compared as a function of Mg-content (x), as shown in fig.4.10a. The average transmittance in the wavelength of visible region (430-700) nm varies between (65-74)% , for x=0, pure ZnO at substrate temperature (400)$^o$C.

Displacement toward the shorter wavelength with increasing Mg-content clearly reflects the merger of Mg in the lattice of ZnO, indicating that the optical energy gap expanded with the addition of Mg regardless of crystallisation, are similar behavior into [14,39].

The transmittance at wavelength (430) nm was about (77)% at x=(30)% which increases to (90)% for x=(50)%, but then decreases to (83)% for x=(90)% and shifts towards wavelengths the lowest. The initial increase in transmittance could probably

be due to the increasing crystallinity of ZnO. The decrease in transmittance for x=(90)% may probably be due to the increasing Mg-content and temperature is not enough to move the atoms to the their original positions.

It is also noted that the best transmittance of the mixed thin films was at x=(50)% $Mg_{0.5}ZnO_{0.5}$. But when the temperature (450)$^{o}$C, the average transmittance in the visible region of the wavelength was (76-82)% x=0, pure ZnO, as shown in fig.4.10b.

The transmittance at wavelength (430) nm was about (43)% at x=(30)% , which increases to (81)% for x=(50)%. Continue to increase with increasing concentrations of MgO in the films and up to (94)% when the concentration ratio (90)%. The increase in transmittance due to increase the Mg-contents attributed to increase in temperature, which leads to increased crystallization and thereby increase the transmittance. It is noted that the best transmittance of the mixed thin films was at x=(90)% $Mg_{0.9}ZnO_{0.1}$ thin films.

It is observed from the fig.4.10b, that the optical transmittance increases slightly with increasing the substrate temperature. These changes in the transmittance are associated to the increase in carrier concentration. The same behavior occurs at substrate temperature of (500) °C, as shown in the fig. 4.10c, and the best temperature is (450) °C in order to obtain a higher absorption coefficient.

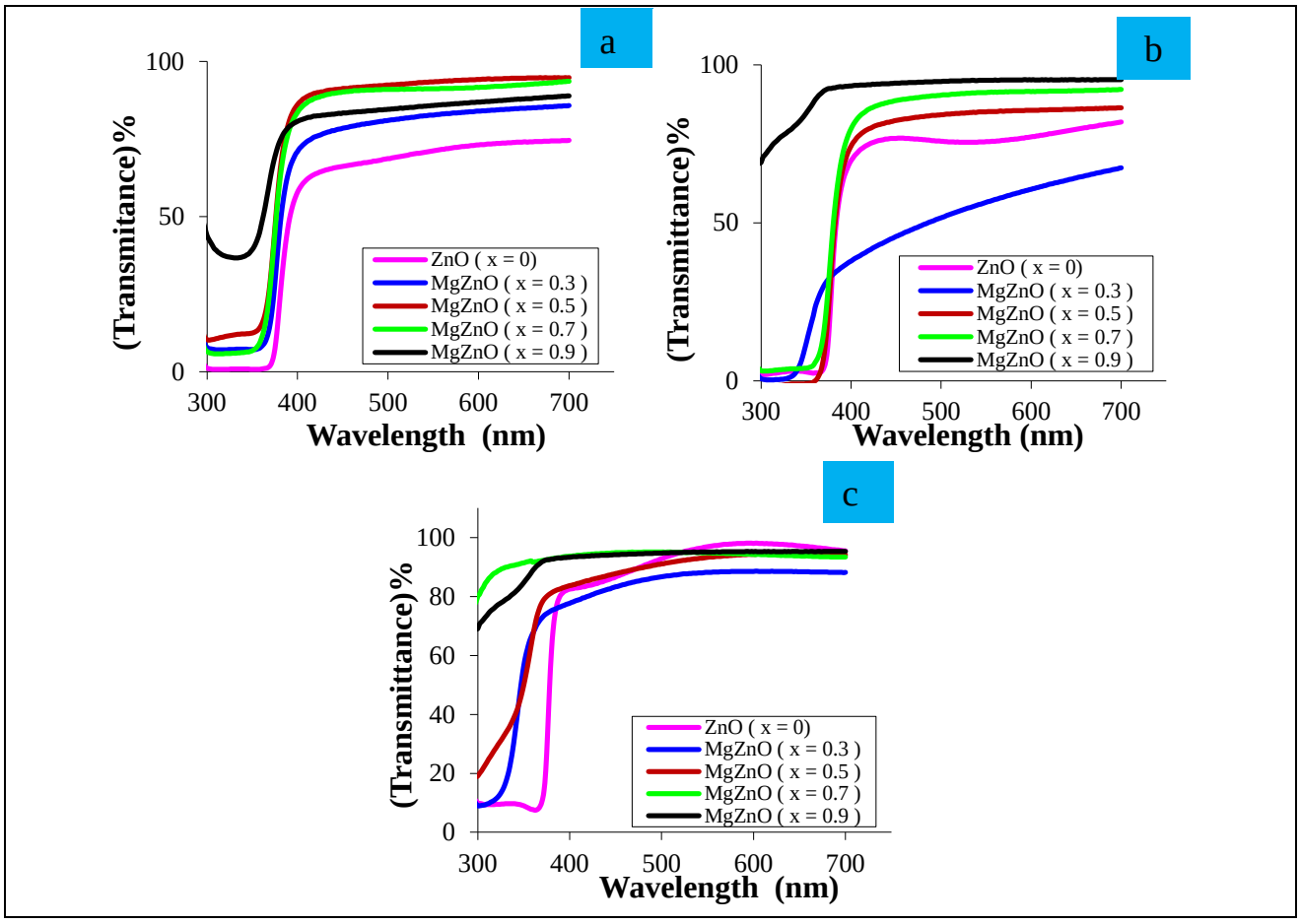


Fig.4.10: Transmittance as a Function of Wavelength for $Mg_xZnO_{1-x}$ Films Prepared in Various Mg-Contents (x), at Substrate Temperatures,( a=400 ,b=450, and c=500) $^oC$.

### 4.4.2 Messurements of Absorbance Spectrum for $Mg_xZnO_{1-x}$ Thin Films

Optical transmission and absorption spectra depend on the chemical composition, crystal structure, energy of the incident photon, film thickness, and film surface morphology. The absorption spectra of the mixed $Mg_xZnO_{1-x}$ thin films in the spectral range of (300-700) nm are compared as a function of Mg-content (x) as shown in fig.4.11a.

The average absorbance for the wavelength in visible region (430-700) nm varies between (0.186-0.128)%, for x=0, pure ZnO. For x=(30)% $Mg_{0.3}ZnO_{0.7}$ thin films the absorbance varies between (0.112-0.068)%, these results are similar behavior into [45].

For x=(50)% the absorbance which more decreases. This increase was caused by the increasing crystallity of ZnO as has been confirmed in structural studies. While

for x=(90)% the absorbance which also decreases, this may probably be due to increasing Mg- content. From the fig.4.11 note that the increasing of Mg-content (x) leads to decreasing in absorbance in the visible region. Considered as temperature of the important contributing factors to the arrangement of atoms within the crystal structure, when the temperature of (450)°C, it is increased absorbance as shown in fig.4.11b is an indication of reduced crystalline defects and increase the regularity of the lattice due to the effect of temperature.

The average absorbance for the wavelength of visible region(0.119-0.088)% for x=0, pure ZnO. For x=(30)% $Mg_{0.3}ZnO_{0.7}$ thin films the absorbance varies between (0.351-0.161)%. Concentration ratio has been characterized (30)% as it was with high absorbency compared to other ratios. This interesting feature may be related to the solubility of Mg-atoms in the ZnO structure and may point to an increase in the localized impurity levels in the energy gap of ZnO as the concentration of Mg is raised.

Note that the remaining ratios increased compared to the temperature (400) °C with the exception of focus ratio (90)% and this may be due to the preparation technique or due to crystal defects within the energy gap. At a temperature of (500) $^{o}$C, absorbance fall further due to increased transmittance, and the reason is the low absorption coefficient and by the relationship (2-10), as shown in fig. 4.11c.

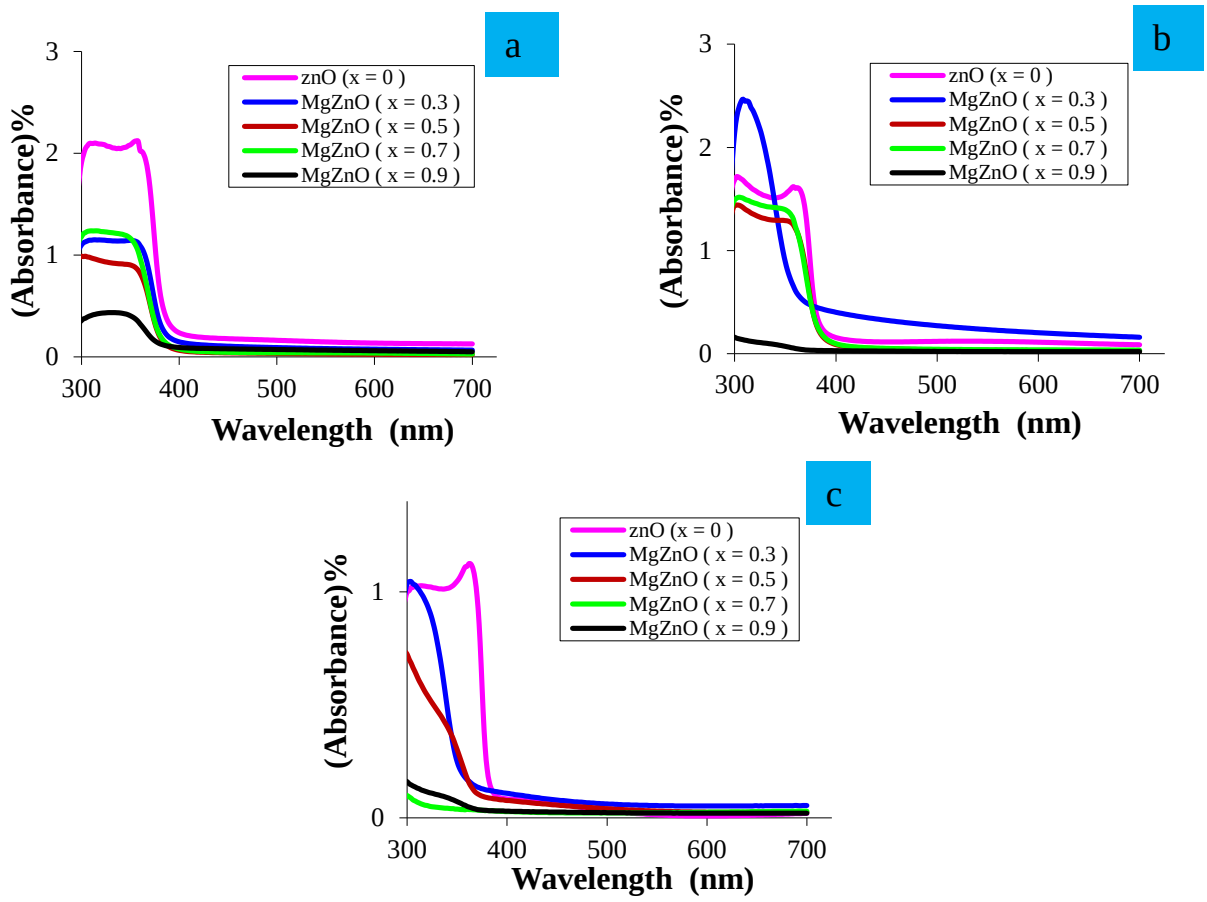


Fig.4.11: Absorbance as a Function of Wavelength for $Mg_xZnO_{1-x}$ Thin Films Prepared in Various Mg-Contents (x),at Substrate Temperatures (a=400,b=450,and c=500) $^oC$.

### 4.4.3 Messurements of Reflectance Spectrum for $Mg_xZnO_{1-x}$ Thin Films

Figs.(4.12a,b,and c) show the reflectance (R) for pure ZnO and mixed $Mg_xZnO_{1-x}$ thin films at different Mg-content, at substrate temperatures (400,450 ,and 500) $^oC$, and constant thickness. It is found that higher reflectivity of ZnO films when absorption edge (380)nm and then decreases with increasing of wavelength, at (450)nm the reflectance tends to saturation at high wavelengths. At substrate temperature of (400) $^oC$, it is found that the reflectivity of pure ZnO films decreased with increasing wavelength, but when add the Mg-content in the ratios mentioned above note initially increase the reflectivity and when increasing the wavelength, it reduces.

But in general, increasing the reflectivity of the $Mg_xZnO_{1-x}$ thin films compared with pure ZnO films, and tend to saturation at high wavelengths as shown in

fig.4.12a. Vary the reflectivity increases and decreases when the substrate temperature (450)ºC depending on the preparation of films and the deposition technique, as shown in fig.4.12b. At (500) ºC note the greatly increased of reflectivity pure ZnO films as shown in fig.4.12c, and this increase is due to reduce defects and increase crystallizing and therefore less surface roughness, either in the $Mg_xZnO_{1-x}$ note decreased the reflectivity with increase Mg-content and this is due to increased acceptor positional levels within the energy gap which leads to the widening gap.

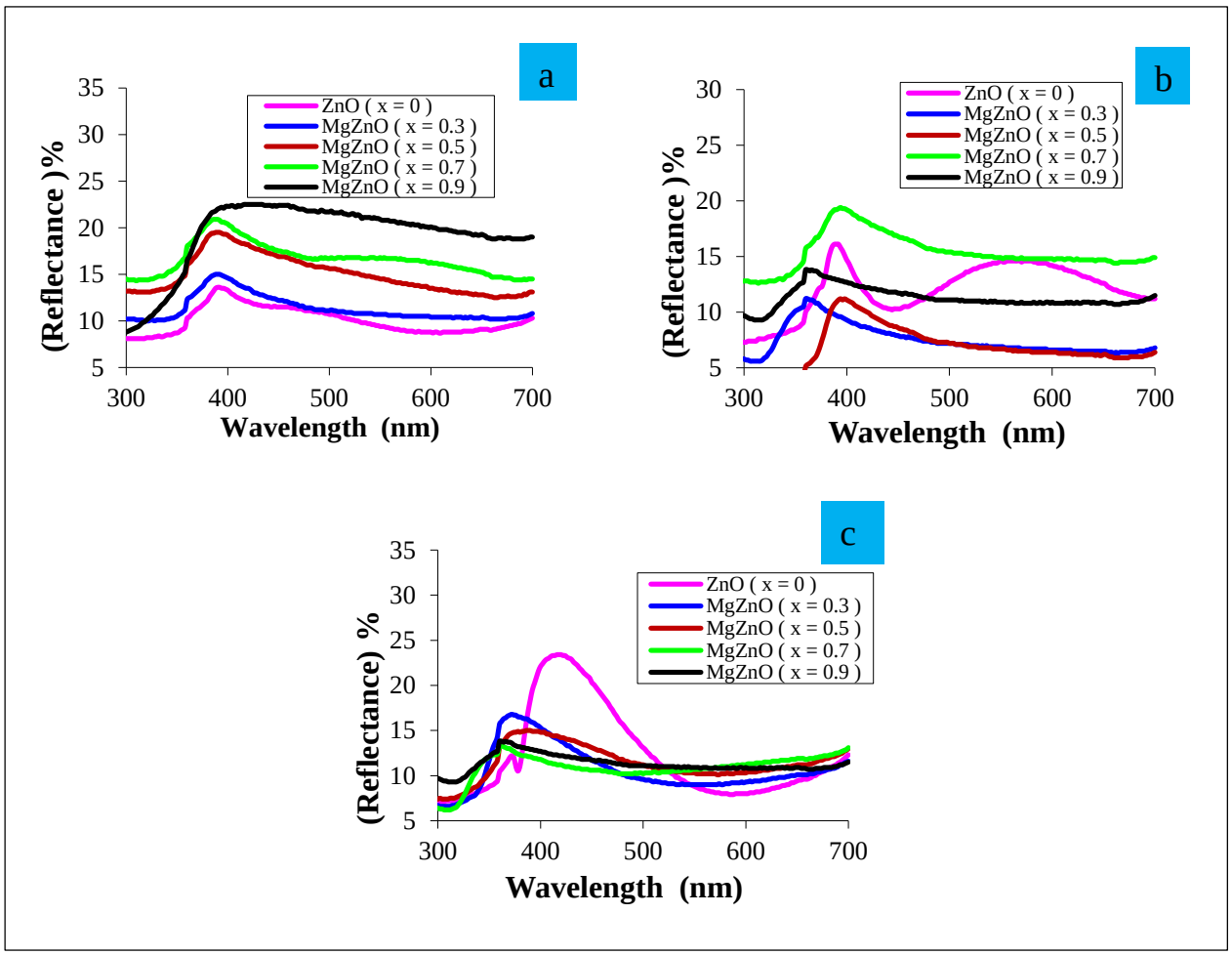


Fig.4.12: Reflectance as a Function of Wavelength for $Mg_xZnO_{1-x}$ Thin Films Prepared in Various M-Contents (x), at Substrate Temperatures(400,450,and 500) ºC.

### 4.4.4 Measurements of Absorption Coefficients for $Mg_xZnO_{1-x}$ Thin Films

Figs.(4.13a,b,and c) shows the absorption coefficient (α) of the $Mg_xZnO_{1-x}$ thin films with different Mg-contents, at substrate temperatures (400,450,and 500) ºC determined from absorbance measurements using equation (2-10). The (α) for the

$Mg_xZnO_{1-x}$ thin films was calculated from equation (2-10). The values of (α) for pure ZnO and $Mg_xZnO_{1-x}$ thin films are found to be lesser than ($10^4$ )$cm^{-1}$ in the UV-Vis region.

The (α) decreased sharply in the visible region, because it is inversely proportional to the transmittance. This means that the electronic transitions between the valence band and the conduction band directly. The (α) of $Mg_xZnO_{1-x}$ thin films is shown in fig.4.13a, as a function of wavelength, at substrate temperature (400) $^oC$ the values of (α) for all thin films are found for wavelength at absorption edge. It is noted that the absorption coefficient at absorption edge for pure ZnO film is equal to ($61\times10^4$) $cm^{-1}$,which decrease randomly with increasing of Mg-content. This can be attributed to the expansion of edge absorption can be the result of the effect of disorder of grain boundaries and the absence of stoichiometry which it generally observed in crystalline materials, or may be due to the absorption of another mechanism because the film has a multi-phase structures as mentioned in the discussion XRD.

But when the substrate temperature (450)$^oC$, generally low absorption coefficient and is attributed to the same reasons mentioned, but when the Mg-content ratio (30)% it is seen that there is a large increase in the absorption coefficient it can be taken advantage of in important applications and attributed this to increase absorption edge is believed to be this porous sample with high and thus led to increased absorption coefficient, or may be a high concentration ratio as shown in fig.4.13b. At substrate temperature of (500) $^oC$,it is noted low of absorption coefficient clearly and this because of the increased transmittance as shown in fig. 4.13c.

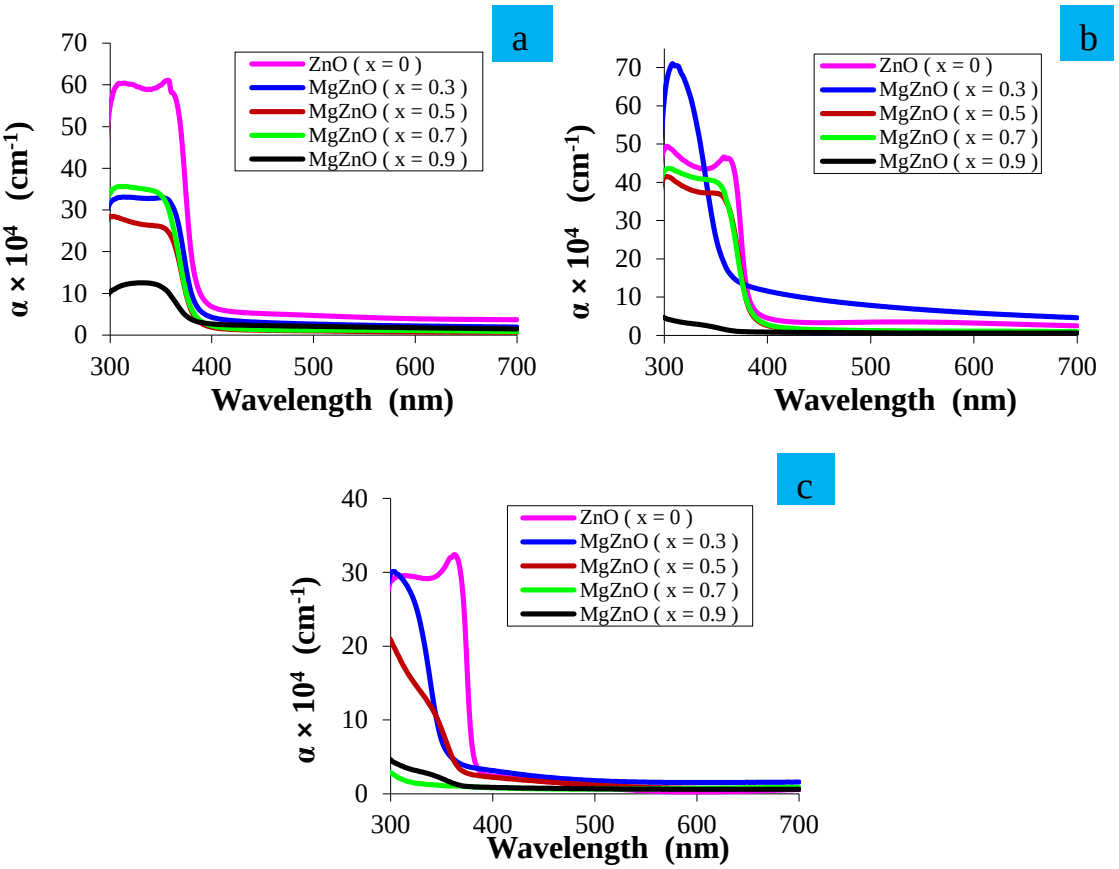


Fig.4.13: Absorption Coefficient as a Function of Wavelength for $Mg_xZnO_{1-x}$ Films Prepared in Various Mg-Contents (x), at Substrate Temperatures (a=400, b=450, and c=500) $^oC$.

### 4.4.5 Measurements of the Optical Energy Gap for $Mg_xZnO_{1-x}$ Thin Films

The optical energy gap can be estimated by calculating the absorption coefficient (α) by applying the Touch equation (2-11) [118] . In order to calculate the energy gap of thin films, the plot of $(\alpha h\nu)^2$ as a function of the energy of incident radiation has been shown in figs. (4.14- 4.16), at substrate temperature (400) $^oC$ the optical energy gap is obtained from intersect of the extrapolated linear region of the curve with the energy axis.

The calculated energy gap value of the pure ZnO is (3.18-3.21) eV, and at (30)% Mg-content is found to be around (3.23-3.30) eV at substrate temperatures of (400,and

450)°C, while at different Mg-contents (50,70, and 90)%, the energy gap value of the $Mg_xZnO_{1-x}$ thin films increased to (3.33,3.35, and 3.37) eV respectively,at(400) $^oC$,

with increasing the Mg-contents, this is due to an increase positional levels within the energy gap when increasing the Mg-content these results are similar behavior into [14].

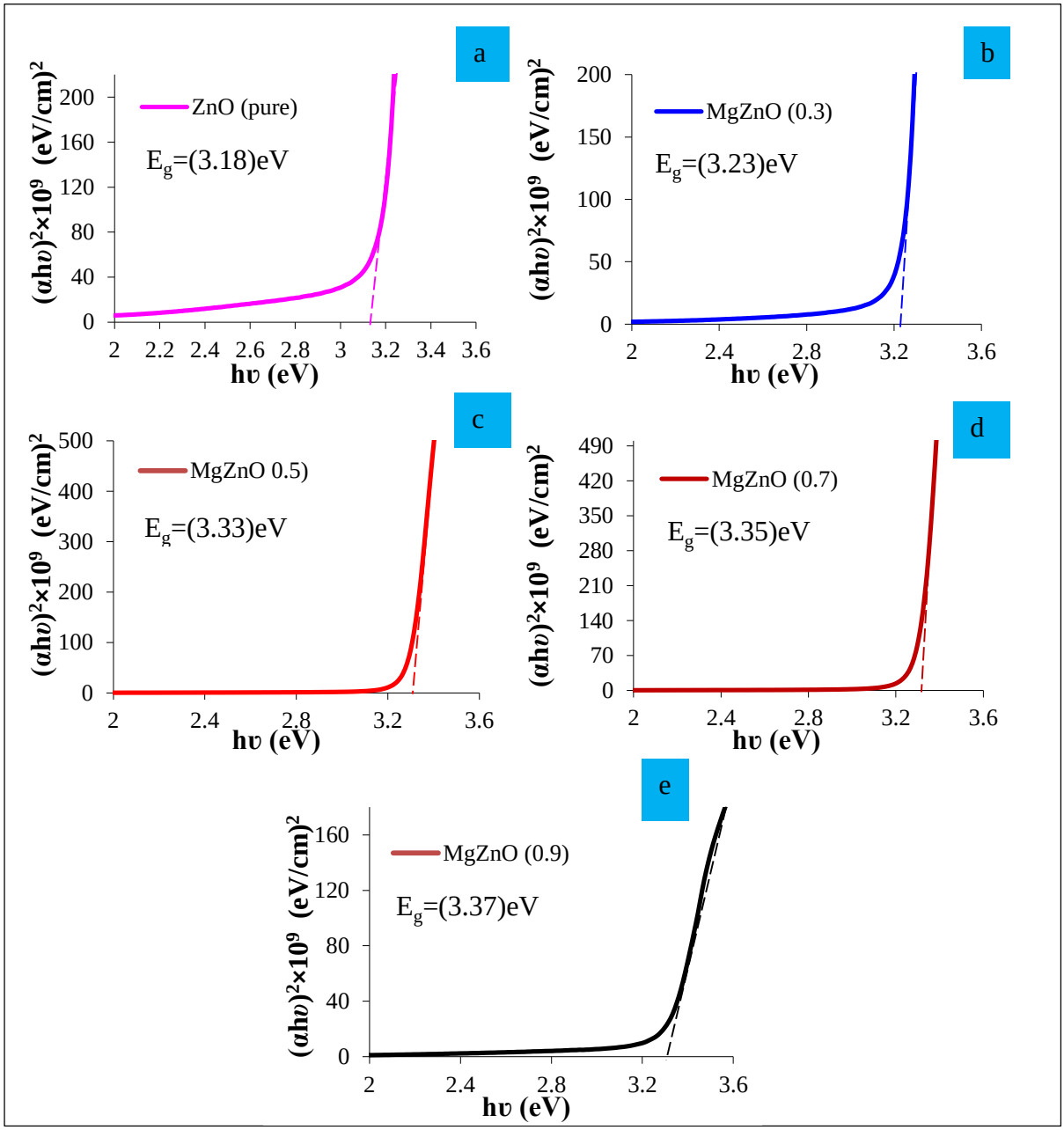


Fig.4.14:$(\alpha h\upsilon)^2$ Versus Photon Energy for $Mg_xZnO_{1-x}$ Thin Films in Various Mg-Contents (x), at Substrate Temperature (400) ºC.

At the same contents (50,70, and 90)%, and at substrate temperature (450)°C led to lower energy gap when increasing Mg-content except percentage (90)% as shown in fig.4.15 e, it is believed that the reason for this increase is due to the samples preparation or the preparation technique.

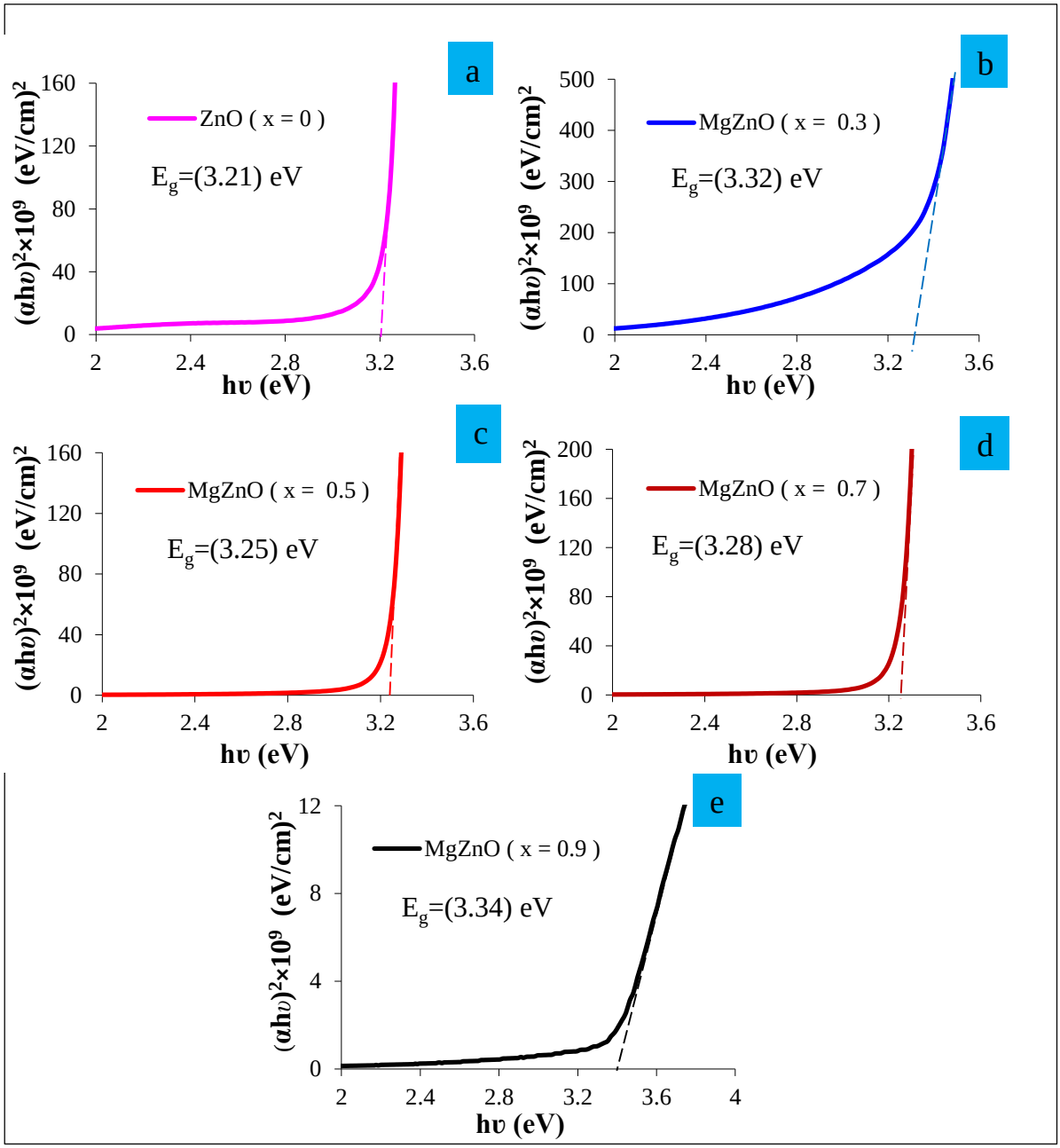


Fig.4.15: $(\alpha h\upsilon)^2$ Versus Photon Energy for $Mg_xZnO_{1-x}$ Thin Films with Mg-Contents (0,30,50,70, and 90)%, at Substrate Temperature (450) $^oC$.

When the substrate temperature (500)$^oC$, it is noticed that the energy gap of pure ZnO decreases to(3.19) eV due to the lack of crystalline defects led to reduce positional levels within the energy gap as shown in fig.4.16a , while at increasing the Mg-content we note increase energy gap for $Mg_xZnO_{1-x}$ thin films, as shown in figs.(4.16b,c,d, and e).

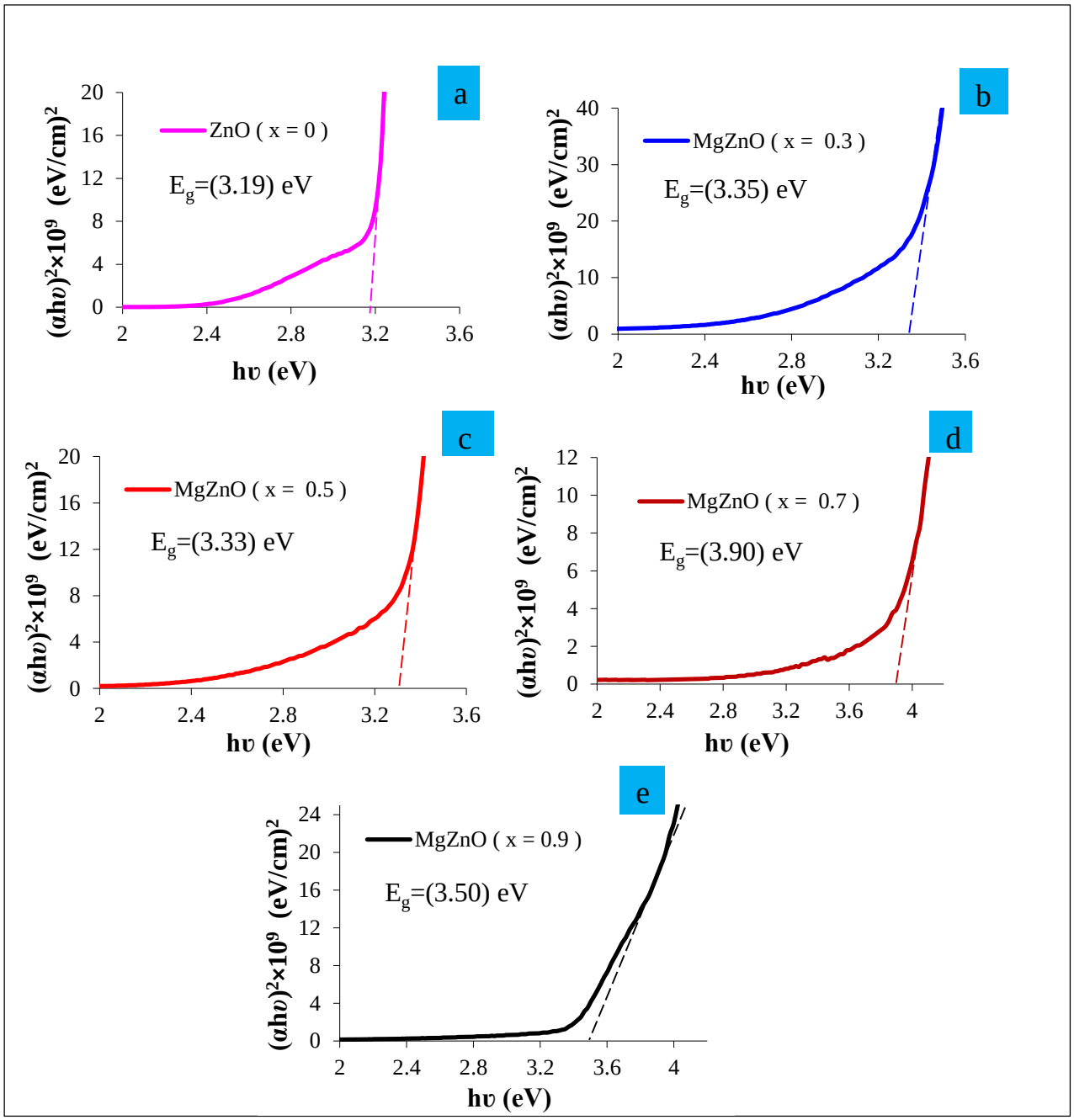


Fig.4.16:$(\alpha h\upsilon)^2$ Versus Photon Energy for $Mg_xZnO_{1-x}$ Thin Films with Mg-Contents (0,30,50,70, and 90)% at Substrate Temperature (500) $^oC$.

### 4.4.6 Messurements of Refractive Index for $Mg_xZnO_{1-x}$ Thin Films

The refractive index (n) is the ratio between the speed of light in vacuum to its speed in material which doesn't absorb this light. The (n) was calculated from the relation (2-15). The values of (n) versus wavelength (λ) shown in figs.(4.17 a, b, and c).

From these figures the maximum value of (n) for all thin films is approximately equal to a value (3.15). Figures below shows the changes of (n) for the pure ZnO and $Mg_xZnO_{1-x}$ thin films at different substrate temperatures. For all samples the (n) increases with the increasing of wavelength in the visible region in all substrate temperatures (400,450,and 500) $^oC$. The (n) decreases when increasing the Mg-content in the films when the substrate temperature (400) $^oC$, as shown in the fig. 4.17a. But the (n) increases when increasing Mg-content in the films when the substrate temperatures (450,and 500) $^oC$, as shown in the figs.(4.17b, and c). This is due to the reflectivity where it decreases with increasing substrate temperatures from (450 to 500) $^oC$.

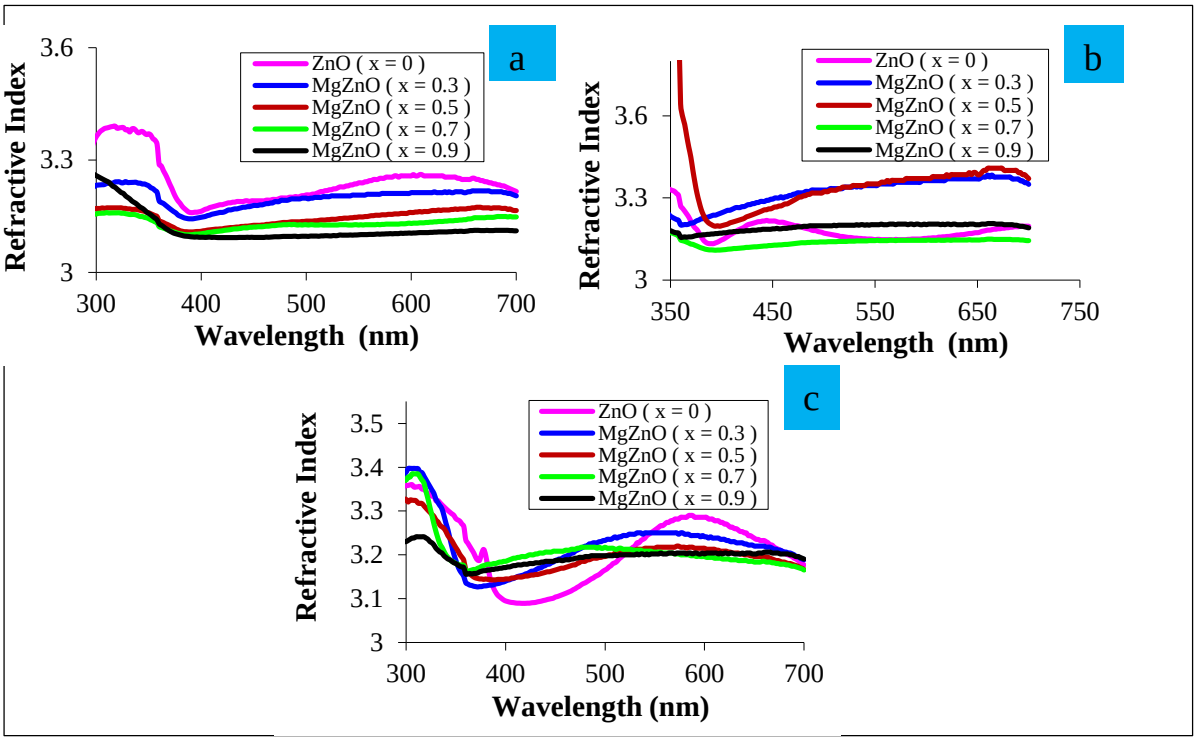


Fig.4.17: Refractive Index as a Function of Wavelength for $Mg_xZnO_{1-x}$ Films in Various Mg-Contents (x), at Substrate Temperatures (a=400, b=450, and c=500) $^oC$.

### 4.4.7 Messurements of Extinction Coefficient for $Mg_xZnO_{1-x}$ Thin Films

The extinction coefficient ($k_o$) is calculated using the relation (2-١7). Fig.4.18, shows the ($k_o$) as a function of wavelength ($\lambda$) for different temperatures of pure ZnO and $Mg_xZnO_{1-x}$ thin films. It's clear from the figure that the ($k_o$) has the same behavior ($\alpha$), but increase of temperature leads to decreases the defects or the tails

within the energy gap so decrease the ($k_o$) values in the pure ZnO. Also shows the effect of concentration of MgO on the ($k_o$) values. When the temperature increased to (450) $^oC$ leads to increased ($k_o$) values with increasing Mg-content. In general, it is noted that the maximum value of ($k_o$) when the absorption edge and then decrease sharply when the visible region of wavelengths, and when increasing the Mg-content shifted absorption edge toward shorter wavelengths(i.e.,high-energy). The ($k_o$) when the substrate temperature (500) $^oC$ is reduced to increase the Mg-content, and this is very clear due to lower ($\alpha$).

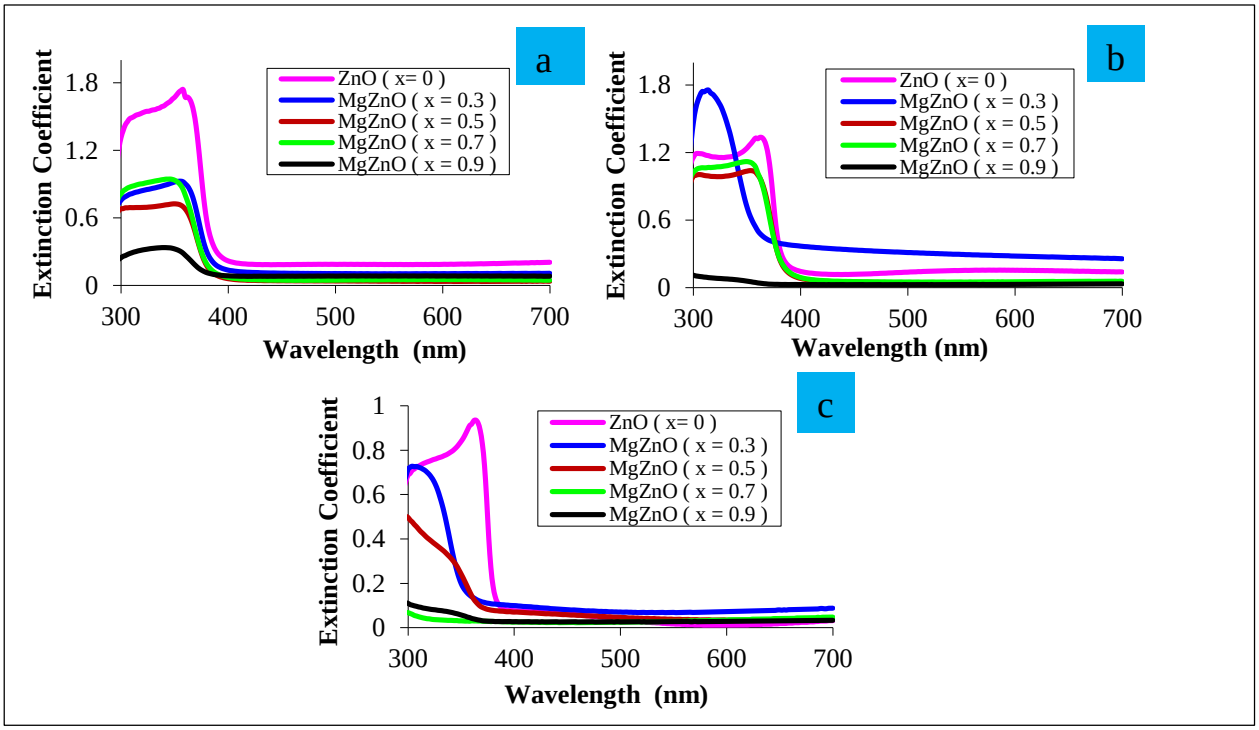


Fig.4.18: The Extinction Coefficient as a Function of Wavelength for $Mg_xZnO_{1-x}$ Thin Films in Various Mg-Contents (x),at $T_s$ (a=400, b=450,and c=500) $^oC$.

### 4.4.8 Messurements of Real and Imaginary Dielectric Constant for $Mg_xZnO_{1-x}$ Thin Films

Real and imaginary parts of dielectric constants were determined using the equations (2-19, and 2-20) respectively. The plots of real ( $\varepsilon_r$) and imaginary ($\varepsilon_i$) dielectric constants of thin films with different $Mg_xZnO_{1-x}$ thin films values are illustrated in figs.(4.19 a1,b1,c1, and 4.20 a2 ,b2 ,c2). The figures shows that the behavior of ($\varepsilon_r$) with wavelength ($\lambda$) was similar to the (n) behavior. And increase its value to the maximum value when the visible region are in the range of (9.89-10.31)

to pure ZnO, when the temperature (400) $^{o}$C and increases its value at high temperatures, as shown in figs.(4.19 a1,b1,and c1). When mixing Mg-content with ZnO and when the substrate temperature (400) $^{o}$C ($\varepsilon_r$) decreases.

The wavelength of the maximum value shifted toward shorter wavelength (high energy) with increasing Mg-content. But all these values located in the visible spectrum in the region which does not absorb the photon. When the substrate temperature increased to (450) $^{o}$C increases the ($\varepsilon_r$) value and this is attributable to the increase in the (n). But when the substrate temperature (500) $^{o}$C it is noticed that the ($\varepsilon_r$) decreases and therefore behave as (n).

Figs.(4.19 a2, b2, and c2) shows the behavior of ($\varepsilon_i$) vs.($\lambda$) for all Mg-content values. The behavior of ($\varepsilon_i$) is like behavior ($k_o$) and the maximum values of ($\varepsilon_i$) change with Mg-content and also substrate temperatures (400,450, and 500) $^{o}$C, while ($\lambda$) values of its maximum are nearly constant with change Mg-content. From the above, it is noted that the increase in the proportion of Mg-content to re-arrange the localized state causing an increase in material conductivity on the account of decreases in real dielectric constant.

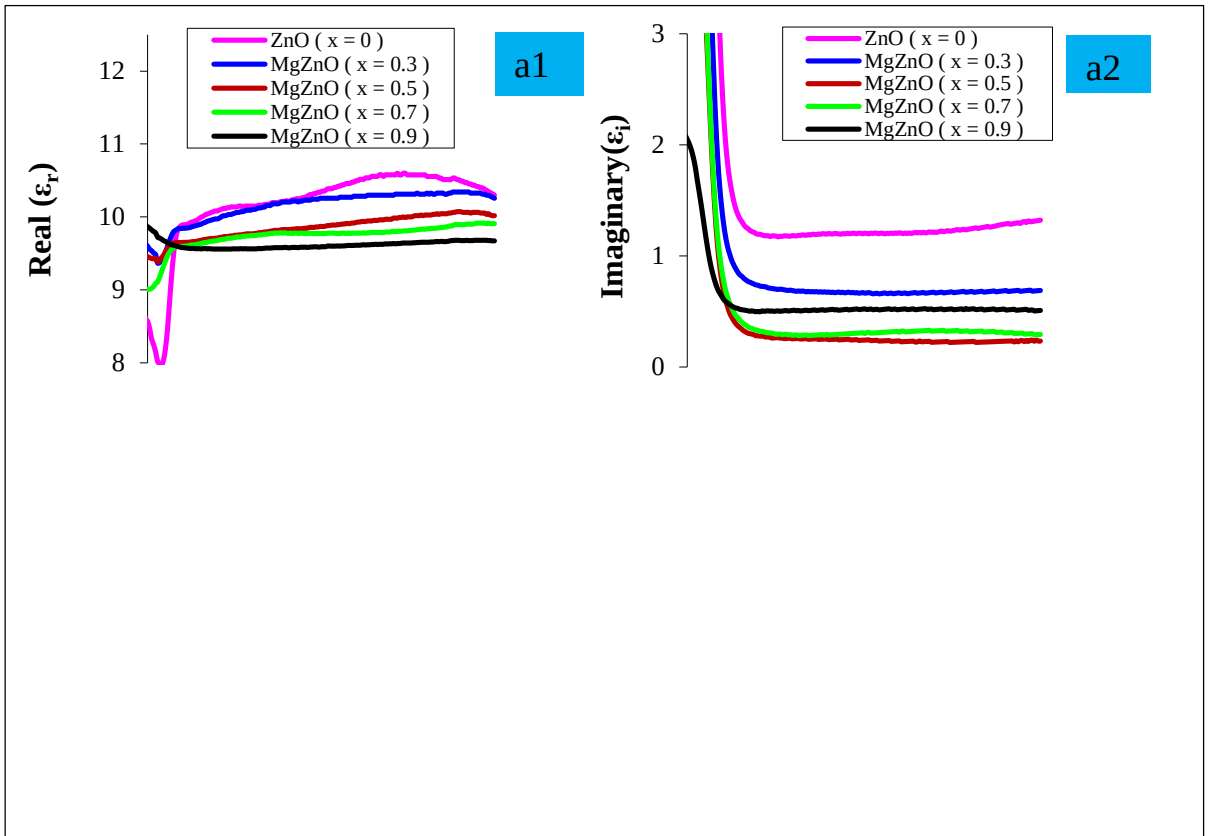

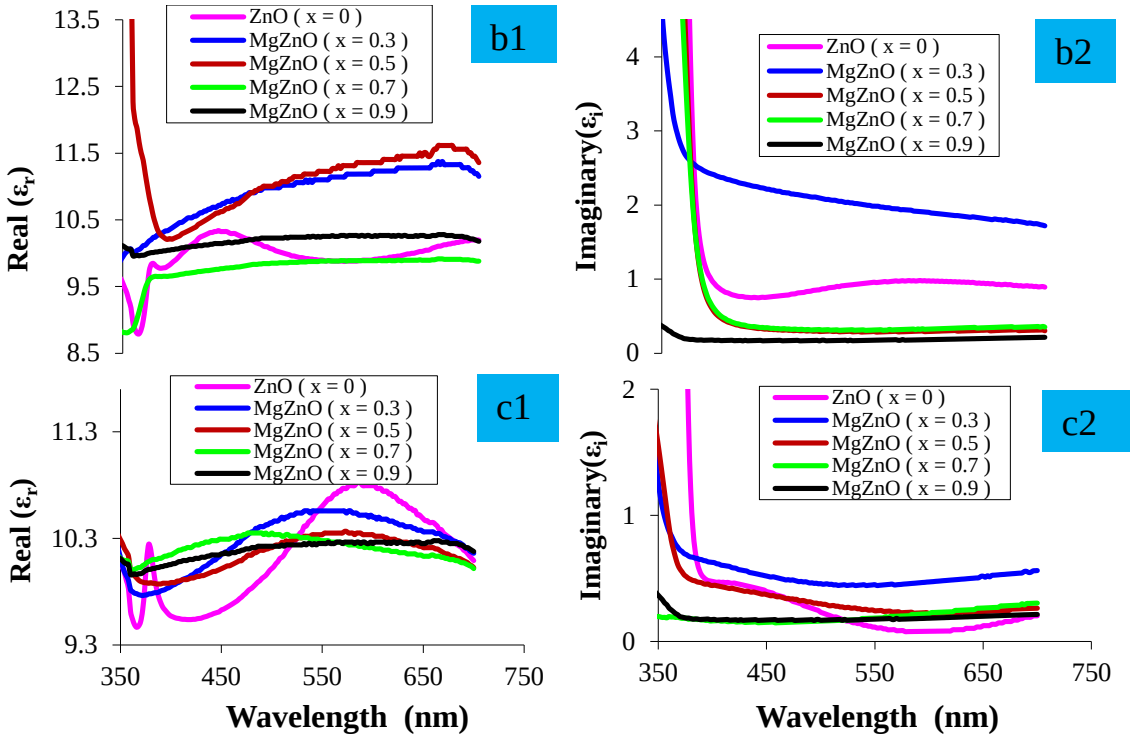


Fig.4.19: Variation of $\varepsilon_r$ and $\varepsilon_i$ as a Function of Wavelength for $Mg_xZnO_{1-x}$ Thin Films with Mg-Contents (0,30,50,70,and 90)%, at Substrate Temperatures (a1, a2=400, b1, b2=450, and c1,c2= 500) $^oC$.

## 4.5 Photoluminescence for $Mg_xZnO_{1-x}$ of Investigation Temperatures

Photoluminescence (PL) spectra obtained from pure ZnO and $Mg_xZnO_{1-x}$ thin films deposited on glass substrate by (CSP) technique with different Mg-content, at substrate temperatures (400,450,and 500) $^oC$, and at a fixed nitrogen pressure of (4.5) bar is

shown in fig.4.20.

It can be seen that the intensity of UV emission peaks increases with the increase of the substrate temperature in the range of (400 -500) $^oC$. The strongest UV emission around (349.5) nm ,as shown in fig.4.20 with a narrow full width at half maximum (FWHM) is observed from the film deposited at (400) $^oC$.

When the substrate temperature increased to (450) $^oC$, the intensity of the UV emission peak decreases slightly. The fig. 4.20 shows the intensities of the deep level emissions (DLEs). The (DLE) centers in second intensity of the ZnO films deposited at substrate temperatures (400,450, and 500) $^oC$ are (448,448.2,and 446.7)nm

corresponding to (2.767,2.766,and 2.775) eV respectively. It is interesting to note that the ZnO film deposited at substrate temperature of (400) $^{o}$C observes only strong ultraviolet emission. The third intensity the (DLE) centers of the ZnO films are (537,536,and 535) nm corresponding to (2.309, 2.313, and 2.317) eV respectively.

However, the two ultraviolet emission in the present search is obtained from a nanocrystalline (polycrystalline) ZnO film deposited by a simple (CSP) method. It implied that the (DLE) has no relation with the crystalline defects like grain boundaries or dislocations. It is understood that the (DLE) is probably relative to the variation of the intrinsic defects in ZnO films, such as Zinc vacancy $V_{Zn}$, oxygen vacancy $V_o$, interstitial Zinc $Zn_i$, interstitial oxygen $O_i$, and antisite oxygen $O_{Zn}$. Different intrinsic defects correspond to various excited energies in (DLE) [120].When mixed MgO with ZnO concentrations (0,0.3,0.5,0.7,and0.9) corresponding to substrate temperatures (400,450, and 500)$^{o}$C respectively as shown in figs. (4.21 a, b, and c).

At substrate temperature of (400)$^{o}$C was the intensity corresponding to the Mg-contents above are (349.5,348.5,350,350.9,and 349.9) nm corresponding to the (3.547, 3.558 ,3.542 ,3.533, and 3.543) respectively. The maximum intensity when the Mg- content ratio (30)%. The (DLE) centers in second intensity of the $Mg_xZnO_{1-x}$ thin films deposited at substrate temperature (400)$^{o}$C is (448,446.7,446,449.1,and 445.9) nm corresponding to (2.767,2.775,2.78,2.761,and 2.78) eV respectively.

The third intensity the (DLE) centers of the $Mg_xZnO_{1-x}$ thin films are (537,537,546,537,and 538) nm corresponding to (2.30,2.309,2.313,2.309, and 2.305) eV respectively, as shown in fig.4.21a. It is observed that the same behavior for substrate temperatures (450 and 500) as shown in the formats (4.21b and 4.21c) .

But was the maximum intensity of the ratio Mg-content (90)% emitted from the surface at substrate temperature of (500) $^{o}$C. These results are similar behavior into [26,121].

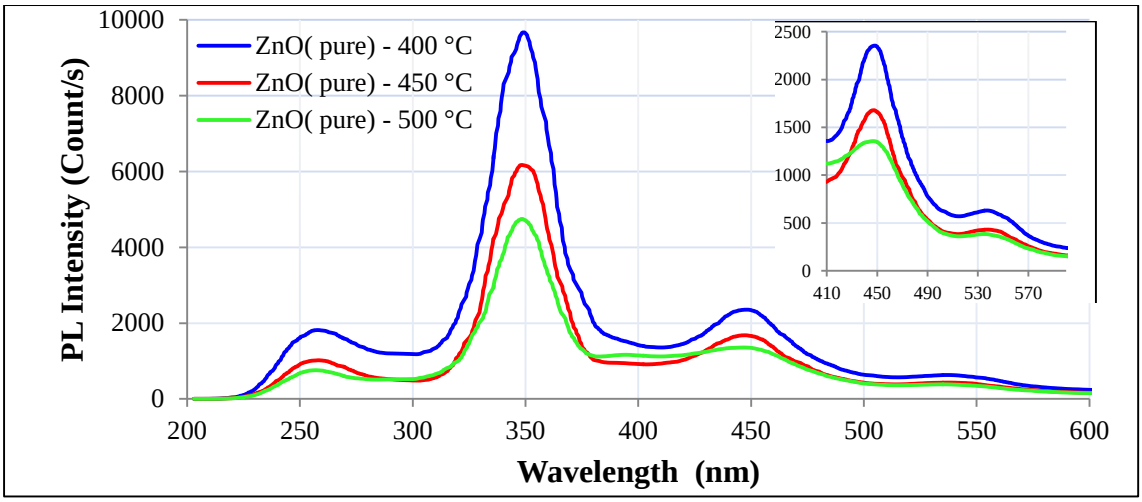


Fig.4.20:PL Spectra of ZnO Thin Films at Substrate Temperatures (400,450, and 500)$^{o}$C.

a

b

Fig.4.21: PL Spectra of $Mg_xZnO_{1-x}$ Thin Films with Mg-Contents (0,30,50,70, and 90)%, at Substrate Temperatures (a=400, b=450, and c=500)$^{o}$C.

## 4.6 Electrical Properties of ZnO, and $Mg_xZnO_{1-x}$ Thin films

The electrical properties of pure ZnO and $Mg_xZnO_{1-x}$ thin films which are deposited on glass substrate at different Mg-contents (0,30,50,70, and 90)% for

different substrate temperatures will be presented. These properties include the D.C electrical conductivity measurements to identify resistant films and activation energy, and also the Hall effect which gives information about the resistivity,conductivity, mobility of carriers, Hall coefficient, density of carriers and type of conductivity.

### 4.6.1 Direct Continuous Electrical Conductivity of ZnO, and $Mg_xZnO_{1-x}$ Thin films

The D.C conductivity of $Mg_xZnO_{1-x}$ thin films as a function of 1000/T, at substrate temperatures (450,and 500)$^oC$ with different Mg-contents (0,30,50,70, and 90)% have been investigated. All of the films prepared at substrate temperature (450) $^oC$, showed that a resistivity varied in the range (13.44-2.38×$10^5$) Ω. cm corresponding to the Mg-content, are similar behavior into [42]. Finally the films prepared at substrate temperature (500) $^oC$ exhibit that a resistivity varied in the range (1.71-1.47×$10^3$) Ω. cm.

This refers to a major change has occurred in the materials with the increase of Mg-content in the films. It is well known that pure ZnO is an n-type semiconductor with a low electrical resistivity. Hence, the electrical restitution in films is probably related to the formation of Mg involving complexes and the generation of native defects acting as acceptors. $\sigma_{D.C}$ increases with increasing substrate temperature, this means that the $Mg_xZnO_{1-x}$ thin films have negatived thermal coefficient of resistivity and this is an essential property of semiconductors.

### 4.6.2 The Activation Energy of ZnO, and $Mg_xZnO_{1-x}$ Thin films

Fig.4.22 shows activation energy of ZnO, and $Mg_xZnO_{1-x}$ thin films are calculated from $ln\sigma_{D.C}$ versus(1000/T)with different Mg-content,at substrate temperature (450) $^oC$.

From this figure it is noted that the films possess of two activation energy depend on Mg-content. This means there are two mechanisms for conductivity. The activation energy depends on the mixing ratio and it will increase with increasing mixing until it reaches a certain value , then began to decrease. Its depends on the donor or accepter carrier concentration and the impurity of energy levels. An increase

in donor carrier concentration brings the Fermi level up in the energy gap and results in the decrease of activation energy these results are similar behavior into [42].

The activation energy is obtained for these films as shown in fig. 4.23, which calculated from the slope of $\ln\sigma_{D.C}$ versus 1000/T. From this figure that films owns two activation energy depend on Mg-content ratios. This means there are two mechanisms for conductivity. whereas that activation energy in the low range temperature depends on the ionization impurity and at high range temperature depends on the generation of electron-hole pairs. Table 4.6 shows that the value of $Ea_1$ is smaller than values of $Ea_2$.

This indicates that the conductivity depends on the temperature where $\sigma_{D.C}$ directly proportional to $T^{3/2}$. The activation energy decrease with increasing Mg-content in the films, then began to decrease with increasing substrate temperature to(500) $^{o}$C as shown in fig. 4.23. The activation energy decrease with increasing Mg-content ratios, with the exception of high percentages we note that it increases as shown in the table 4.6.

Table 4. 6: Activation Energies for $Mg_xZnO_{1-x}$ Thin Films at Different Mg-Content of (x), and Substrate Temperature (450) $^{o}$C.

| Sample | $Ea_1$ ( eV) | Temp. Range ($^{o}$C) | $Ea_2$ ( eV) | Temp. Range ($^{o}$C) |
|---|---|---|---|---|
| ZnO(pure) | 0.01470 | (25-90) | 0.07900 | (90-200) |
| $Mg_{0.3}ZnO_{0.7}$ | 0.00973 | (25-90) | 0.02609 | (90-200) |
| $Mg_{0.5}ZnO_{0.5}$ | 0.02093 | (25-90) | 0.06681 | (90-200) |
| $Mg_{0.7}ZnO_{0.3}$ | 0.07738 | (25-90) | 0.30174 | (90-200) |
| $Mg_{0.9}ZnO_{0.1}$ | 0.14972 | (25-90) | 0.53854 | (90-200) |

Fig.4.2 2: $\ln\sigma_{D.C}$ Versus 1000/T for $Mg_xZnO_{1-x}$ Thin Films with Mg-Contents (0,30,50,70, and 90)%, at Substrate Temperature (450) $^oC$.

Fig.4.23: $\ln\sigma_{D.C}$ Versus 1000/T for $Mg_xZnO_{1-x}$ Thin Films at Different Mg- Contents (0,30,50,70, and 90)% at Substrate Temperature (500) $^oC$.

### 4.6.3 Hall Effect Measurements of ZnO, and $Mg_xZnO_{1-x}$ Thin films

The resistivity of the $Mg_xZnO_{1-x}$ thin films by (CSP) technique decreases linearly with increasing temperature indicating the semiconductor behaviour. The electrical resistivity($\rho$) of the $Mg_xZnO_{1-x}$ thin films (semiconductor material), their electrical conductivity($\sigma_{D.C}$), carrier mobility($\mu_H$), Hall coefficients ($R_H$), carrier concentrations, and the type of the charge carrier have been calculated from Hall measurements. Hall measurements indicate that the $Mg_xZnO_{1-x}$ thin films have two types of conductivity, pure ZnO show n-type conductivity ,and the films which have contents (0,30,50,70, and 90)% show p-type conductivity.

Hall coefficient ($R_H$) have been calculated from Hall measurements, at substrate temperature (400) $^oC$, was their value is negative for pure ZnO. ($R_H$) and carrier concentration are calculated from equation(2-36) and the value of ($R_H$) increases with the increasing of Mg-content in the films, and the values of carrier concentration decrease with the increasing of Mg-content in the films. Hall mobility is calculated from the product of the conductivity and Hall coefficient according to equation (2-37). It can be seen that the Hall mobility increases randomly with the increasing of Mg-content in the films at (400)$^oC$. At high temperatures (450, and 500) $^oC$ can observe the increases and decreases randomly in (n and $\mu_H$) with Mg-content increase. The overall variation in (n and $\mu_H$) can be understood in terms of the position of MgO in the ZnO lattice. The ZnO film generally grows as an n-type semiconductor, due to the presence of native defects in the form of Zinc interstitials,

oxygen vacancies, or both. A decrease in ($\mu_H$) at mixing concentrations may be due to the interstitial occupancy of MgO in the ZnO lattice. The presence of MgO at interstitial sites and grain boundaries in the form of oxide, besides decreasing grain size, may act as scattering centers and result in a decrease in the observed mobility at mixing concentration.

Figs.(4.24a, b, c, and d) show the resistivity, conductivity, mobility and carrier concentration as a function of Mg-content for the $Mg_xZnO_{1-x}$ thin films.

Fig.4.24: The $\rho$, $\sigma_{D.C}$ ,$\mu_H$, and n Versus Mg-Content for $Mg_xZnO_{1-x}$ Thin Films at Different Substrate Temperatures.

## 4.7 Characterization of ZnO/n-Si, and $Mg_xZnO_{1-x}$/n-Si Photodetector

ZnO/n-Si and $Mg_xZnO_{1-x}$/n-Si are prepared by(CSP) technique. The structural, optical and electrical properties of ZnO/n-Si, and $Mg_xZnO_{1-x}$/n-Si have been studied for different Mg-contents(0,30,50,70,and90)%, at substrate temperatures (400,450,and 500)$^oC$.

### 4.7.1 Surface Morphology Properties of ZnO/n-Si, and $Mg_xZnO_{1-x}$/n-Si Photodetector

The effect of mixing ratios were studied and temperature change on the structural, and surface morphology characteristics for the pure ZnO/n-Si, and $Mg_xZnO_{1-x}$/n-Si.

#### 4.7.1.1 Field Emission Scanning Electron Microscopy for $Mg_xZnO_{1-x}$/n-Si Photodetector

The $Mg_xZnO_{1-x}$/n-Si Photodetector were measured nanostructure in the Islamic Republic of Iran/ University of Tehran/ Razi foundation. Surface morphologies of (FESEM) images and their corresponding (EDX) spectra at different Mg-content (0,30,50,70 and 90)%, at substrate temperature (450) °C are shown in figs.(4.25 A,B, and C- 4.26 D, and E) respectively, were all fixed thickness of the films (80) nm.

In addition, the measurement of concentration ratio of (30)%, at substrate temperatures (400, 450, and 500)°C (best ratio of concentration). The morphology of the surface of pure ZnO is a nanostructure cannot determine its kind, as irregular in shape, as shown in fig.4.26A. From the (FESEM) images the grain size values are found to be in the range of (30-63)nm. When you add certain compensatory ratios of Mg-content into ZnO reduced surface roughness gradually as shown in figs.(4.25 B, and C- 4.26 D, and E). Decrease the grain size in the range of (26-54,21-43,26-58,and15-24)nm corresponding to the concentrations of Mg-contents (30,50,70, and 90)%, respectively. These values were compared with the results of XRD, as shown in table 4.7. At different substrate temperatures (400,450,and 500)$^{o}$C, notice that the grain size increase in the range of (21-37,26-54,and 27-33)nm, respectively to concentration (30)% of Mg-content, as shown in table 4.8, and figs.(4.27A,4.25B,and 4.27C) ,these results are similar behavior into [26]. Grains with large sizes of (100) nm and above represent drops of material deposited in the film, which is considered as a latent defect in the film and this seems obvious when the ratio (90)% of Mg-content.

Fig.4.25: FESEM and EDX for $Mg_xZnO_{1-x}$/n-Si Photodetector for Mg-Contents (0,30,and 50)% Prepared, at Substrate Temperature(450) $^{o}$C.

Fig.4.26: FESEM and EDX for $Mg_xZnO_{1-x}$/n-Si Photodetector for Mg-Contents (70, and 90)% Prepared, at Substrate Temperature(450) $^{o}$C.

Table 4.7: Comparison between the Crystillite Size Calculated from (XRD) and (FESEM) Analysis for $Mg_xZnO_{1-x}$/n-Si Photpdetector.

| Substrate Temperature(450) ºC | | |
|---|---|---|
| **Contents** | **Crystallite Size Calculated from (XRD) (nm)** | **Grain Size Calculated from (FESEM) Images (nm)** |
| **ZnO(pure)** | 47.30 | 30-63 |
| **$Mg_{0.3}ZnO_{0.7}$** | 52.00 | 26-54 |
| **$Mg_{0.5}ZnO_{0.5}$** | 31.60 | 21-43 |
| **$Mg_{0.7}ZnO_{0.3}$** | 37.76 | 26-58 |
| **$Mg_{0.1}ZnO_{0.9}$** | 38.20 | 15-24 |

Table 4.8: Comparison between the Grain Size Calculated from (XRD) and (FESEM) Analysis for $Mg_{0.3}ZnO_{0.7}$/n-Si Photpdetector at Different Substrate Temperatures.

| (30)% Mg- Content | | |
|---|---|---|
| **Substrate Temperature (ºC)** | **Crystallite Size Calculated from (XRD) (nm)** | **Grain Size Calculated from (FESEM) Images (nm)** |
| **400** | 42.06 | 21-37 |
| **450** | 52.00 | 26-54 |
| **500** | 48.94 | 27-33 |

Table 4.9: Compound Percentage of the $Mg_xZnO_{1-x}$ /n-Si Photpdetector.

| **MgO-** | **Compound Percentage ( % )** | **Total** |
|---|---|---|

| Contents | Si | N | O | Zn | Mg | |
|---|---|---|---|---|---|---|
| **ZnO (Pure)** | 73.16 | 4.64 | 12.26 | 9.94 | 0 | 100 |
| **$Mg_{0.3}ZnO_{0.7}$** | 72.29 | 6.82 | 10.55 | 6.64 | 3.70 | 100 |
| **$Mg_{0.5}ZnO_{0.5}$** | 74.09 | 3.92 | 11.60 | 3.55 | 6.84 | 100 |
| **$Mg_{0.7}ZnO_{0.3}$** | 73.67 | 4.57 | 11.66 | 1.40 | 8.70 | 100 |
| **$Mg_{0.9}ZnO_{0.1}$** | 73.18 | 4.69 | 12.16 | 0.52 | 9.45 | 100 |

Fig.4.27: FESEM and EDX for $Mg_{0.3}ZnO_{0.7}$/n-Si Photodetector for Mg-Content Prepared, at Substrate Temperatures(400,450,and 500) $^{o}$C.

### 4.7.1.2 Elemental Analysis for $Mg_xZnO_{1-x}$/n-Si Photodetector

The energy-dispersive X-ray analysis spectra (EDX) of the $Mg_xZnO_{1-x}$/n-Si heterojunction deposited on silicon substrate at (450)$^{o}$C by (CSP) technique with different Mg-contents (x = 0, 30, 50, 70, and 90)% are given in figs.(4.25 a, b, and c-4.30 d , and e). Among the above ratios, the ratio (30)% is the best, when measuring the concentration ratio mentioned at different temperatures was the best temperature is (450) $^{o}$C. Which show that all the films contain the elements (Si, N, O, Zn, and Mg) as expected, indicating formation of the $Mg_xZnO_{1-x}$/n-Si photodetector.

Fig. 4.25a shows the (EDX) spectra of the (pure) ZnO film and it reveals that the compound percentage for the (Si, N,O, and Zn) are (73.16, 4.64 ,12.26, and 9.94) respectively. Fig.4.30b depicts the (EDX) spectra of the $Mg_{0.3}ZnO_{0.7}$/n-Si photodetector with compound percentage for the(Si,N,O,Zn, and Mg) are (72.29,6.82,10.55,6.64,and 3.70) respectively these results are similar behavior into [122].The remaining percentages listed in table 4.9, figs.(4.27a ,4.25b, and 4.27c) shows the temperature change for the best ratio (30)%, the best temperature is (450) $^{o}$C.

The (EDX) spectrum for all films are clearly observable (SiKα ,ZnLα, MgKα, OKα and NKα lines). Lines did not show ZnKα, ZnKβ in the (EDS) spectra. The

adhesion between the MgZnO species and the Si substrate was strong , resulting in higher growth speed in the vertical direction, was the reason why the grain size of MgZnO nanoparticles was lower than those on the Si [123]. Which led to increase the intensity of spectral lines by adding Mg-content.

### 4.7.2 Optical Properties for $Mg_xZnO_{1-x}$/n-Si Photodetector

It included the optical properties of the hetrojunction on the photoluminescence measurements**.**

#### 4.7.2.1 Photoluminescence for $Mg_xZnO_{1-x}$/n-Si Photodetector

PL spectrum of the pure ZnO/n-Si, and mixing $Mg_xZnO_{1-x}$/n-Si with different Mg-content , thin films deposited at substrate temperatures of (400,450,and 500) ºC for ratio Mg-content (30)% only, and at nitrogen pressure of (4.5) bar as shown in figs.(4.28,and 4.29).

In all the samples (pure and mixed) there are three luminescence peaks, first peak is the UV emission corresponding to the near band edge emission (NBE), as shown in table 4.9. The increasing Mg-content lead to increase in PL intensity peaks is observed, but decrease when preparation temperature the films increase , and this is attributable to the increase of oxygen vacancies in the films, as well as decreasing the temperature of preparation the films. a broad peak was observed high- energy in UV region (first emission) as shown in fig.4.28.

The PL emission might have close relation with the luminescence photoinduced electrons and holes, which possibly resulted from the no-integrality of nano-sized $Mg_xZnO_{1-x}$/n-Si such as the lattice distortion and surface oxygen vacancies. However in $Mg_xZnO_{1-x}$/n-Si photodetector, the broad band UV emission at (3.538) eV as shown in table 4.10 this luminescence could be due to the excitons in the charge transfer process. Second luminescence peak is in the visible spectrum (Vi) region (i.e. lower energy) the smaller value of PL peak could be assigned to radiated recombination of electrons and holes trapped in the band-tail states.

A broadband peaked at (447.3) nm was observed this energy emitted at (2.772) eV at (400) $^{o}$C, and which are issued by the deep level emission (DLP) for $Mg_{0.3}ZnO_{0.7}$/n-Si films. Third luminescence peak is also a broadband peaked at (542.5) nm was observed this energy emitted at (2.285) eV at (400) $^{o}$C, and which are issued by the deep level emission (DLP) for $Mg_{0.3}ZnO_{0.7}$/n-Si photodetector. The same behavior for temperatures (450,and 500) $^{o}$C. Fig.4.29 shows PL spectra for $Mg_xZnO_{1-x}$/n-Si photodetector with different Mg-content at substrate temperature (450)$^{o}$C.

They have the same behavior there is no need to repeat of speech former, table 4.11 shows three emission peaks, these results are semelar behavior into[26,١٢1].

Fig.4.28: PL Spectra of $Mg_{0.3}ZnO_{0.7}$/n-Si Photodetector with Mg-Content(30)%, at Different Substrate Temperatures.

Fig.4.29: PLSpectra of $Mg_{0.3}ZnO_{0.7}$/n-Si Photodetector with Different Mg-Contents (0,30, 50,70, and 90)%, at Substrate Temperature (450)$^{o}$C.

Table 4.10: Wavelength and Energy values of Photoluminescence Peaks for $Mg_{0.3}ZnO_{0.7}$ /n-Si Phtodetector, at Different Substrate Temperatures and (30)% Mg-Content.

| ***Substrate $T_s$ ($^{o}$C)*** | ***Mg- Content*** | ***First Emission Wavelength (nm)*** | ***First Emission Energy (eV)*** | ***Second Emission Wavelength (nm)*** | ***Second Emission Energy (eV)*** | ***Third Emission Wavelength (nm)*** | ***Third Emission Energy (eV)*** |
|---|---|---|---|---|---|---|---|
| **400** | **$Mg_{0.3}ZnO_{0.7}$** | 350.4 | 3.538 | 447.2 | 2.772 | 542.5 | 2.285 |
| **450** | **$Mg_{0.3}ZnO_{0.7}$** | 350.9 | 3.533 | 446.8 | 2.775 | 541.6 | 2.289 |
| **500** | **$Mg_{0.3}ZnO_{0.7}$** | 351.1 | 3.531 | 447.8 | 2.769 | 540.1 | 2.295 |

Table 4.11: Wavelength and Energy Values of Photoluminescence Peaks for $Mg_xZnO_{1-x}$/n-Si Phtodetector, at Different Mg-Content, and Substrate Temperature (450)$^{o}$C.

| *Mg- Content* | *First Emission Wavelength (nm)* | *First Emission Energy (eV)* | *Second Emission Wavelength (nm)* | *Second Emission Energy (eV)* | *Third Emission Wavelength (nm)* | *Third Emission Energy (eV)* |
|---|---|---|---|---|---|---|
| **ZnO/ n-Si** | 350.0 | 3.54 | 446.2 | 2.779 | 542.6 | 2.285 |
| **$Mg_{0.3}ZnO_{0.7}$** | 351.0 | 3.53 | 446.8 | 2.775 | 539.9 | 2.296 |
| **$Mg_{0.5}ZnO_{0.5}$** | 349.8 | 3.54 | 448.8 | 2.762 | 543.2 | 2.282 |
| **$Mg_{0.7}ZnO_{0.3}$** | 348.2 | 3.56 | 448.0 | 2.767 | 542.6 | 2.285 |
| **$Mg_{0.9}ZnO_{0.1}$** | 348.1 | 3.56 | 445.7 | 2.782 | 540.0 | 2.296 |

### 4.8 Raman Shift for $Mg_xZnO_{1-x}$/n-Si at $T_s$ (400, 450 ,and 500) $^oC$.

At substrate temperatures (400,450, and 500) $^oC$, and with Mg-content ratio (30)%, there is little difference is to increase the intensity of the peaks and shifted slightly to the rightis noticed as shown in fig.(4.30 400$^o$C,and 450$^o$C), this is due to a change of lattice constants with increasing temperature. While at substrate temperature of (500)$^o$C, the phase separation at same Mg-content ratio and increase the intensity of the peak separation is observed as shown in fig. (4.31500$^o$C) this is due to an increase of lattice defects. These results are similar behavior into[1٢4]. Raman scatterings fig.4.31 confirmed that synthesized $Mg_xZnO_{1-x}$/n-Si samples have crystalline nature with hexagonal wurtzite structure, but with obvious structural disorder induced by the

preparation procedure and presence of impurities. The exact peak positions (frequency) and (FWHM) of each band were determined by Raman spectrometer. To achieve the most accurate deconvolution of the obtained Raman spectra each spectrum was divided into three peaks and analyzed separately.

Firstly the low-frequency region (468)$cm^{-1}$ dominated by acoustic overtones, secondly the intermediate frequency region (872) $cm^{-1}$ where optical and acoustic phonon combinations occur, thirdly the high-frequency region (1306) $cm^{-1}$ formed by optical overtones and combinations for the pure ZnO as shown in fig.4.38a. The intense narrow line at (468)$cm^{-1}$ $E_2^{high}$ first-order ZnO Raman mode-associated with the vibration of oxygen atoms, and which dominates the spectra, surely indicates that these are the scatterings from the hexagonal modification of ZnO [1٢5].

Wurtzite type ZnO belongs to the space group $C_{6v}^4$ and optical phonons belong to the following irreducible representations: $\Gamma_{opt}=A_1+E_1+ ٢E_2+2B_1$. The $A_1$ and $E_1$ are polar modes and both Raman and infrared active, $E_2$ are nonpolar and only Raman active, while the $B_1$ modes are silent [1٢5]. Have tilted orientation the two longitudinal (LO) modes are expected to interact and create one single mode of mixed ($A_1$–$E_1$) symmetry known as quasi-LO mode where ($A_1$–$E_1$) symmetry is (872) $cm^{-1}$, where $E_1$(LO) frequency is expected to show blue shift while $A_1$(LO) is almost unaffected by Mg-mixing these results are similar behavior into [1٢6].

However, due to the two different crystal structures of the $Mg_xZnO_{1-x}$/n-Si end members the two oxides do not show complete solid solubility, and an intermediate composition range exists in which the thin films is phase separated into the wurtzite and cubic structures. However, due to the two different crystal structures of the $Mg_xZnO_{1-x}$/n-Si end films the two oxides do not show complete solid solubility, and an intermediate composition range exists in which the Thin Films is phase separated into the wurtzite and cubic structures. For the Raman investigation of the domains with wurtzite and cubic structures, the Raman selection rules need to be considered.

According to the Raman selection rules, the scattering of the LO phonon of ZnO with the wurtzite structure is allowed. In contrast, MgO with the cubic rocksalt structure has no allowed first order scattering due to the inversion symmetry of the crystal. However, defects and impurities can destroy the symmetry which in turn may result in first order Raman scattering, a phenomenon that was previously observed in MgO. As can be seen in fig.4.31b, the LO mode is found to shift in frequency with Mg-content. Specifically, the LO frequency rises until (30)% Mg-content, which is attributed to the incorporation of Mg into the wurtzite structure. This is expected behavior since the LO mode of MgO is (612) $cm^{-1}$. Above (30)% Mg, the LO frequency is observed to saturate at (601) $cm^{-1}$ as can be seen in fig. 4.31c. The saturation is attributed to the wurtzite structure becoming unable to accommodate additional Mg atoms as shown in figs.(4.31d, and e). The presence of the cubic phase was confirmed previously XRD.

Fig.4.30: Raman Shift for $Mg_{0.3}ZnO_{0.7}$/n-Si Photodetector Prepared at Different Substrate Temperatures.

Fig.4.31: Raman Shift for$Mg_xZnO_{1-x}$/n-Si Photodetector Prepared at Mg-Contents (0,30, 50,70, and 90)%, at Substrate Temperature (450) $^oC$.

## 4.9 Electrical and Photoconductive Properties for Al/$Mg_xZnO_{1-x}$/n-Si/Al Photodetector

Electrical characteristics of the photodetector include on the measurements the capacitance-voltage (C-V), current-voltage (I-V), and photocurrent gain (PG) characteristics. For $Mg_xZnO_{1-x}$/n-Si photodetector at different Mg-content, at substrate temperatures (400,450,and 500) $^oC$ they are presented below:

### 4.9.1 C-V Characteristic of Al/$Mg_xZnO_{1-x}$/n-Si/Al Photodetector

The change of capacitance as a function of reverse bias voltage in the range of (0-1)V and at frequency equal to (0.6-1) MHz has been studied, at different Mg-content, as shown in fig.4.32. It is clear that the capacitance decreases with increasing of the reverse bias voltage, and decreasing be non-linear. Such behavior is attributed to the increasing in the depletion region width, which leads to increase of the value of a built-in potential. An enhancement of the capacitance of zero bias voltage ($C_o$) with the increasing of Mg-content as shown in the table 4.12. behavior attributed to the surface states which leads to an increase in the depletion region and decreasing of the capacitance. The width of depletion region can be calculated using equation (2-41).

From table 4.12 that the depletion region width increases with increasing Mg-content is noticed, which is due to the decreasing in the carrier concentration, and therefore leads to decrease of the capacitance. At higher temperatures (400,450,and 500)$^{o}$C, the hetrojunction capacity increases, and decrease built-in potential ,and this is caused by the increasing of carriers concentration are noted, this behavior was for the proportion of Mg-content (30)% only, as shown in fig.4.33 and table 4.13.

The inverse capacitance squared is plotted versus a reverse bias voltage at different Mg-content of (x), as shown in fig. 4.34. The plots revealed straight line relationship which means that the junction was of an abrupt type. The interception of the straight line with the voltage axis at ($1/C^2$= 0), represents the built–in potential.

From table 4.12 that the built-in potential an increases with increasing of Mg-content is noticed. Fig.4.35 shows the inverse capacitance square is plotted as a function of reverse bias voltage for $Mg_{0.3}ZnO_{0.7}$/n-Si photodetector at different substrate temperatures. From through which, to increase the concentration of carriers which in turn leads to lower hetrojunction capacity and increased built-in potential are noted as listed in the table 4.13.

Fig.4.32: The Variation of Capacitance as a Function of Bias Voltage for Al/Mg ZnO/n-Si/Al Photodetector with Different Mg- Contents (x), at Substrate Temperature (450) $^{o}$C.

Table 4.12: The Variation of the $C_o$ ,W, $V_{bi}$ , and $N_D$ for $Mg_xZnO_{1-x}$ /n-Si Photodetector at Different Mg-Content (x).

| Sample | $C_o$ (nF) | W (nm) | $V_{bi}$ (Volt) | $N_D$ ($cm^{-3}$) |
|---|---|---|---|---|
| **ZnO (Pure)** | 663.328 | 12.37 | 0.70 | $4.10\times10^{21}$ |
| **$Mg_{0.3}ZnO_{0.7}$** | 369.700 | 22.18 | 0.60 | $2.71\times10^{18}$ |
| **$Mg_{0.5}ZnO_{0.5}$** | 333.500 | 24.59 | 0.63 | $2.13\times10^{23}$ |
| **$Mg_{0.7}ZnO_{0.3}$** | 178.750 | 45.87 | 0.70 | $5.54\times10^{21}$ |
| **$Mg_{0.9}ZnO_{0.1}$** | 205.873 | 39.83 | 0.84 | $5.34\times10^{23}$ |

Fig.4.33:The Variation of Capacitance as a Function of Bias Voltage for Al/$Mg_{0.3}ZnO_{0.7}$/n-Si/Al Photodetector with Different Substrate Temperatures.

Fig. 4.34: The Variation of ($1/C^2$) as a Function of Reverse Bias Voltage a Mg-Contents (0,30, 50,70, and 90)% for $Mg_xZnO_{1-x}$ /n-Si Photodetector at Substrate Temperature (450)$^{o}$C.

Table 4.13: The Variation of the $C_o$ ,W, $V_{bi}$ , and $N_D$ for $Mg_{0.3}ZnO_{0.7}$ /n-Si Photodetector, at Different Substrate Temperatures.

| Sample | Substrate Temperature ( $^{o}$C) | $C_o$ (nF) | W (nm) | $V_{bi}$ (Volt) | $N_D$ ($cm^{-3}$) |
|---|---|---|---|---|---|
| **$Mg_{0.3}ZnO_{0.7}$** | **400** | 303.6 | 27.01 | 0.50 | $1.24\times10^{19}$ |
| **$Mg_{0.3}ZnO_{0.7}$** | **450** | 369.7 | 22.18 | 0.60 | $2.71\times10^{18}$ |
| **$Mg_{0.3}ZnO_{0.7}$** | **500** | 404.3 | 20.28 | 0.55 | $6.55\times10^{17}$ |

Fig.4.35: The Variation of ($1/C^2$) as a Function of Reverse Bias Voltage for $Mg_{0.3}ZnO_{0.7}$ /n-Si Photodetector, at Different Substrate Temperatures

### 4.9.2 I-V Characteristics for $Mg_xZnO_{1-x}$ /n-Si Photodetector under Dark

Current-voltage (I-V) characteristic is one of the important parameters of a heterojunction measurement is a which explains the behavior of the resultant current with the applied forward and reverse bias voltage. Figs.(4.36 a, and b) shows (I-V) characteristic at forward and reverse bias voltage with different Mg-content of (x), and substrate temperature (450) $^oC$. The forward dark current is generated due to the flow of majority carriers and the applied voltage injects majority carriers, which lead to decrease of the built-in potential, as well as the width of the depletion region.

As the majority and minority carrier concentrations are higher than the intrinsic carrier concentration which generates the recombination current at lower voltage region (0-0.3)V. This is because the excitation of electrons from the valence band

(V.B) to the conduction band (C.B) will recombine them with the holes which are found at the (V.B), and this is observed by the little increase in recombination current at low voltage region [1٢4]. Either, the diffusion current is represented in the high bias voltage region (>0.3)V, where there is a fast exponential increase in the current magnitude with increasing the bias voltage, which dominates the process. The bias current also contains two regions. In the first region of low bias voltage (<0.3)V, the current slightly increases with increasing of the applied bias voltage, and the generation currently dominates, while at the second high bias voltage region (> 0.3)V, the diffusion current dominates [9٠].

From fig. 4.36a, the value of the current decreases with increasing Mg-content of (x) is observed. Which is attributed to involving defects and dislocations that have an effect on the mobility of charge carriers. These defects are within the levels inside the energy gap, these defects are within the depletion region act as active recombination centers, and consequently they decrease current flow across the junction. The best ratio was the mixing (30)% Mg-content, this ratio under the influence of substrate temperatures (450,and 500) $^{o}$C is taken, the forward dark current increases slightly is noted as shown in fig.4.36c.

Fig.4.36: I-V Characteristics in the Dark for $Mg_xZnO_{1-x}$/n-Si Photodetector (a- Reverse ,b- Forward, c- Forward (30)% ,at Substrate Temperatures (450, and 500)$^{o}$C).

A semilogarithim scale of (I-V) characterization for the forward bias is presented in figs.(4.37, and4.38). These figures show that forward current mechanism correspond with the recombination mechanism. The mechanism of transport current is estimated from the value of the ideality factor (η) where the saturation current can be calculated from intercepting the straight line with the current axis at zero voltage

bias. It is clear from the tables (4.14,and 4.15) that the ideality factor and saturation current decreases with increasing Mg-content (x).

Fig.4.37: I-V Characteristics at Forward Bias Voltage on a Semilogarithim Scale for $Mg_{0.3}ZnO_{0.7}$/n-Si Photodetector, at Dfferent Substrate Temperatures.

Fig.4.38: I-V Characteristics at Forward Bias Voltage on a Semilogarithim Scale for $Mg_xZnO_{1-x}$/n-Si Photodetector at Different Mg- Content (x).

Table 4.14: Values of Ideality Factor (η),and Saturation current ($I_s$) for $Mg_xZnO_{1-x}$/n-Si Photodetector at Different Mg-Content (x).

| **Sample** | η | **$I_s$ (nA)** |
|---|---|---|
| **ZnO (pure)** | 1.709 | 47.00 |
| **$Mg_{0.3}ZnO_{0.7}$** | 1.184 | 52.00 |
| **$Mg_{0.5}ZnO_{0.5}$** | 1.450 | 21.00 |

| | | |
|---|---|---|
| $Mg_{0.7}ZnO_{0.3}$ | 1.293 | 14.00 |
| $Mg_{0.9}ZnO_{0.1}$ | 1.164 | 9.93 |

Table 4.15:Values of Ideality Factor (η),and Saturation Current ($I_s$) for $Mg_{0.3}ZnO_{0.7}$/n-Si Photodetector at Different Substrate Temperature.

| Sample | Substrate Temperature (°C) | η | $I_s$ (nA) |
|---|---|---|---|
| $Mg_{0.3}ZnO_{0.7}$ | 450 | 1.184 | 52.0 |
| $Mg_{0.3}ZnO_{0.7}$ | 500 | 1.855 | 70.0 |

### 4.9.3 I-V Characteristics for $Mg_xZnO_{1-x}$ /n-Si Photodetector under Illumination

The optoelectronic characteristics are the best for photodetector hetrojunction since these characteristics determine how the incident light power converts to photocurrent. This photocurrent is observed in reverse bias only. When the detector is illuminated, the electron- hole pairs are generated, performed in the minority carrier which able to diffuse to the edge of the depletion layer before recombination takes place. The internal electric field in the depletion layer can separate of the electrons and holes, this electric field is much higher where the device is in reverse biased.

Figs.(4.39 a, b, c, and d) show that the reversed (I-V) characteristics of the device measured in different light intensity illumination, the photocurrent under a (60-100) mW/cm² tungsten lamp illumination. It can been reversed current value is at a given voltage for photodetector under illumination which is increases with the increasing of light intensity. It is noticed that increasing the light intensity results in the increased the photocurrent. This can be attributed to the number of absorbed photons become greater and a large number of electron-hole's pairs are generated in the junction. In the linear region ,the thermionic emission and the carrier velocity will increase when the sample illuminated with light of change intensity power.

From the figs.(4.39b,c , and d) the current value at a given voltage for $Mg_{0.9}ZnO_{0.1}$/n-Si under illumination is higher than $Mg_{0.3}ZnO_{0.7}$/n-Si is noticed, the

photocurrent increased from ($1.88\times10^{-8}$ to $1.28\times10^{-7}$) A, corresponding to the ratio of Mg-content (30)% to (90)% as shown in figs.(4.39b to 4.39d). This can be attributed to the increased energy gap with increasing Mg-content.

Fig.4.39: The I-V Characteristics at Different Incident Power Intensity for $Mg_xZnO_{1-x}$/n-Si Photodetector at Reverse Bias Voltage

### 4.9.4 Gain for $Mg_xZnO_{1-x}$/n-Si Photodetector

From measuring the current flow within a film in illumination ($I_{ph}$) and dark ($I_d$) conditions at temperature (450)$^oC$, can be done calculated the gain (G) by using equation (2-49) as shown in table 4.16, which can be defined as a ratio between illumination current ($I_{ph}$) to dark current ($I_d$).

From figs.(4.40,and 4.41), the decrease in gain and then reduces depending on increasing the Mg-content and temperature is noted. This behavior is attributed to the low number of carriers concentration in the film. The intensity of the optical power is (1000)mW$(cm)^{-1}$, and high of the optical source (30) cm in the case of measuring photocurrent, and for all samples.

Best ratio of the Mg-content were (30)%, and when the treatment of this ratio under substrate temperatures (450, and 500) $^oC$, the gain increases with high temperature is noticed, as in the table 4.17, has been increasing rapidly at substrate temperature of (500)$^oC$, as in fig.4.42, due to increase photocurrent. These results are similar behavior into [١٢7].

Table 4.16:The Variation of the Photocurrent,Dark Current, and the Gain for $Mg_xZnO_{1-x}$/n-Si Photodetector at Different Mg-Content, and $T_s$ (450)$^oC$.

| Optical Power(1000mW/(cm)$^2$ at High (30) cm | | | | |
|---|---|---|---|---|
| **Mg- Content** | **Substrate Temperature (°C)** | **$I_d$ (μA)** | **$I_{ph}$(μA)** | **Gain** |
| **$Mg_{0.3}ZnO_{0.7}$** | 450 | 0. 0242 | 227 | 9380 |
| **$Mg_{0.3}ZnO_{0.7}$** | 500 | 0.0166 | 177 | 10662 |

Table 4.17: The Variation of the Photocurrent, Dark Current, and the Gain for $Mg_{0.3}ZnO_{0.7}$ /n-Si Photodetector at Different Substrate Temperatures.

| Substrate Temperature (450) °C<br>Optical Power(1000mW/(cm)$^2$ at High (30) cm | | | |
|---|---|---|---|
| **Mg- Content** | $I_d$ (μA) | $I_{ph}$(μA) | Gain |
| **ZnO (Pure)** | 0. 1410 | 316 | 2241 |
| **$Mg_{0.3}ZnO_{0.7}$** | 0. 0242 | 227 | 9380 |
| **$Mg_{0.5}ZnO_{0.5}$** | 0. 0145 | 15.6 | 1076 |
| **$Mg_{0.7}ZnO_{0.3}$** | 0.0 222 | 18.5 | 833 |
| **$Mg_{0.9}ZnO_{0.1}$** | 0. 0946 | 43.4 | 459 |

Fig.4.40: The Photocurrnt and Dark Current as a Function of Forward Bias Voltage for $Mg_xZnO_{1-x}$/n-Si Photodetector at Different Mg-Contents.

Fig.4.41: The Photocurrnt and dark Current as a Function of Forward Bias Voltage for $Mg_{0.3}ZnO_{0.7}$/n-Si Photodetector at Both Substrate Temperatures (450,and 500)$^oC$.

## 4.10 Figures of Merit for $Mg_xZnO_{1-x}$ /n-Si Photoconductive Detectors

### 4.10.1 The Spectral Responsivity

Fig.4.42 shows the spectral responsivity ($R_\lambda$) as a function of wavelneth for all substrate temperatures and all values of Mg-contents. It is found from the figure that ($R_\lambda$) increase with the increasing of Mg-contents for white light and bias voltage equal to 3V for ratio (30)% of Mg-content only. The ($R_\lambda$) by using equation (2-54) is calculated.

Fig.4.42a shows ($R_\lambda$) change as a function of wavelength. It is clear from figure that there are two regions of the peaks response, the first region at visible spectrum(450)nm,and the second located at near infrared spectrum (NIR)(900) nm.

The result of ($R_\lambda$) means that the portion of light with higher energy, such as (450) nm, is absorbed by $Mg_xZnO_{1-x}$ layer (one region) and the portion of light with lower energy, such as (900) nm (two region), can completely incident into n-Si substrate and is absorbed. These results are due to the absorption edges MgZnO and n-Si. At short wavelength incident photon energy which is larger than the energy gap indicates a large increase in the ($R_\lambda$) and this increase relates to the high absorption

coefficient. The ($R_\lambda$) of the ratio of Mg-contents (50,70, and 90)% are more decrease, is due to increment of the barrier height and decrement of the absorption coefficient. When the substrate temperature increase (400, 450, and 500) $^oC$ into the proportion of Mg-content (30)% only, the ($R_\lambda$) increase is noted, this is due to the same reason above as shown in fig.4.42b.

Fig. 4.42: The Variation of Responsivity as a Function of Wavelength for$Mg_xZnO_{1-x}$/n-Si Photodetector (a- at Different Mg-Content ,and b- at Different Substrate Temperatures).

### 4.10.2 The Quantum Efficiency

Quantum efficiency (QE) is a very important criterion in the photovoltaic devices which is known as optoelectronic effect, it represents the ratio between the numbers of generating electrons in the hetrojunction to the number of incident photons on the effective area of the hetrojunction. (QE) is related to the change of the spectral responsivity were calculated using equation (2-56). (QE) was determined as a function of wavelength for photoconductive detectors, as shown in fig.4.43a for different Mg-content. It is observed that the photodetector with(30)% from Mg-content has higher quantum efficiency comparing to the photodetectors for the remaining percentages of the Mg-content due to the lowest barrier height and highest photocurrent. When the substratre temperature increase (400,450, and 500) $^oC$ into the proportion for Mg-content (30)% only, the (QE) increase is noticed. This is due to the same reason as shown in fig.4.43b.

Fig.4.43:The Variation of Quantum Efficiency as a Function of Wavelength for $Mg_xZnO_{1-x}$/ n-Si(a- at Different Mg-Contents ,and b-at Different $T_s$).

### 4.10.3 The Specific Detectivity

Fig.4.44a shows the variation of specific detectivity (D*) as a function of wavelength for photodetectore at different Mg-content (x), at substrate temperatures

(400,450,and 500) were calculated using equation (2-60). the structural and electrical properties of this heterojunction is improved. Increasing Mg-content to reduce structural defects and thus reducing the recombination and reduce the noise generated in the current detector center and as a result increase significantly the (D*). When increasing the substrate temperature of preparation of hetrojunction (400,450,and 500) $^{o}$C with the proportion of Mg-content (30)%, (D*) increase. This is attributable to the improvement in the structural and electrical properties as shown in fig.4.44.

Fig.4.44: The Variation of Specific Detectivity as a Function of Wavelength for $Mg_xZnO_{1-x}$/n-Si (a- at Different Mg-Content, and b- at Different $T_s$ ).

**4.10.4 Noise Equivalent Power**

The noise equivalent power (NEP) values were calculated using equation (2-61) as shown in fig. 4.45a for photoconductive detectors at different Mg-content (x). The minimum (NEP) occurs when ($R_\lambda$) has the maximum value is observed as shown in fig.4.45. From this figure (NEP) decreases with increasing of Mg-content is noticed.

When increasing the temperatures (400,450,and 500)$^{o}$C for preparation of photodetector with the proportion of Mg-content (30)%, the (NEP) goes down is noted. This is attributable to the improvement in the structural and electrical properties as shown in fig. 4.45b.

Fig.4.45: The Variation of (NEP) as a Function of Wavelength for $Mg_xZnO_{1-x}$/n-Si Photodetector (a- at Different Mg-Content, and b- at Substrate Temperatures).

## 4.11 Gas Sensing Measurements (GS)

### 4.11.1 Determination of Operation Temperature of $Mg_xZnO_{1-x}$ /n-Si Sensor

One of the common disadvantages of $Mg_xZnO_{1-x}$/n-Si gas sensors is the high temperature required for the sensor operation. For this reason, the effect of the operation temperature on the thin films sensitivity was studied with the aim of optimizing the operation temperature to the lowest possible value. The operating temperature is defined as the temperature at which the resistance of the sensor reaches a constant value. The changing of resistance is just only influenced by the presence of amount of some gases of interest [1٢8].

Figs.(4.46a , and b) show the variation of sensitivity as a function for operation temperature in the range (25-300) $^oC$ of the $Mg_xZnO_{1-x}$/n-Si sensor for substrate temperatures (400,450,and 500) $^oC$. The sensing test was done by using (3)% $NO_2$: air mixed ratio and bias voltage 6V were applied on the electrodes for all samples. The variation of the temperature reveals resistance of the film decreases as the temperature increases from room temperature to (200) $^oC$ showing a typical negative temperature coefficient of resistance (NTCR) due to thermal excitation of the charge carriers in semiconductor[129].

Operating temperature (200)$^oC$, sensor film displays positive temperature coefficient of resistance (PTCR) as temperature increases further, which may be due to the saturation of the conduction band with electrons raise from shallow donor levels caused by oxygen vacancies. At this point an increase in temperature leads to a decrease in electron mobility and a subsequent increase in resistance. These results that ia an agreement with [1٢7,129].

Operating temperature (200)$^oC$, oxygen adsorption at the surface is mainly in the form of $O^{-2}$, while operating temperature (200)$^oC$, chemisorbed oxygen is present in the form of $O^-$, due to the conversion of $O^-$ into $O^{-2}$ oxygen adsorbs the additional electron from the $Mg_xZnO_{1-x}$/n-Si sensor, which is attributed to increase in the resistance of the sensor film as temperature rises further. After this detailed explanation, there are no sensitivity at high Mg-content ratios, and the optimal ratio of Mg-content was (5)%.

The optimum operating temperature is room temperature for the Mg-content (5)% is noticed. In addition, whenever is sample preparation temperature of low was the sensitivity better. It was observed that the optimum operating temperature is (200) °C as shown in fig. 4.46b.

Fig.4.46: The Variation of Sensitivity with the Different Operating Temperature of the Prepared $Mg_{0.05}ZnO_{0.95}$/n-Si Gas Sensor{a- at Substrate Temperatures (450,and 500) $^oC$, and b- at Substrate Temperatures (400,and 450) $^oC$}.

### 4.11.2 Response and Recovery Time of $Mg_xZnO_{1-x}$/n-Si Sensor

Figs. (4.47a, and b) show the relation between the response and the recovery times with the operating temperature of the pure ZnO/n-Si, and $Mg_xZnO_{1-x}$ /n-Si sensor for $NO_2$:air and bias voltage 6V. The response and recovery times are defined as the time need to reach (90)% of a signal change. From fig. 4.47a it took (25.2s) for the pure ZnO/n-Si time sensor to response and (31.5s) to recover at operating temperature (300) $^oC$, when substrate temperature (450) $^oC$. While from fig.4.47b $Mg_{0.05}ZnO_{0.95}$/n-Si sensor took (6.3s) to response and (44.1s) to recover at (25) $^oC$. As for fig.4.47c $Mg_{0.10}ZnO_{0.90}$/n-Si sensor took (18.9s) to response and (126.25s) to recover at (25) $^oC$.

In the substrate temperature (400) $^oC$, as shown in fig.4.47d takes a response time (15.3s) and recovery time (42.3s), at operating temperature (200) $^oC$. From the table 4.18, The response time to the proportion of Mg-content of (5)% faster than the pure ZnO response time is noted, either recovery time be more, and that the optimum operating temperature is (200) $^oC$ when the preparation substrate temperature (400)$^oC$. At substrate temperature of (500)$^oC$, the highest sensitivity at room temperature, response time (28.8s), and recovery time (99.9s) are noticed, as shown in fig. 4.47e.

Table 4.18: The Response Time and the Recovery Time with Different Operating Temperatures of $Mg_xZnO_{1-x}$/n-Si sensor with Different Mg-Content, at Substrate Temperature (400) $^oC$.

Fig.4.47: The Variation of Response and Recover Time with Different Operating Temperatures for $Mg_xZnO_{1-x}$/n-Si Sensor, at Different Substrate Temperatures.

## 4.12 The conclusions

Through what has been discussed in the text of dissertation, it can be concluded

| Operation Temperature ($^oC$) | ZnO (Pure) /n-Si | | $Mg_{0.05}ZnO_{0.95}$/n-Si | |
|---|---|---|---|---|
| | Response Time(s) | Recover Time(s) | Response Time(s) | Recover Time(s) |
| **25** | 28.4 | 76.2 | 26.1 | 149.4 |
| **100** | 33.6 | 47.3 | 14.4 | 63.0 |
| **200** | 41.8 | 38.2 | 15.3 | 42.3 |
| **300** | 29.3 | 34.1 | 15.3 | 36.9 |

the following points:

1. The addition of Mg to the films increases its strength to withstand high temperatures and little of expansion.
2. There are two regions of the peaks response, the first region is located at visible spectrum, and the second located at (NIR). The responsivity, quantum efficiency and specific detectivity decreases in visible region and increase in (NIR) with increasing of Mg-content.

3. Optimum temperature to prepare $Mg_xZnO_{1-x}$/n-Si phtodetector is (450) $^oC$ for the manufacture of photovoltaic detectors, but the best substrate temperature for the $Mg_{0.05}ZnO_{0.95}$/n-Si is (400) $^oC$ for the manufacture of gas sensors.
4. The results are shown that the sensitivity properties of $Mg_xZnO_{1-x}$/n-Si phtodetector for $NO_2$ gas decrease with increasing Mg-content in the films, as well as with increase the substrate temperature.
5. It is found that the sensitivity of the ZnO thin films changes linearly with the increase of the $NO_2$ gas concentration.
6. Sensors ZnO/n-Si films recorded of good measure sensitive to $NO_2$ gas at a concentration of (30) ppm. The maximum sensitive is (67.82)% in the operating temperature of (300) $^oC$, while the $Mg_{0.05}ZnO_{0.95}$/n-Si films the maximum sensitive is (90.8)% in the operating temperature of (200)°C, and (15)% at an operate temperature (25) $^oC$, with fast response and recovery time.
7. The ZnO/n-Si sensors and $Mg_{0.05}ZnO_{0.95}$/n-Si, at nitrogen pressure of (4.5) bar, at substrate temperatures (450,and 400) $^oC$, respectively are promising devices and good for the optical sensors.

## 4.13 Future Works

Through the obtained results is suggested of the following studies for future works:

1. Study of magnetic properties for $Mg_xZnO_{1-x}$ films,and its applications by using pulsed laser deposition (PLD) technique.
2. Study the physical properties of the $Mg_xZnO_{1-x}$/n-Si photpdetector deposited on substrates ($TiO_2$, Quartz,and $SiO_2$), and it's applications by using chemical spray pyrolysis (CSP) technique.
3. Study the physical properties of the $Mg_xZnO_{1-x}$/PS photpdetector, and it's application.

4. Study the effect of concentrations of the oxidizing gases, reducing, and the operating temperature on the sensitivity properties for $Mg_xZnO_{1-x}$ thin films by chemical spray pyrolysis (CSP) technique.
5. Study of the physical properties for dopant effect of MgO on ZnO nanoparticles and it's applications.

## List of Publications

**A- The Papers of Published**


1. A. O. Mousa, N. A. Nema, and S. H. Trier, "Study of structural and optical properties for MgO films prepared by using chemical spray pyrolysis technique", Materials Science, Vol.14, pp.( 426-434), (2016).
2. A. O. Mousa, and S. H. Trier,"$Mg_xZnO_{1-x}$ photodetector grown by chemical spraying pyrolysis technique", Published research an International Journal of Engineering and Advanced Research Technology (IJEART) ISSN: 2454-9290,Vol.2, Issue-8, pp.(54-59) (2016).

3. A. O. Mousa, and S. H. Trier, "The C-V and I-V properties of $Mg_xZnO_{1-x}$/n-Si heterojunction", Published research an International Journal of Engineering and Advanced ResearchTechnology(IJEART) ISSN: 2454-9290,Vol.2, Issue-8, pp.( 60-65) ,(2016).

**B- The Accepted Papers for Publishing**

1. A. O. Mousa, and S. H. Trier, "Structural and optical properties of $Mg_xZnO_{1-x}$ Thin Films by chemical spray pyrolysis (CSP) technique".
2. A. O. Mousa, and S. H. Trier, "Effect of doping and temperature on ($NO_2$) gas sensing properties for $Mg_xZnO_{1-x}$ heterojunction".

**C- The Conferences**

1- The fifth scientific national conference for nanotechnology, advanced material, and it's applications in University of Technology in November, (2015).

## References


[1] B.G. Streetman and S. K. Banerjee, "Solid state electronic devices",6th edition Prentice Hall, New Delhi, (2009).

[2] H. Zhang, X. Ma, Jin Xu, and D. Yang, "Synthesis of CdS nanotubes by chemical bath deposition", Journal of Crystal Growth,Vol.263, pp.(372-376), (2004).

[3] K. L. Chopra and I. Kaur, "Thin film device application", 1st edition ,Plenum Press, New York and London, (1983).

[4] J. Cibert, P.M. Petroff, G.J. Dolan, S.J. Pearton, A.C. Gossard and J.H. English, "Optically detected carrier confinement to one and zero dimension in GaAs quantum well wires and boxes", Applied Physics Letter Vol.49, pp.(1275-1277), (1986).

[5] Y. Yao, Y. Liang, V. Shrotriya , S. Xiao, L. Yu, and Y. Yang "Plastic near-infrared photodetectors utilizing low band gap polymer", Journal of Advanced Materials, Vol.19, pp.(3979-3983), (2007).

[6] D. S. Ginley, H. Hosono, D. C. Paine, "Handbook of transparent conductors", Springer, New York, ( 2010).

[7] A. J. Freeman, K.R. Poeppelmeier, T.O. Mason, R.P.H. Chang, and T.J. Marks, "Chemical and thin-film strategies for new transparent conducting oxides", MRS Bulletin, Vol. 25, pp.(45-51), (2000).

[8] J. Robertson and B. Falabretti, "Electronic structure of transparent conducting oxides", in Handbook of transparent conductors, Springer Science,Business Media, New York, pp. (27-50) , (2010).

[9] C. Muratore, J.J. Moore, and J. A. Rees, "Electrostatic quadruple plasma mass pectrometer and Langmuir probe measurements of mid-frequency pulsed DC magnetron discharges", Surface and Coatings Technology, Vol.163, pp.(12-18), (2003).

[10] G. Patil, D. Kajale, D. D. Kajale, D.N. Chavan, N. K. Pawar, P. T. Ahire, S. D. Shinde, V. B. Gaikwad , and G. H. Jain, "Synthesis, characterization and gas sensing performance of $SnO_2$ thin films prepared by spray pyrolysis ", Bull. Mater. Sci., Vol.34, pp.(1-9), (2011).

[11] R. M. Balabai, and P. V. Merzlikin, " Electronic properties of doped ZnO films:

AB initio calculations", Journal of Physics, Vol. 55, (2010).

[12] N.H. Tran, A.J. Hartmann, and R. N. Lamp, "Structural order of nanocrystalline ZnO films", Journal of Physical Chemistry B, Vol.103, pp.( 4264 - 4268), (1999).

[13] ZnO - Wikipedia, the free encyclopedia, ttps://en.wikipedia.org/wiki/Zinc_oxide, (2016).

[14] Ü. Özgür,Y. I. Alivov, C. Liu, A. Teke, M. A. Reshchikov, S. Doğan, V. Avrutin, S.-J. Cho, and H. Morkocd, "A comprehensive review of ZnO materials and devices", Applied Physics Reviews, Vol.98, pp.(1-301) , (2005).

[15] D.C. Look, D.C. Reynolds, J.R. Sizelove, R.L. Jones, C.W. Litton, G. Cantwell, and W.C. Harsch, "Electrical properties of bulk ZnO",Solid State Communications, Vol.105, pp.(399-401), (1998).

[16] Y. Li, G. Tompa, S. Liang, C. Gorla, C. Lu and J. Doyle, "Transparent and conductive Ga-doped ZnO films grown by low pressure metal organic chemical vapor deposition" ,Journal of Vacuum Science and Technology A, Vol.15, p.1063, (1997).

[17] D. H. Zhang, T. L. Yang, J. Ma, Q. P. Wang, R. W. Gao, and H. L. Ma, "Preparation of transparent conducting ZnO:Al films on polymer substrates by RF magnetron sputtering", Applied Surface Science, Vol.158, pp.(43-48), (2000).

[18] P. Sharma, K. Sreenivas, and K.V. Rao, "Analysis of ultraviolet photoconductivity in ZnO films prepared by unbalanced magnetron sputtering", Journal of Applied Physics, Vol.93, pp.(3963-3970), (2003).

[19] C. Jin ,"Growth and characterization of ZnO and ZnO based alloys $Mg_xZn_{1-x}O$ and $Mn_xZn_{1-x}O$", Ph.D. Thesis, University of Carolina, (2003).

[20] N. Sutradhar, A. Sinhamahapatra , S. K. Pahari, P. Pal, H. C. Bajaj, I. Mukhopadhyay and A.B. Panda, "Controlled synthesis of different morphologies of MgO and their use as solid base catalysts", Journal of Physics Chemistry C, Vol.115, pp.(12308-12316), (2011).

[21] K. Christova, A. Manov, J. Nyhus, U. Thisted, O. Herstad, S.E. Foss, K.N. Hugen and K. Fossheim, "Bulk $Bi_2Sr_2CaCu_2O_x$ with MgO particles embedded by partial melting process", Comptes Rendus del' Academie Bulgare des Sciencesi, Vol. 53, pp.( 17- 24), (2011).

[22] S. Thakoor, H.G. Leduce, J. A. Stern, A.P. Thakoor and S.K. Khanna, "Insulator interface effects in sputter-deposited NbN/MgO/NbN (superconductor-insulator-superconductor) tunnel", Journal of Vacuum Science and Technology A: Vacuum, Surfaces, and Films, Vol. 5, pp.(1721-1725), (1987).

[23] T. Jinand and Y. He, "Antibacterial activities of MgO nanoparticles against foodborne pathogens", Journal of Nanoparticle Research,Vol.13, pp. (6877-6885), (outside the USA), (2011).

[24] Y. Liu, Z. Lockman, A. Aziz, and J. MacManus-Driscoll, "Principles and methods" Journal Physics Condens. Matter 20, p.165201,(2008).

[25] MgO-Wikipedia, the free encyclopedia, https://en.wikipedia.org/wiki/Magnesium_ oxide, (2016).

[26] M. S. Kim, K. T.Noh, K. G. Yim, S. Kim, G. Nam, D.-Y. Lee, J. S. Kim, J. S. Kim, and J.-Y. Leem, "Composition dependence on structural and optical properties of $Mg_xZn_{1-x}O$ thin films prepared by Sol-Gel method", Bull. Korean Chem. Soc.,Vol.32, pp.(3453- 3458), ( 2011).

[27] A. Ohtomo, M. Kawasaki, T. Koida, K. Masubuchi, H. Koinuma, Y. Sakurai, Y. Toshida, T.Yasuda and Y. Segawa,"$Mg_xZn_{1-x}O$ as a II–VI widegap semiconductor alloy", Applied Physics Letter, Vol. 72, pp.(2466-1468) ,(1998).

[28] W. Yang, S.S. Hullavarad, B. Nagaraj, I. Takeuchi, R.P. Sharma, T. Venkatesan, R. Vispute and H. Shen," Compositionally-tuned epitaxial cubic $Mg_xZn_{1-x}O$ on Si(100) for deep ultraviolet photodetectors", Applied Physics Letter, Vol.82, pp.(3424-3426) , (2003).

[29] A. Tsukazaki, A. Ohtomo, M. Kawasaki, T. Makino, C. H. Chia, Y. Segawa and H. Koinuma, "Emission from the higher-order excitons in ZnO films grown by laser molecular-beam epitaxy", Applied Physics Letter,Vol.84, pp.(3858-3860) , (2004).

[30] R. Prabakaran, R. Kesavamoorthy, and A. Singh," Optical and microstructural investigations of porous silicon", Bull. Mate. Sci. Vol.28,pp.(219-225), (2005).

[31] P. A. Temple and C.E. Hathaway, "Multiphonon Raman spectrum of silicon", Physics Review B7, Vol.7, p.3685, (1973).

[32] A.B. Sproul , M. A. Green, "Improved value for the silicon intrinsic carrier concentration from (275 to 375) K", Journal of Applied Physics,Vol.70, pp.(846-854), (1991).

[33] J.L. Vossen, and W. Kern, "Thin film processes", 2nd edition, Academic Press, INC., New York, (1991).

[34] L. Eckertova, "Physics of thin films ", Plenum Press, New York and London p.15, (1977).

[35] C.M. Lampkin, "Growth characterization", Prog. Cryst. , Vol. 1, no. 405, (1979).

[36] F.K. Shan, G. X. Liu, Z. F. Liu, W. J. Lee, G. H. Lee, I. S. Kim, B. C. Shin and Y.S. Yu, "Optical characterizations of ZnO thin films on Si(100) substrates deposited by pulsed laser deposition", Journal of the Korean Physical Society, Vol. 45, pp. (771-775), (2004).

[37] J.-H. Huang, and C.-P. Liu, "The influence of magnesium and hydrogen introduction in sputtered ZnO thin films", Science direct , Thin Solid Films, Vol. 498, pp.(152-157), (2006).

[38] S.S. Hullavarad, N.V. Hullavarad, D.E. Pugel, S. Dhar, I. Takeuchi, and R. D. Vispute, "Homo - and hetero-epitaxial growth of hexagonal and cubic $Mg_xZn_{1-x}O$ alloy thin films by pulsed laser deposition technique", Journal of Physics D: Applied Physics, Vol. 40,pp.( 4887-4895), (2007).

[39] C.-Y. Tsay, M.-C.Wang and S.-C. Chiang, "Effects of Mg additions on microstructure and optical properties of Sol-Gel derived ZnO thin films", Materials transactions, Vol. 49, pp.(1186 - 1191), (2008).

[40] D.Y. Jiang , C.X. Shan, J.Y. Zhang , Y.M. Lu, B. Yao, D.X. Zhao, Z.Z. Zhang, D.Z. Shen, and C.L. Yang, "$Mg_xZn_{1-x}O$ solar-blind photodetector grown by radio frequency magnetron sputtering", Journal of Physics D: Applied Physics,Vol.42, p.3, (2009).

[41] M. Sahal, B. Marí, M. Mollar, and F. J. Manjón , "$Zn_{1-x}Mg_xO$ thin films deposited by spray pyrolysis", Physics Status Solid C7, pp.(2306-2310), (2010).

[42] S. A.Yousif, A. A. Rasheed, and N. F. Habubi, "Electrical properties of $Zn_{1-x}Mg_xO$ thin films prepared by spray pyrolysis technique", The seventeenth

scientific conference of college of education Al-mustansiriyah university, (2010).

[43] H. Kou, X. Zhang, Y. Du , W. Ye, S. Lin and C. Wang, "Electrochemical synthesis of ZnO nanoflowers and nanosheets on porous Si as photoelectric materials", Journal of Applied Surface Science, Vol. 257, pp.(4643-4649), (2011).

[44] S. A. Yousif, N. F. Habubi, and A. A. Rasheed, "The morphology and I-V characteristics of $Zn_{1-x}$ $Mg_xO$ thin films deposited by spray pyrolysis technique", Journal of Electron Devices, Vol.16, pp.(1347 - 1355) ,(2012).

[45] A. Agrawal, T. A.Dar, and P. Sen,"Structural and optical studies of Mg doped ZnO thin films", Journal of Nano- and Electronic Physics Vol.5, pp.(1-3) , (2013).

[46] H. S. Kim, C. H. Kim, and L. Yue, "A study of the growth of single-phase $Mg_{0.5}Zn_{0.5}O$ films for UV LED" , International Journal of Chemical, Nuclear, Materials and Metallurgical Engineering Vol.8, pp.(640-644), (2014).

[47] A. A-K. Hussain, K. A. Aadim, and H. M. Slman , "Structural and optical properties of ZnO doped Mg thin films deposited by pulse laser deposition (PLD)", Iraqi Journal of Physics, Vol.12, pp. (56-61) , (2014).

[48] G. K. Mani, J. Bosco, and B. Rayappan, "Impact of annealing duration on spray pyrolysis deposited nanostructured zinc oxide thin films", Superlattices and Microstructures, Vol. 67, pp.( 82-87), (2014).

[49] S. Shanmugan, D. Mutharasu, and I. Abdul Razak ,"Sol-Gel derived Mg and Ag doped ZnO thin film on glass substrate: Structural and surface analysis", Journal of Optoelectronics and Biomedical Materials Vol.6, pp.(119-129) , (2014).

[50] N. Akın, Y. Özen, M. Çakmak, and S. Özçelik, "Characterization of sputtered-MgZnO thin films as UV sensors", Euro Nano Forum,(2015).

[51] R. Singh, and A. A. Koser, "Synthesis and characterization of ZnO and Mg doped ZnO (Mg-ZnO) nanoparticles by chemical precipitation method",

International Journal of Scientific Progress and Research (IJSPR), Vol.13, pp.(71-73), (2015).

[52] J. Gao, G.J. Zhao, X.X. Liang and T.L. Song, "First-principles study of structural properties of $Mg_xZn_{1-x}O$ ternary alloys", Journal of Physics Conference Series, Vol.574 , pp.(1-6) ,(2015).

[53] C. Kittel, "Introduction to Solid State Physics", 5th edition, John. Wiley and Sons, USA, (1976).

[54] K. Saremah, R. Sarma and H.L. Das , "Correlative assessment of structural and photoelectrical properties of thermally evaporated CdSe thin films", Journal of Non-Oxide Glasses ,Vol.1, pp.(143-156),(2009).

[55] N.M. Saeed , "Structural and optical properties of ZnS thin films prepared by spray pyrolysis technique", Journal of Al-Nahrain University, Vol.14 , pp.(86-92), (2011).

[56] J. Sengupta, A. Ahmed, and R. Labar, "Structural and optical properties of post annealed Mg doped ZnO thin films deposited by the sol-gel method", Materials Letters, Vol.109 , pp. (265-268), (2013).

[57] A. H. Moharram, S. A. Mansour, M.A. Hussein, and M. Rashad, ″ Direct precipitation and characterization of ZnO nanoparticles″,Journal of Nanomaterials, Vol. 2014, pp. (1-5), (2014).

[58] A. Ivashchenko and I. Kerner, "Physical approaches to improvement of semiconductor Gas sensor based on $SnO_2$ thin films", Moldavian Journal of the Physical Sciences, Vol. 2, pp.(95-102), (2003).

[59] T. Allen, S. Rutherford, S. Murray, S. Reipert, and M. Goldberg, "Scanning probe and scanning electron microscopy", Elsevier Science (USA), (2006).

[60] D. Sarid, "Scanning Force Microscopy", Oxford University Press, 2nd edition, (1994).

[61] F.H. Abdulrazzak Aldahlaki, "Synthesis and applications of carbon nanotubes", Ph.D. Thesis, University of Babylon-college of science ,chemistry department, Babylon, (2015).

[62] P.V. Avramov, B.I. Yakobson, and G.E. Scuseria, "Effect of carbon network defects on the electronic structure of semiconductor single-wall carbon nanotubes", Physics of the Solid State, Vol.46, pp.(1168-1172), (2004).

[63] P.-C. Ma, N.A. Siddiqui, G. Marom, and J.-K. Kim, "Dispersion and functionalization of carbon nanotubes for polymer-based nanocomposites a review", Composites: A, Vol.41, pp.(1345-1367), (2010).

[64] S. Byrne, "Raman spectroscopy and X-ray diffraction studies of ZnO grown by pulsed laser deposition", M.Sc. Thesis, School of Physical Sciences, Dublin City University, (2003).

[65] D. C. Look , J. W. Hemsky, and J. R. Sizelove , "Residual native shallow donor in ZnO", Physics Review Letter, Vol. 82, pp.(2552-2555) , (1999).

[66] J. I. Pankove, "Optical processes in semiconductors", Prentice-Hall, Inc., Englewood cliffs, New Jersey, (1971).

[67] D.A. Newman, "Semiconductors physics and devices",3rd edition, basis principles, McGraw-Hill, University of new Mexico, USA, (1992).

[68] J. Millman, "Microelectronics", Murray-Hill, Book Company Kogakusha, (1979).

[69] R. J. Elliot and A.F. Gibson, "An introduction to solid state physics and its application", 1st edition, Macmillan Inc., (1974).

[70] R. Grenier, "Semiconductors device and electronic energy series", Mc Graw-Hill, Book Co. Inc. (1961).

[71] L. L. Kazmerski, "Polycrystalline and amorphous thin films and device", 6th edition, Lawrence Academic Press, New York, (1980).

[72] R. L. Park, M.G. Lagally,"Solid state physics", Academic Press, Inc., Harcourt Brace Jovanovich,Vol.22, New York, (1985).

[73] J. Tauc, "Amorphous and liquid semiconductors", plenums press, New York and London, (1974).

[74] T. S. Moss, "Optical properties of semiconductors", London butterworths scientific Puplications, New York , Academic Press (1959).

[75] M. Grundmann, H. Wenckstern, R. Pickenhain, Th. Nobis, A. Rahm, and M. Lorenz, "Superlattices and microstructures", Vol. 38, pp.(317–328), (2005).

[76] M. Lorenz, H. Hochmuth, R. Schmidt-Grund, E.M. Kaidashev, and M. Grundmann, "Advances of pulsed laser deposition of ZnO thin films", annalen der physics,Vol.13, pp.(59-60) , (2004).

[77] M. Lorenz, E.M. Kaidashev, A. Rahm, T. Nobis, J. Lenzner, G. Wagner, D. Spemann, H. Hochmuth, and M. Grundmann, "$Mg_xZn_{1-x}$ nanowire arrays on sapphire grown by high-pressure pulsed-laser deposition" , Applied Physics Letter, Vol. 86, p.14, (2005).

[78] B.K. Meyer, H. Alves, D.M. Hofmann, W. Kriegseis, D. Forster, F. Bertram, J. Christen, A. Hoffmann, M. Straßburg , M. Dworzak, U. Haboeck, and A. V. Rodina, "Bound exciton and donor-acceptor pair recombinations in ZnO", Physics Status Solidi B, Vol.241, pp.(231-260), (2004).

[79] N. Ashkenov , G. Wagner, H. Neumann, B.N. Mbenkum, C. Bundesmann, V. Riede, M. Lorenz, E.M. Kaidashev, A. Kasic, M. Schubert, and M. Grundmann, "Infrared dielectric functions and phonon modes of high-quality ZnO films", Journal Applied Physics, Vol. 93, pp.(126-133) ,(2003).

[80] Y. R. Park, and C. K. Joo Kim," Optical and electrical properties of Ti- doped ZnO films observation of semiconductor-metal transition", Solid State Communications, Vol.123, pp.(147-150) , (2002).

[81] A. Islam, M. Choudhury and M. Hossan, "Recent development in condensed matter physics and nuclear science", Rajshahi University, Bangladesh, New York, pp.(1969-1978), (1981).

[82] P. Kireev,"Semiconductors physics translated from russian by M. Samokhvalov", MIR Publishers, Moscow, (1978).

[83] D.C. Look," Methods in materials", John Wiley, New York , p.15 , (2000).

[84] B. R. Nag, "Electron transport in compound semiconductors", Journal Applied Spring-Verlag Berlin Heiderg, New York, (1980).

[85] Y. Yu. Peter,and M. Cardona , "Fundamentals of semiconductors", 3rd edition, Physics and Materials Properties, Springer, p.639, (2005).

[86] S.M. Sze, "Physical of semiconductor device", 2nd edition ,John Wiley and Sons,(1981).

[87] B.L. Sharma and R.K. Purohit, "Semiconductor heterojunctions", 1st edition Pergamon Press, New York, (1974).

[88] D. Song, J. Zhao, A. Wang, P. Widenborg, W. Chin, and A. Aberle, "Efficient ZnO/c-Si heterojunction solar cell prepared by magnetron sputtering", 17 European PV conference, munich, pp.(1- 4) , (2001).

[89] F. Chaabouni, M. Abaab, and B. Rezig, "Characterization of n-ZnO/p-Si films grown by magnetron sputtering", Superlattices and Microstructures, Vol.39, pp.( 171-178 ), (2006).

[90] S.M. Sze and K. K. Ng, " Physics of semiconductor devices", 3rd edition , Central Laboratory, John Wiley and Sons in Canada, (2007).

[91] Y. Yu. Peter, and M. Cardona , "Fundamentals of semiconductors physics and materials properties", 4th edition , Springer, (2010).

[92] A.A.M. Farag,"Structure and transport mechanisms of Si/porous Si n–p junctions prepared by liquid phase epitaxy",Applied Surface Science,Vol.255, pp.(3493-3498), (2009).

[93] V. Quemener," Electrical characterization of bulk and thin film ZnO", Ph.D. Thesis ,University of Oslo, Norway, (2012).

[94] G. H. Mohammed, "Optoelectronic parameters of $Pb_xS_{1-x}$ thin films", M.Sc. Thesis, University of Baghdad, Iraq, (2002).

[95] I. Zh. Alferov,"Semiconductor heterostructures physical processes and applications", Printed in RSSA, (1989).

[96] E. M. Nasir ,"Fabrication of CdSe: Cu photoconductive detector by using vacuum evaporation technique and studying its electro-optical properties", M.Sc. Thesis, University of Baghdad, Iraq, (1999).

[97] I. H. Khdayer ,"Fabrication and studying the photo conducting characteristics of InSb Junction with silicon as a single crystal semiconductor", Ph.D. Thesis, University of Baghdad, Iraq,(2005).

[98] L. Xu, L. Shi and X. Li, "Effect of $TiO_2$ buffer layer on the structural and optical properties of ZnO thin films deposited by electron-beam evaporation and sol-gel method", Applied surface science, Vol.255, pp. (3230-3234), (2008).

[99] E.M.Nasir,"Fabriction of $Pb_xS_{x-1}$ detector", Ph.D. Thesis, University of Baghdad, Iraq, (2005).

[100] M. Caria, L. Barberini, S. Cadeddu, A. Giannattasio, A. Lia, A. Rusani, and A. Sesselego, "Far UV responsivity of commercial silicon photodetectors", Journal of Nuclear Instruments and Methods in Physics Research A, Vol. 466, pp.(115-116), (2001).

[101] D. Song, "Effect of RF power on surface- morphological, structural and electrical properties of aluminium-doped zinc oxide films by magnetron sputtering", Applied Surface Science, Vol., 254, pp.(4171-4178), (2008).

[102] R. Ionenescu, and A. Vancu ,"Time-dependence of the conductance of $SnO_2$:Pt:Sb in atmospheres containing oxygen, carbon monoxide and water vapour I. Non-oscillatory behavior", Applied Surface Science, Vol.74, pp.(207-212), (1994).

[103] T. Seiyama, A. Kato, K. Fukushi, and M. Nagatini. "A new detector for gaseous components using semi conductive thin films", Analytical Chemistry ,Vol.34, pp.(1502-1503), (1962).

[104] S. R. Morison , " Chemical sensors in semiconductor sensors", John Wiley , New York, (1994).

[105] S. H. Wang, T.C. Chou, and C. C. Liu, "Nano-crystalline tungsten oxide $NO_2$ sensor", Sensors and Actuators B, Vol. 94, pp.(343-351), (2003).

[106] M. Schuisky, J. W. Elam, and S. M. Georg, "In situ resistivity measurements during the atomic layer deposition of ZnO and W thin films", Applied Physics Letter, Vol. 81, pp.(180-183), (2002).

[107] D. Diamond, "Principles of chemical and biological sensors" ,volume of chemical analysis. John Wiley and Sons, Inc.,Vol.150, (1998).

[108] Ü.Kersen,"Gas sensing properties of nanocrystallite metal oxide powder produced by thermal deposition and mechanochemical processing", Ph.D. Thesis, Helsinki University of Technology, department of electrical and communication engineering, (2003).

[109] A. J. Mohammad," Studying the effect of molarity on the physical and sensing properties of ZnO thin films prepared by spray pyrolysis technique", Ph.D. Thesis, University of Technology , Baghdad , Iraq , (2007).

[110] J. L. Comstock, "Elements of chemistry", 26th edition, Robinson, Pratt. Co.,1838 original from Harvard University digitized, p.356, (2008).

[111] S.J. Kim, S. H. Lee, and C. J. Lee, "Organic vapour sensing by current response of porous silicon layer", Journal Physics D: Applied Physics,Vol.34, pp.(3505-3509), (2001).

[112] S. Wegrzyn, J. Klamka, L. Znamirowski, R. Winiarczyk, and S. Nowak, "Nano and quantum systems of informatics", Bulletin of the polish academy of science technical sciences, Vol.52, pp.(1-10), (2004).

[113] S. Marco, A. Cornet, J. R. Morante, E. Castano, R. Jane, S. Jimenez, A. Pardo, and A. Ortega, "Smart multi sensor integrating methane and carbon monoxide gas detection with improved selectivity by signal processing", Proceedings, San Diego, p.98, (1998).

[114] D. E. Williams, "Semiconductor oxides as gas-sensitive resistors", Sensors and Actuators B,Vol.57, pp.(1-16) ,(1999).

[115] M. T. Wu, X. Yao, Z. H. Yuan, H. T. Sun, W.C. Wu, Q. H. Chen, and G. Y. Xu, "Effect of noble metal catalyst on titanium exhaust gas oxygen sensor", Sensors and Actuators B, Vol.491 , pp.(13-14), (1994).

[116] S. Kose, F Atay, V. Bilgin And I. Akyuz, "In doped CdO films: electrical, optical, structural and surface properties", International Journal of Hydrogen Energy, Vol. 34 , pp. (5260- 5266), ( 2009).

[117] W. Zhao-yang, H. Li-zhong, Z. Jie, S. Jie and W. Zhi-jun, "Effect of the variation of temperature on the structural and optical properties of ZnO thin films prepared on Si (111) substrates using PLD vacuum", Vol. 78, pp.(53-57), (2005).

[118] W. D. Callister, "Materials science and engineering-an introduction",7th edition, New York, John Wiley and Sons,(2007).

[119] H. Jun-Hang , and L. Chuan-Pu, "The influence of Mg and hydrogen introduction in sputtered zinc oxide thin films", Science direct , Thin Solid Films, Vol. 498, pp.(152-157), (2006).

[120] L. Chaoyang, X. Li, E. Pradeep, and K. Toshiyuki, "ZnO thin film phosphor prepared on different substrates by novel multiple reducing annealing", Society for Information Display, Vol.45, pp.(1305-1308), (2014).

[121] A. Kaushal, D. Pathak, R.K. Bedi, and D. Kaur, "Structural, electrical and optical properties of transparent $Zn_{1-x}Mg_xO$ nanocomposite thin films",Thin Solid Films, Vol. 518, pp.(1394-1398), (2009).

[122]P.S. Shewale, and Y.S. Yu, "Structural surface morphological and UV photodetection properties of pulsed laser deposited Mg-doped ZnO nanorods effect of growth time", Journal of Alloys and Compounds,Vol.654, pp.(79-86), (2016).

[123] T. B. Ivetic, M. R. Dimitrievska, N. L. Fincur, L. R. Đacanin, I. O. Gúth, B.F. Abramovic, and S. R. Lukic- Petrovic, "Effect of annealing temperature on structural and optical properties of Mg-doped ZnO nanoparticles and their photocatalytic efficiency in alprazolam degradation", Ceramics International, Vol. 40, pp.(1545-1552), (2014).

[124] J. Huso, H. Che, D. Thapa, A. Canul, M. D. Mc. Cluskey, and L. Bergman, "Phonon dynamics and Urbach energy studies of MgZnO alloys", Journal of Applied Physics, Vol.117, p.125702, (2015).

[125] R. Cusco, E. A. Lladó, J. Ibáñez, and L. Artús,"Temperature dependence of Raman scattering in ZnO", Physical Review B75, pp.(1-11), (2007).

[126] N. Kılınc, L. Arda, S. Öztürk, and Z.Z. Öztürk, "Structure and electrical properties of Mg-doped ZnO nanoparticles", Cryst. Res. Tech.,Vol.45,pp.(529-538), (2010).

[127] J. Yu, C.X. Shan, J. S. Liu, X. W. Zhang, B. H. Li, and D. Z. Shen, "MgZnO avalanche photodetectors realized in Schottky structures", Physics Status Solidi RRL7, pp.(425-428), (2013).

[128] N. H. Al-Hardan, M. J. Abdullah, A. A. Aziz, "Sensing mechanism of hydrogen gas sensor based on RF - sputtered ZnO thin films", International Journal of Hydrogen Energy ,Vol.35, pp.(4428 - 4434), (2010).

[129] J. X. Wang, X. W Sun, Y. Yang, H. Huang1, Y. C. Lee, O. K. Tan and L. Vayssieres, "Hydrothermally grown oriented ZnO nanorod arrays for gas sensing applications", Nanotechnology, Vol. 17, pp.(4995-4998), (2006) .

**الخلاصة**

في هذا العمل تم تحضير أغشية $Mg_xZnO_{1-x}$ باستخدام تقنية الرش الكيميائي الحراري وهي طريقة ملائمة ومناسبة للترسيب على مساحات كبيرة . وتم إنماء مزيج محاليل $Mg_xZnO_{1-x}$ بنسب حجمية مختلفة (٠، ٣٠، ٥٠، ٧٠ و٩٠)% ومرسبه على قواعد زجاجية وسليكونية وعند درجات حرارة مختلفة (400، 450 و 500) درجة مئوية وتم تثبيت السمك من خلال تثبيت عدد الرشات وكان سمك جميع الاغشية يتراوح بين (٥±٨٠) نانومتر وقد تم اجراء الرش باستخدام غاز النيتروجين . تم تشخيص التركيب البلوري للأغشية بتقنية حيود الأشعة السينية (XRD) و اظهرت النتائج ان جميع الأغشية المحضرة كانت متعددة التبلور وأظهرت تحسن في البنية البلورية من خلال تغير درجات الحرارة.

درست طبوغرافية السطح للأغشية باعتماد مجهر القوى الذرية (AFM) والمجهر الالكتروني الباعث الماسح (FESEM) ومشتت الطاقة للأشعة السينية (EDX). إن زيادة نسبة محتوى المغنيسيوم في الاغشية ادت إلى نقصان خشونة السطح . وان (EDX) اظهرت احتواء الأغشية على عناصر(Si ، N، O ، Zn و Mg ) كما هو متوقع . تم قياس استطارة رامان لأغشية $Mg_xZnO_{1-x}$/n-Si الرقيقة لمختلف نسب محتوى

المغنيسيوم ، حيث اظهرت شدة ذات حزمتين $cm^{-1}$(٦٠١ و ١٢٠٢) المقابلة الى انماط استطارة رامان ذات الرتبة الاولى العليا $E_2^{high}$, ونمط الرتبة الثانية هو $A_1(LO)$ وهو نمط الرتبة الأولى بالنسبة لأوكسيد الزنك، اذ انه بزيادة محتوى المغنيسيوم الى اكثر من (50)% فان نمط الرتبة $E_2^{high}$ سوف تنخفض شدته.

وتمت دراسة الخصائص البصرية للأغشية المحضرة من خلال قياس النفاذية البصرية في المنطقة الطيفية (300-700) نانومتر، وكانت نتائج النفاذية تتراوح من (65-89)% عند زيادة محتوى المغنيسيوم من (30-٩٠)% في درجة حرارة (400) درجة مئوية ، وتزداد النفاذية اكثر عند زيادة درجة الحرارة الى (500) درجة مئوية لتصبح من (84-95)% عند محتوى المغنيسيوم نفسه مما يجعلها ملائمة لتطبيقات المتحسسات الغازية. وتم قياس الامتصاصية والانعكاسية لجميع الاغشية وكانت تتناقص بارتفاع درجات الحرارة، بالإضافة الى ذلك تم قياس معامل الامتصاص لجميع الاغشية وكانت قيمته أعلى من $cm^{-1}$ (١٠٤) .

وحسبت فجوة الطاقة المباشرة لأوكسيد الزنك النقي وكانت (3.18، 3.21 و 3.19) الكترون فولت التي تقابل درجات الحرارة (400، 450 و 500) درجة مئوية على التوالي . وتم حساب الثوابت البصرية كمعامل الانكسار ومعامل الخمود وثابت العزل الحقيقي والخيالي لجميع الأغشية المحضرة. وتم حساب فجوة الطاقة البصرية من خلال مطياف الاستضائية وكانت القيم تتراوح بين (3.531 - 3.558) الكترون فولت، تم دراسة الخصائص الكهربائية كالتوصيلية الكهربائية المستمرة وتأثير هول، واظهرت نتائج قياسات تأثير هول ان غشاء اوكسيد الزنك النقي من النوع السالب (n-type) اما اغشية $Mg_xZnO_{1-x}$ فهي من النوع الموجب (p-type) وتمتلك طاقتي تنشيط ($Ea_1$ و $Ea_2$). تم قياس سعة كاشف $Mg_xZnO_{1-x}$ /n-Si كدالة لفولتية الانحياز العكسي وبتردد يتراوح بين (0.6 -1) ميكا هيرتز، واشارت تلك النتائج الى أن كاشف المفرق الهجين من النوع الحاد.

كما وجد إن جهد البناء الداخلي تنخفض قيمته بزيادة محتوى المغنيسيوم وتزداد عند نسبة محتوى المغنيسيوم (٩٠)% . واظهرت خصائص تيار- فولتية لكاشف $Mg_xZnO_{1-x}$ /n-Si ان تيار الظلام الأمامي يتغير أسيا مع فولتية الانحياز، كذلك لوحظ تناقص عامل المثالية وتيار الإشباع العكسي بزيادة محتوى المغنيسيوم في الاغشية في حين يزداد عند درجات الحرارة العالية كما تم في هذا العمل دراسة الخصائص الطيفية للكاشف ووجد أن قيم الاستجابة الطيفية ، الكفاءة الكمية والكشفية النوعية تزداد بزيادة نسبة محتوى المغنيسيوم ، بينما القدرة المكافئة للضوضاء تنخفض بزيادة محتوى المغنيسيوم .

وظهرت قمم الاستجابية عند الطول الموجي (٤٥٠) نانومتر وكانت تساوي الى A/W (13.51) وعند الطول الموجي (900) نانومتر وكانت تساوي الى A/W(36.83) . كما تم حساب الربحية للكاشف ووجد ان الكسب يزداد عند ارتفاع درجات الحرارة . وتم قياس تحسسية المتحسس لغاز $NO_2$ في الهواء المحيط في منظومة استشعار الغاز . وتم فحص جميع العينات في نسبة ٣% $NO_2$: الهواء وفولتية انحياز (٦) فولت. وكانت أفضل نسبة اشابة لمحتوى المغنيسيوم %(x=٥) ، و درجة حرارة القاعدة السليكونية هي (٤٠٠) درجة

مئوية و درجة حرارة تشغيل (٢٠٠) درجة مئوية. وكانت اقصى تحسسية عند هذه النسبة هي (٩٠,٨٠)% وسرعة زمن الاستجابة هو (١٥,٣) ثانية وزمن الاسترجاع هو (٤٢,٣) ثانية.